Univerzita Karlova v Praze
Matematicko-fyzikální fakulta

DIPLOMOVÁ PRÁCE

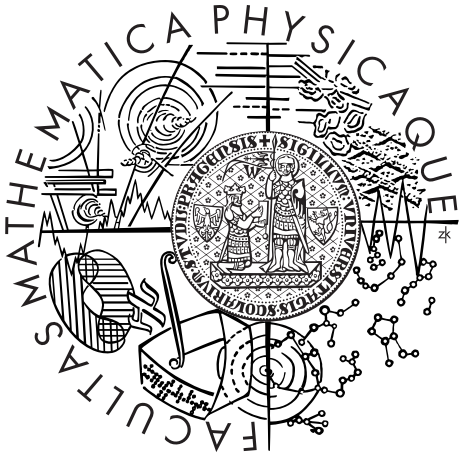

Lukáš Fajt

Prototyp detektoru reaktorových antineutrin

Ústav Částicové a Jaderné Fyziky

Vedoucí diplomové práce: Doc. Ing. Ivan Štekl, CSc.
Studijní program: Fyzika
Studijní obor: Jaderná a Subjaderná Fyzika

Praha 2015

Charles University in Prague
Faculty of Mathematics and Physics

MASTER THESIS

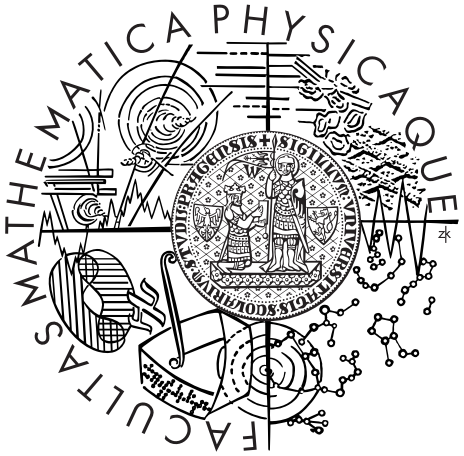

Lukáš Fajt

Prototype of detector for detection of reactor's antineutrinos

Institute of Particle and Nuclear Physics

Supervisor of the master thesis: Doc. Ing. Ivan Štekl, CSc.
Study programme: Physics
Specialization: Particle and Nuclear Physics

Prague 2015

At this point I want to thank several people who made this thesis possible. First and foremost, I would like to express the most sincere gratitude to my supervisor, Doc. Ing. Ivan Štekl, CSc., for being an excellent teacher and a perfect guide and for his continuous support and patience with my questions and ideas. Without his inspiring discussions, invaluable guidance, and endless encouragement this work would have never been fulfilled.

I would also like to extend my gratitude to those with whom I have worked most closely at Institute of Experimental and Applied Physics, my colleagues from the office R. Hodák, M. Špavorová, E. Rukhadze who helped me with construction of the detector itself, benchmark tests at Dubna and Kralupy, and for their cooperation, advise, and friendship.

I would like to thank to our electrical engineers, P. Přidal and P. Mašek, for their never-ending support and willingness to explain to me everything about measurements, electronics and electrical circuits. This was very helpful during electronics testing and I learned a lot from them. I am also grateful to our technician, Jan Hrubý, who helped me a lot with the mechanical design of the holders for testing purposes and taught me a lot about work in a workshop and work with multiple tools during the construction of holders.

Special thanks are also due to the Russian group from JINR, Dubna, led by V. Egorov. It was honour to collaborate with them during my stay in Russia. I learned a lot from them and all of our benchmark tests carried out in Russia were done under their supervision. I benefited a lot from our long discussions.

Finally, a special thank goes to those closest to me. My family, especially my mother, Hana Fajtová, my grandparents, Hana and Ladislav Lochmanovi, and my girlfriend, Michaela Přívratská, have been a constant source of boundless love and support. Without their ever patience, understanding and daily encouragement this work would not have been possible. I love you.

I declare that I carried out this master thesis independently, and only with the cited sources, literature and other professional sources.

I understand that my work relates to the rights and obligations under the Act No. 121/2000 Coll., the Copyright Act, as amended, in particular the fact that the Charles University in Prague has the right to conclude a license agreement on the use of this work as a school work pursuant to Section 60 paragraph 1 of the Copyright Act.

In Prague date ..... signature of the author

Název práce: Prototyp detektoru reaktorových antineutrin

Autor: Lukáš Fajt

Katedra: Ústav Částicové a Jaderné Fyziky

Vedoucí diplomové práce: Doc. Ing. Ivan Štekl, CSs., ÚTEF, ČVUT v Praze

Abstrakt: Předložená diplomová práce souvisí s vývojem komplexního detektoru reaktorových antineutrin, tzv. S^3, který je založen na využití scintilačních detektorů na bázi polystyrenu. Detektor S^3 (rozměry 40 x 40 x 40 cm^3) bude umístěn v blízkosti jaderného reaktoru (5-12 m) a jeho účelem bude měření výkonu reaktoru, izotopového složení jaderného paliva a také ověření hypotézy existence sterilního neutrina pomocí detekce reaktorových antineutrin v procesu IBD.

V rámci předložené diplomové práce byl zkonstruován první prototyp detektoru antineutrin, který je složen z 18-ti scintilačních desek (40 x 20 x 1 cm^3) a příslušné elektroniky. S daným prototypem byly provedeny testy pomocí kosmických mionů. V rámci diplomové práce se také povedlo významně vylepšit energetické rozlišení scintilačních desek optimalizací jejich chemického složení a správnou volbou odrazivého materiálu, což je velmi důležité z hlediska funkčnosti detektoru S^3. Také byly navrhnuty a vyzkoušeny nové metody pro vytvoření obalové vrstvy s obsahem Gd, která je významně lacinější oproti komerčně dodávaným Gd fóliím. Součástí diplomové práce jsou i výsledky MC simulací (optimalizace sběru světla, účinnost detekce reaktorových antineutrin, atd.), které byly získány pomocí programu na bázi Geant4.

Klíčová slova: reaktorová antineutrina, scintilační detektory, Geant4, S^3

Title: Prototype of detector for detection of reactor's antineutrinos

Author: Lukáš Fajt

Department: Institute of Particle and Nuclear Physics

Supervisor: Doc. Ing. Ivan Štekl, CSc., IEAP, CTU in Prague

Abstract: This master thesis is related to the development of the complex detector of reactor's antineutrinos, so called S^3, which is based on the polystyrene scintillation detectors. The detector S^3 (dimensions 40 x 40 x 40 cm^3) will be located in the close vicinity of a nuclear reactor (5-12 m) and its purpose will be to measure reactor's power, isotopic composition of the nuclear fuel and moreover verification of the sterile neutrino hypothesis by detecting reactor's antineutrinos via the Inverse Beta Decay (IBD) interaction.

Within the thesis, the first prototype of the antineutrino detector was constructed. It is composed of 18 scintillation plates (40 x 20 x 1 cm^3) and corresponding electronics. With this prototype the first test with cosmic muons were performed. Within the thesis, the energy resolution of the scintillation plates was significantly improved by the optimization of their chemical composition and selection of the optimal refractive material. The proper energy resolution is very important for the detector functionality. In addition, a new methods for the production of coating layer with Gd were proposed and tested. The newly produced Gd layer is significantly cheaper compared to commercially produced foils. For the thesis, the Geant4-based simulations were developed and results (the optimization of the light collection, the efficiency of the antineutrino detection, etc.) are presented.

Keywords: reactor's antineutrinos, scintillating detectors, Geant4, S^3

Contents

1. Introduction

In the last few years more and more attention in physics is given to neutrino physics. The neutrinos are very abundant, however, elusive particles which are still, more than 80 years after their theoretical prediction and more than 50 years after their experimental observation, surrounded by the large number of questions without answers. It is becoming even worse as new unresolved questions continue to emerge.

For instance, nature of neutrinos, if they follow Majorana or Dirac statistics, what is the true mechanism which gives neutrinos the mass, what is the absolute neutrino mass scale and which neutrino mass hierarchy is the right one, the normal one or the inverted one. In addition, a few years ago, a new very interesting hypothesis about neutrinos appeared. It is a hypothesis of fourth, so called "sterile", neutrino which can explain several unsolved experimental observations which do not coincide with theoretical predictions. A lot of effort was spent on the above mentioned mysteries, however the study of sterile neutrinos is so far only at the beginning.

The sterile neutrino can not be detected directly as it interacts only gravitationally, nevertheless, neutrino oscillations enable to detect sterile neutrinos indirectly. To verify or disprove this hypothetical fourth neutrino, new specialized types of detectors need to be developed. The goal of this work is exactly this task, to develop prototype of the electron antineutrino detector which will be located at variable position very close to a nuclear reactor and allows to make conclusions about sterile neutrinos.

The detector S^3 which is described in this work, is developed in the cooperation with JINR team and is based on the experience with the detector DANSS. Although, an idea behind this experiment is essentially the same, the solid parts of the detector are designed from scratch and thus have to be tested and optimized again, especially a chemical composition, refractive material for wrapping, gadolinium content, electronics, photosensitive elements, etc. During this work, the first functional prototype of this detector was built and the first background data were obtained and analysed.

For better understanding of inner processes and possibility to study behaviour of our detector with respect to the varying parameters the simulations of the detector were developed. Two simulation packages were prepared, one for the study of light propagation and collection in scintillation plates and second for the study of energy deposition inside the detector and spacial and time pattern of the detection process – Inverse Beta Decay (IBD). Developed MC package provides also expected antineutrino detection efficiencies for the detector S^3 and a $1\,m^3$ version.

Moreover, the detector S^3 has many other useful applications: monitoring of the nuclear reactor power (antineutrino flux) and even, under certain circumstances, a fuel composition inside the reactor (antineutrino energy spectrum). In addition, the detector can prevent illegal enrichment and extraction of plutonium, which is a vital part of the nuclear weapons. Thanks to the very short distance to a reactor, cross-sections of weak interactions can be studied as well.

Structure of this thesis is as follows:

- Chapter 1:
  Short introduction and an overview of thesis structure is reviewed.

- Chapter 2:
  The history of neutrino physics is briefly discussed. The position of neutrinos in the Standard Model and introduction into neutrino physics and a few basic information about neutrino sources and neutrino oscillations are presented.

- Chapter 3:
  The experiment S^3, detector design, detection method, etc. are reviewed. Also motivation for building such a detector is described.

- Chapter 4:
  This chapter contains a detailed description of simulations developed directly for the experiment S^3. All parts of the simulation package for the study of light propagation inside one scintillation plate and simulation package for study of energy deposition inside the whole detector are presented. Also, the results of the simulations are reviewed.

- Chapter 5:
  Whole experimental set-up, measuring procedure and benchmark tests carried out at Joint Institute for Nuclear Research (JINR) in Russia by cosmic muons are reviewed. Namely, the results of chemical composition, refractive material and gadolinium layer optimization experiments are given.

- Chapter 6:
  The experiments with individual scintillation plates using mono-energetic source of electrons performed at Envinet factory and construction of the detector S^3 are described. Also, the first measurements with the detector itself are analysed.

- Chater 7:
  All the important conclusions are presented and extended and future plans of experiment S^3 are summarized.

2. Neutrino Physics

Neutrinos are after photons the most abundant particles in the Universe. Scientists say there are about 300 of them in every single cubic centimetre (for baryons it is 10^{-7} per cm^3) [1] which means there are a little bit more than 10^{89} neutrinos in the observable universe. Even more unimaginable is that trillions of neutrinos are penetrating through our bodies every second unnoticed. Actually, neutrinos are so elusive they are able to pass through the earth without a single interaction. In addition, neutrinos are directly connected with the Big Bang which began our universe, with explosions of supernovae and even with the origin of energy in the Sun

Even though neutrinos were discovered more than fifty years ago, they are still one of the most mysterious particles in the particle zoo. It has been proven that neutrinos have to have some tiny, nevertheless, non-zero mass, however, we are still far away from measuring the absolute mass of neutrino. Moreover, we are not even sure about the mechanism of mass generation. Another current issue is the existence of fourth so called "sterile" neutrino [2]. And we know nothing about the nature of the neutrino itself, if it is Majorana or Dirac. And that is just a tip of the iceberg.

This unresolved questions led to a substantial development in experimental as well as theoretical neutrino physics in the last few decades as neutrino oscillations, double β decay, cosmic rays, Seesaw mechanism, CP-violation etc. TU sum up, the neutrino physics is the very exciting and advanced branch of research and its understanding is of vital importance as well as building of new experiments which will probe new frontiers of physics.

Besides, neutrinos are the only particles which have their own song and poem.

Cosmic Gall

Neutrinos they are very small.
They have no charge and have no mass
And do not interact at all.
The earth is just a silly ball
To them, through which they simply pass,
Like dustmaids down a drafty hall
Or photons through a sheet of glass.
They snub the most exquisite gas,
Ignore the most substantial wall,
Cold-shoulder steel and sounding brass,
Insult the stallion in his stall,
And, scorning barriers of class,
Infiltrate you and me! Like tall
And painless guillotines, they fall
Down through our heads into the grass.
...

John Updike (1932–2009)

2.1 What is a Neutrino

The neutrino is electrically neutral fundamental elementary subatomic particle in the Standard Model (Fig. 2.1). The neutrinos have a half-integer spin $\frac{1}{2}$ and are thus a fermions. It is experimentally proved neutrinos have tiny, however, non-zero masses despite predictions of the Standard Model, where they are massless. The masses of neutrinos are more than 500 000 times smaller than mass of the lightest particle – electron, however, the absolute values of their masses are not known yet. Due to lack of an electric charge, neutrino interacts only through weak subatomic force and gravitationally which places high demands on neutrino detectors.

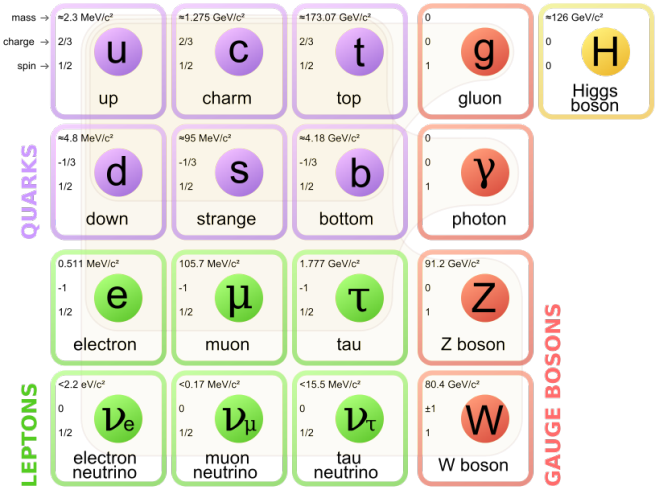

Figure 2.1: Schematic diagram of particles included in the Standard Model. The elementary particles can be divided into groups – leptons (green), quarks (purple), gauge bosons (red) and Higgs boson (yellow). Also names, masses, spins and charges are listed for individual particles. Taken from http://en.wikipedia.org/wiki/Standard_Model.

Experiments suggest that there are three types (flavour states) of weakly interacting neutrinos – electron neutrino ν_e, muon neutrino ν_μ and tau neutrino ν_τ related to three flavours of charged leptons – electron (e^-), muon (μ^-) and tau (τ^-). Charged leptons and corresponding neutrinos form three generations arranged by the increasing mass of leptons. All neutrinos are left-handed and each neutrino flavour is associated with its own antiparticle – antineutrino ($\bar{\nu}$) which is right-handed. In case that a neutrino and its analogous antiparticle are identical we will define neutrinos as Majorana particles.

As was mentioned before, neutrinos interact only through the weak force, excluding gravitational interaction which is barely affecting neutrinos because of their tiny masses. Weak interactions are mediated by $W^{\pm}$ and Z^0 bosons that are much more heavier than protons and their masses are in Standard Model explained by the Higgs mechanism. As a result of their large masses, W and Z bosons ($m_W = 80.4\,\mathrm{GeV}$ and $m_Z = 91.2\,\mathrm{GeV}$) have short lifetimes (under $10^{-24}\,\mathrm{s}$) which results in very short range of weak interactions (about $10^{-17}\,\mathrm{m}$) [3]. Therefore, you need either enormous huge detectors placed underground or huge fluxes of neutrinos for sufficient statistics.

2.2 A Brief History of Neutrinos

As we already mentioned the neutrino was first predicted in 1930 by the theorist Wolfgang Pauli who proposed such a hypothetical construct of almost non-interacting particle in order to solve the beta decay crisis. Previously it was assumed that beta decay is only three particle interaction therefore electron should be produced with fixed energy in contrast to observed data from experiments where electron has a continuous energy spectrum. The discrepancy between theory and experiment was by some interpreted as a violation of energy conservation.

Pauli undertook a very courageous step and proposed the existence of a neutral particle which had not been detected yet. He did so at the conference where he did not attend by a letter [4]

> Dear Radioactive Ladies and Gentlemen,
>
> As the bearer of these lines, to whom I graciously ask you to listen, will explain to you in more detail, because of the "wrong" statistics of the N- and Li-6 nuclei and the continuous beta spectrum, I have hit upon a desperate remedy to save the "exchange theorem" of statistics and the law of conservation of energy. Namely, the possibility that in the nuclei there could exist electrically neutral particles, which I will call neutrons, that have spin $\frac{1}{2}$ and obey the exclusion principle and that further differ from light quanta in that they do not travel with the velocity of light. The mass of the neutrons should be of the same order of magnitude as the electron mass and in any event not larger than 0.01 proton mass. - The continuous beta spectrum would then make sense with the assumption that in beta decay, in addition to the electron, a neutron is emitted such that the sum of the energies of neutron and electron is constant.
>
> ...
>
> signed W. Pauli

The only thing that has changed since Pauli's letter is the name of this particle which was modified by Enrico Fermi to neutrino – little neutron in Italian. Thus thanks to Pauli we know that the β decay is actually four particle interaction and can be written as

$$(\mathrm{A}, \mathrm{Z}) \rightarrow (\mathrm{A}, \mathrm{Z}+1) + \mathrm{e}^{-} + \bar{\nu_e} \ , \tag{2.1}$$

or in the case of neutron

$$\mathrm{n} \rightarrow \mathrm{p} + \mathrm{e}^{-} + \bar{\nu_e} \ . \tag{2.2}$$

After a while, Fermi took the advantage of this idea and in 1934 formulated the first theory of weak interaction based on the theory of quantum electrodynamics. In this so called Fermi's interaction there were not any particles carrying weak force, it was suggested that it is a direct interaction of four fermions described by Lagrangian density [5]

$$\mathcal{L}_{int} = -G(\bar{\psi_p}\gamma^\mu\psi_n)(\bar{\psi_e}\gamma_\mu\psi_\nu) + \text{h.c.} \ , \tag{2.3}$$

where γ^μ are standard Dirac matrices, G is a coupling constant and ψ's are four-component spinor fields.

This theory has been further developed, expanded to more types of leptons and enriched with the Cabibbo angle. This led to a new version of the interaction Lagrangian (so called Feynman–Gell-Mann Lagrangian) [5]

$$\mathcal{L}_{int} = -\frac{G_F}{\sqrt{2}} J^\rho J^\dagger_\rho \ , \tag{2.4}$$

where G_F is a coupling constant and J_ρ are the charged currents and equal

$$J_\rho = \bar{\nu_e}\gamma_\rho(1-\gamma_5)e + \bar{\nu_\mu}\gamma_\rho(1-\gamma_5)\mu + \bar{u}\gamma_\rho(1-\gamma_5)(d\cos\Theta_C + s\sin\Theta_C) \ , \tag{2.5}$$

where all fermions fields are denoted by corresponding particle label and Θ_C is the Cabibbo angle.

Even though, this Lagrangian provided very strong apparatus for the accurate calculations of many processes, it was shown that there are also processes which exhibit strange behaviour at higher energies. For example, cross section of neutrino-electron elastic scattering in the lowest order is proportional to the $E^2_{c.m.}$ [1]. Such a power-law behaviour violates the S-matrix unitarity and thus causes non-renormalizability of this theory.

To solve this crisis a new theory of weak interactions were proposed. This theory introduces Intermediate Vector Bosons (IVB) W^+ and W^- and an appropriate Lagrangian

$$\mathcal{L}_{int} = -\frac{g}{2\sqrt{2}}(J^\mu W^+_\mu + J^{\mu\dagger} W^-_\mu) \ , \tag{2.6}$$

where $W^\pm$ are vector fields of corresponding vector bosons ($W^\pm$). This theory repairs deficiencies of the old theory, however, the power-law behaviour was still present, although in another processes. And finally in 1968, the weak interaction was unified with the electromagnetic force to the electro-weak force, which is renormalizable, by S. Glashow, S. Weinberg, and A. Salam.

In 1959, long twenty-eight years after the theoretical prediction of the neutrino, the first experiment of direct neutrino observation was realized by Clyde L. Cowan and Frederick Reines [6] who measured electron antineutrinos emerging from a nuclear reactor via Inverse Beta Decay (IBD) interaction

$$\bar{\nu_e} + \mathrm{p} \rightarrow \mathrm{n} + \mathrm{e}^+ \ . \tag{2.7}$$

The two remaining neutrinos were detected in 1962 (muon neutrino) at Brookhaven National Laboratory [7] and in 2000 (tau neutrino) by DONUT experiment [8] finally completing hunt for fermions in the Standard Model.

[1] $E_{c.m.}$ is the full centre-of-mass energy

2.3 Neutrino Sources

There are a lot of places, not only in the universe but also on the Earth, where neutrinos can be created even thought they always have to be produced in the weak interactions. For complete comprehension of all properties and behaviour of neutrinos we have to study different flavours and energies of neutrinos, it is the only approach how we can obtain a complete picture. Naturally, creation of so many various types and energies is impossible in one kind of sources. The sources of neutrinos may be classified into two big categories (taken from [9]):

- Natural sources
- Artificial sources.

The most important natural sources are the Sun, our atmosphere and the huge number of neutrinos was created during the Big bang and can be creates during every Supernova.

In the core of the sun $3.86{\cdot}10^{26}$ joules are released every second providing sufficient amount of energy for life on the Earth. This energy is created in PP chain described within Standard Solar Model (SSM), when four protons are gradually transformed to helium

$$4\mathrm{p} \rightarrow^{4} \mathrm{He} + 2\mathrm{e}^{+} + 2\nu_e + 25\,\mathrm{MeV}\ . \tag{2.8}$$

Neutrinos created in the core penetrate through the Sun in less than two seconds and provide solar neutrino flux of $4{\cdot}10^{10}$ neutrinos/cm^2/s at the Earth with maximum energy of about 18 MeV.

The atmospheric neutrinos are created by cosmic rays when interact with the atoms of our atmosphere and produce non-stable mesons which subsequently decay and produce electron neutrinos, muon neutrinos and antineutrinos. The atmospheric neutrinos are excellent probes for neutrino oscillations when ν_μ/ν_e ratio and up-down asymmetry in the number of detected neutrinos is studied. The energy of produced neutrinos allows to study Δm^2 down to $10^{-5}\,\mathrm{eV}^2$.

Relic neutrinos, or in other words neutrinos which are remains of the Big Bang (BB), are quite similar to Cosmic Microwave Background (CMB) radiation – they are almost everywhere in the universe (340 ν/cm^3) and their energy is extremely small (10^{-4} eV) [1]. Right after the BB, all elementary particles were in thermal equilibrium, however, as the Universe grew and its temperature decreased it was still harder and harder for neutrinos to stay in this equilibrium. Finally, few seconds after the BB (in contrast with 379 000 years for CMB) neutrinos decoupled from matter and started propagate freely through the matter. Even thought they have not been detected yet in any experiment because of their tiny mass, they are one of the assumed candidates for the Dark Matter (DM).

Another source of neutrinos is supernova which is stellar explosion of incredible brightness and power, changing stars in their final life stage into the neutron stars or the black holes. During Supernova 99 % of relased energy is taken away by neutrinos. Theory of neutrinos created in such a huge stellar explosions was confirmed in 1987, when about 25 neutrinos from supernova 1987A were observed in time period shorter than 13 seconds at three different underground experiments – Kamiokande, IMB and Baksan.

The most important artificial sources of neutrinos are particle accelerators and nuclear reactors. Particle accelerators are able to produce neutrino beam with different energies and flavours. The main idea is to collide particles with a fixed target to produce pions and kaons which decay in flight and produce also neutrinos. Then the whole beam is guided through the huge amount of shielding which suppresses all other particles thus creating pure neutrino or antineutrino beam. Such a beam is usually studied in detectors far away from an accelerator (T2K, Opera, NOvA).

Much more frequent artificial source of neutrinos is a nuclear reactor which produces a huge number of electron antineutrinos during the fuel fission. These antineutrinos are actually a by-product of human energy production, however are also ideal for scientific research (Daya Bay, KamLAND). Much more about this source of electron antineutrinos is written in Section 3.

2.4 Neutrino Oscillations

Neutrinos have, unlike other leptons, a special property which is called flavour oscillations [3]. When we talk about neutrinos we actually mean their flavour eigenstates which are produced in the weak interactions. For instance, if a neutrino is produced together with an electron we speak about electron neutrino etc. However, these flavour eigenstates do not coincide with the mass eigenstates. It means that every flavour eigenstate is a linear combination of different mass eigenstates, as it is with the quarks.

Since every mass eigenstate propagates through space with a different velocity at constant energy, the flavour states can change during the propagation through space. It means that neutrino originated as electron neutrino can be detected as muon or tau neutrino and vice versa.

The neutrino flavour states are labeled as $|\nu_\alpha\rangle$ (α = e, μ, τ) and neutrino mass states as $|\nu_j\rangle$ (j = 1, 2, 3). Every neutrino flavour state can be expressed as a linear combination of mass states and vice versa

$$|\nu_\alpha\rangle = \sum_{\mathrm{j}=1,2,3} U_{\alpha j}|\nu_j\rangle \ , \tag{2.9}$$

where **U** is the PMNS (Pontecorvo-Maki-Nakagawa-Sakata) mixing matrix which provides connection between flavour and mass states. This matrix can be written as

$$\mathbf{U} = \begin{pmatrix} \mathrm{c}_{12}\mathrm{c}_{13} & \mathrm{s}_{12}\mathrm{c}_{13} & \mathrm{s}_{13}\mathrm{e}^{-i\delta} \\ -\mathrm{s}_{12}\mathrm{c}_{23} - \mathrm{s}_{13}\mathrm{s}_{23}\mathrm{c}_{12}\mathrm{e}^{i\delta} & \mathrm{c}_{12}\mathrm{c}_{23} - \mathrm{s}_{12}\mathrm{s}_{13}\mathrm{s}_{23}\mathrm{e}^{i\delta} & \mathrm{s}_{23}\mathrm{c}_{13} \\ \mathrm{s}_{12}\mathrm{s}_{23} - \mathrm{s}_{13}\mathrm{c}_{12}\mathrm{c}_{23}\mathrm{e}^{i\delta} & -\mathrm{s}_{23}\mathrm{c}_{12} - \mathrm{s}_{12}\mathrm{s}_{13}\mathrm{c}_{23}\mathrm{e}^{i\delta} & \mathrm{c}_{13}\mathrm{c}_{23} \end{pmatrix} \ ,$$

where $\mathrm{c}_{jk} = \cos\theta_{jk}$, $\mathrm{s}_{jk} = \sin\theta_{jk}$, and δ is the CP-violating phase introduced by Dirac. The most general form of the relation for oscillation probability is following [10]

$$P(\nu_\alpha \to \nu_\beta) = \delta_{\alpha\beta} - 4\sum_{i>j} \Re(U^*_{\alpha i}U_{\beta i}U_{\alpha j}U^*_{\beta j}) \sin^2(\Delta m^2_{ij}\frac{L}{4E}) + 2\sum_{i>j} \Im(U^*_{\alpha i}U_{\beta i}U_{\alpha j}U^*_{\beta j}) \sin(\Delta m^2_{ij}\frac{L}{2E}) \ . \quad (2.10)$$

If δ is equal zero the imaginary part of the equation is also zero and moreover this equation substantially simplifies if just two neutrino case is assumed which is very often in neutrino experiments. Then oscillation probability for $\alpha \neq \beta$ is

$$P(\nu_\alpha \to \nu_\beta) = \sin^2(2\theta)\sin^2(\Delta m^2 \frac{L}{4E_\nu}) \ . \quad (2.11)$$

The angles θ_{jk} are mixing angles and carry information about relative abundance of particular flavour eigenstates in the mass eigenstates. $\Delta m^2_{ij} = m^2_i - m^2_j$ are the mass squared differences of mass eigenstates and as the oscillations were verified in countless experiments they show that at least one neutrino has to have non-zero mass.

Parameters from "12-sector", Δm^2_{12} and θ_{12} were successfully measured from the solar neutrinos. Parameters from the "23-sector" were measured thanks to atmospheric neutrinos and parameters from the "13-sector" are studied right now on the reactor neutrinos. Figure 2.2 presents the illustration of currently known values of parameters of the neutrino oscillations. The best known values of oscillation parameters are also shown in Table 2.1.

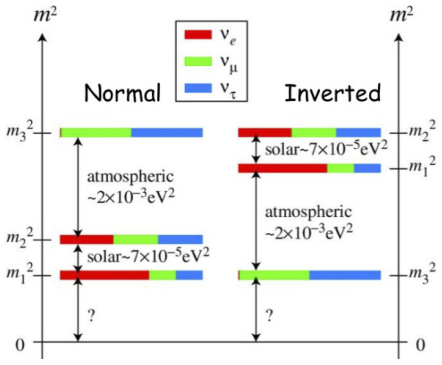

Figure 2.2: Schematic representation of the best currently known values of oscillation parameters for both mass hierarchies. Taken from https://neutel11.wordpress.com/2011/03/16/neutrino-mass-models-by-steve-king/.

In the last few years, hypothesis of sterile neutrino (so called 3+1 scenario) or neutrinos (so called 3+2 or 3+3 scenarios) was developed as a response to experimental observations which are not compatible with just three neutrinos. It means that is possible that there exist one, two, or three additional neutrinos which do not interact weakly, however enables weakly interacting neutrinos oscillate to them.

Mass of such a hypothetical sterile neutrinos would be huge in comparison with active weakly interacting neutrinos thus sterile neutrino will be composed mainly from a new mass state $|\nu_4\rangle$ with mass $m_4 \gg m_1, m_2$, and m_3. So the oscillation length would be very short, in order of meters.

Parameter	Value
$\sin^2(2\theta_{12})$	0.846 ± 0.021
$\sin^2(2\theta_{23})$ (NH)	$0.999^{+0.001}_{-0.018}$
$\sin^2(2\theta_{23})$ (IH)	$1.000^{+0.000}_{-0.017}$
$\sin^2(2\theta_{13})$	$(9.3 \pm 0.8) \times 10^{-2}$
Δm^2_{21}	$(7.53 \pm 0.18) \times 10^{-5}\,\mathrm{eV}^2$
Δm^2_{32} (NH)	$(2.44 \pm 0.06) \times 10^{-3}\,\mathrm{eV}^2$
Δm^2_{32} (IH)	$(2.52 \pm 0.07) \times 10^{-3}\,\mathrm{eV}^2$

Table 2.1: The best currently known values of neutrino oscillations parameters for Normal Hierarchy (NH) and Inverted Hierarchy (IH) [11].

In 3+1 scenario the probability of neutrino oscillation equals [12]

$$P(\nu_\alpha \to \nu_\beta) = \sin^2(2\theta_{\alpha\beta}) \sin^2(\Delta m^2_{41} \frac{L}{4E}) \ , \tag{2.12}$$

where $\sin^2(2\theta_{\alpha\beta}) = 4|U_{\alpha 4}|^2|U_{\beta 4}|^2$ if $\alpha \neq \beta$. The oscillation probability for $\alpha = \beta$ is

$$P(\nu_\alpha \to \nu_\alpha) = 1 - \sin^2(2\theta_{\alpha\alpha}) \sin^2(\Delta m^2_{41} \frac{L}{4E}) \ , \tag{2.13}$$

where $\sin^2(2\theta_{\alpha\alpha}) = 4|U_{\alpha 4}|^2(1 - |U_{\alpha 4}|^2)$.

2.5 The Present State of Reactor $\bar{\nu_e}$ Detection

There are two main categories of reactor $\bar{\nu_e}$ research. The first category specializes on the measurement of θ_{13} value and uses two detectors, near and far, located hundreds of metres away from a nuclear reactor. The second category would like to solve so called Reactor Anomaly and usually operates with just one detector which is located very close to the nuclear reactor (less than 20 m). There is one thing common for both categories and that is the detection method, which is in almost all cases Inverse Beta Decay (IBD). It is also true, that experiments from one category can often measure parameters from the second category. These two categories will be described in detail in the following two sections.

2.5.1 θ_{13} Category

The knowledge of θ_{13} value as accurate as possible is very important for further study of neutrinos, namely CP-violation and the mass hierarchy. This angle can be obtained relatively easily[2] by measuring the disappearance of electron antineutrinos, which can be on short distances (~ 1 km) expressed as

$$P(\bar{\nu_e} \to \bar{\nu_e}) = 1 - \sin^2 2\theta_{13} \sin^2(1.27\,\Delta m^2_{31} \frac{L(km)}{E_\nu(GeV)}) \ . \tag{2.14}$$

[2]If the Δm^2_{31} is known accurate enough

Currently, there are three main experiments measuring the mixing angle θ_{13}: Double Chooz, RENO, and Daya Bay [13]. All these experiments use IBD and tonnes of Gd-doped liquid scintillator and also use at least two detectors in order to avoid lack of knowledge about absolute antineutrino flux.

The Double Chooz experiment is located in France and its two detectors are set 400 and 1050 m away from the two 4.27 GW_{th} reactors. The far detector is located in the cavern with 300 m.w.e. The Double Chooz collaboration already released their preliminary results for $\sin^2 2\theta_{13} = 0.090^{+0.032}_{-0.029}$ [14].

The RENO experiment is located in South Korea with two detectors 294 and 1383 metres away from six reactors. Also RENO collaboration released their results of $\sin^2 2\theta_{13} = 0.100 \pm 0.010\,(\text{stat}) \pm 0.015\,(\text{sys.})$ [15].

So far the most accurate value of θ_{13} mixing angle provided experiment Daya Bay located in China. It consists from eight detectors divided into three groups located up to 1.9 km from six nuclear reactors. Their latest result is $\sin^2 2\theta_{13} = 0.084 \pm 0.005$ [16].

Measurements of the θ_{13} from all aforementioned experiments are shown simultaneously in Fig. 2.3.

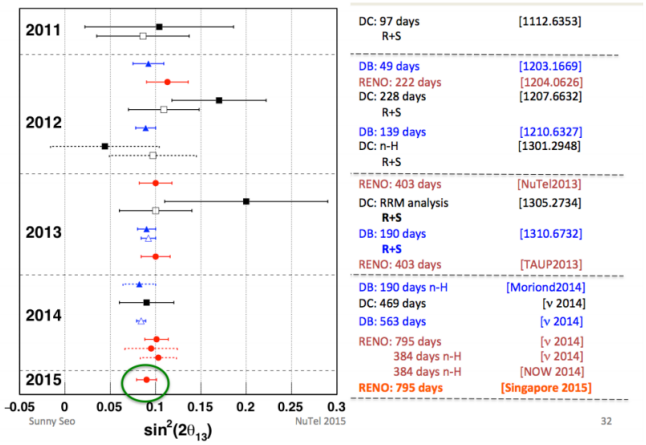

Figure 2.3: All measurements of the θ_{13} from Double Chooz, RENO, and Daya Bay experiments [17] in different stages of their data taking.

2.5.2 Reactor Anomaly Category

On the other hand, experiments from Reactor Anomaly Category are much smaller and lighter, they are much closer to a nuclear core, use just one detector, and depend on the knowledge of an absolute electron antineutrino flux. These experiments should be able to verify or disprove theory of fourth neutrino. Moreover, these detectors should be able to measure reactor power, to estimate isotopic composition in the reactor, provide method how to prevent illegal plutonium misuse and also improve values of antineutrino cross sections. These are the reasons why, in the last years, a lot of new experiments in this category have been started. More about the fourth neutrino and isotopic composition can be found in Section 3.

The list of all currently data taking or planed experiment is shown in Tab. 2.2. The name of the experiment and the country where the experiment is located,

Name	Det. Met.	Mass	Seg.	Dep.	Dist.	P_{th}	Status
Nucifer (FR)	LS+Gd	0.75	1	13	7	70	work
DANSS (RU)	SS+Gd	1	2500	50	9.7-12.2	3000	mount
Neutrino4 (RU)	LS+Gd	2.2	2	few	6-12	100	mount
STEREO (FR)	LS+Gd	1.75	1	18	8.8-11.2	50	R&D
SoLid (UK)	^{6}LiF:ZnS	3	64	10	6-8	45-80	R&D
Hanaro (KR)	LS+Gd	0.5	1	few	6	30	R&D
Prospect (US)	LS+Gd	1,10	1	few	4,18	20-120	R&D
NuLat (US)	SS+^{10}B	1	3375	few	3-8	1500	R&D
Poseidon (RU)	LS+Gd	1.5	5	few	5-15	100	MC
CARR (CN)	LS+Gd	~ 1	1	few	7 & 15	60	MC

Table 2.2: The review of all currently data taking or planed experiment from the Reactor Anomaly branch [18].

detection method (LS - liquid scintillator, SS - solid scintillator, Gd - gadolinium), mass of the active volume in tons, segmentation, depth of the experiment in the m.w.e., distance from the core in metres, thermal power of a nuclear core in MW and the status of the experiment are listed.

In majority of listed experiments the liquid scintillator is used as in the experiments from θ_{13} category, however commercially operated reactors are not compatible with liquid scintillators in close vicinity due to the highly flammable nature of these scintillators. Also more compact nuclear reactors are preferred because of the washing out of the oscillation pattern caused by large dimensions of a core. These experiments also use IBD for detection of the incoming antineutrinos.

3. The detector S^3

During a fission reaction, neutron-rich nuclei are produced, which finally undergo β decay. After one fission about 6 $\bar{\nu}_e$ is produced together with $\sim 200\,\mathrm{MeV}$ of released energy. Every second more than 10^{21} antineutrinos are produced in the fission reactions inside a typical $3\,\mathrm{GW}_{th}$ nuclear reactor thus forming the most intensive man-controlled source of antineutrinos ideal for neutrinos research, for instance: oscillations, mass hierarchy, existence of another types of neutrinos.

A lot of experiments for detection of reactor's antineutrinos are in operation right now (e.g. Daya Bay, Double Chooz, and RENO) and under construction as well (e.g. JUNO, and RENO-50) and a large number of ground breaking results were already published (value of θ_{13} – see Sec. 2.5.1).

Detectors in these experiments are almost always liquid scintillation detectors with huge dimensions and ktones of scintillator which places high demands on price, number of staff, time, and complexity. Moreover some neutrino properties can be tested with much higher efficiency in the close vicinity of the reactor, however, power plants are well-known for their high level of security and the impossibility of using flammable or otherwise dangerous compounds in the close vicinity of a reactor core which exclude usually used liquid scintillators from detection on a very short baselines ($\sim 10\,\mathrm{m}$ from a nuclear core).

That is why our approach to detector construction, based on design and experience of our Russian colleagues from JINR, is completely opposite from these huge antineutrinos detectors, since we are developing compact antineutrino detector with volume just $1\,\mathrm{m}^3$ composed of plastic scintillators which are relatively cheap, easy to maintain and completely non-toxic as well. However, construction of such a detector from scratch is a very complicated task, thus only the prototype with dimensions 40 x 40 x $40\,\mathrm{cm}^3$ is created at first. This prototype is called S^3.

The decrease in detection rate due to smaller dimensions of detector S^3 is generously compensated by uniquely short distance ($\sim 10\,\mathrm{m}$) from commercially used nuclear reactors as the neutrino flux produced in the core is inversely proportional to the square of the distance ($\propto 1/d^2$), so the neutrino flux at 10 metres is 10 000 times higher than at 1 km. Since neutrino flux is strongly correlated with nuclear power station power, detectors like S^3 have applications in both industry and research (applied as well as basic).

3.1 Detector design

S^3 is the second generation of a detector prototype for detection of reactor's antineutrinos based on experience with Russian experiment DANNSino [19, 20] and developed in direct cooperation with colleagues from Joint Institute for Nuclear Research (JINR), Dubna. S^3 consists of 80 basic detection elements (Figs. 3.1(a), 3.2) – organic plastic scintillator plate based on polystyrene with luminescent additives pTP $2\,\%_{wt}$ and POPOP $0.05\,\%_{wt}$ (see Sec. 5.1) with dimensions 40 x 20 x $1\,\mathrm{cm}^3$ produced by Envinet company [21].

Each plate has 19 grooves[1], parallel to the longest side, equipped by the

[1] 10 fibres is attached to the PMT and 9 is attached to the SiPM

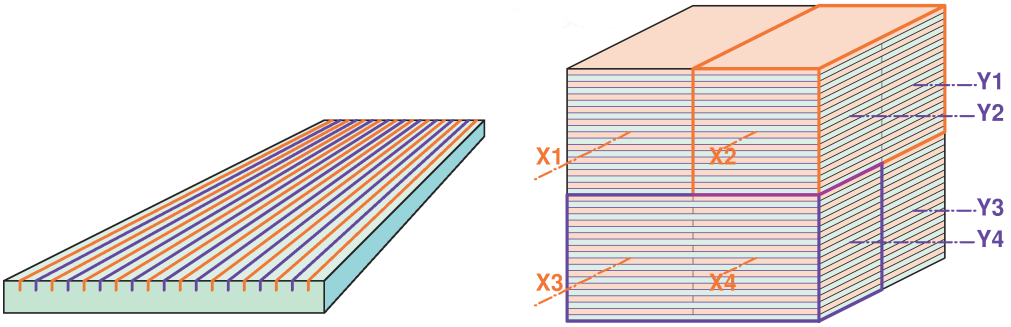

(a) (b)

Figure 3.1: Detector S^3 construction design. a) One basic detection element with dimensions 40 x 20 x 1 cm^3 and 19 grooves for WLS fibres. b) Detector S^3 with dimensions 40 x 40 x 40 cm^3 and 8 electronic channels (X1-X4, Y1-Y4).

WaveLength Shifting (WLS) Kuraray fibres Y-11 with $\oslash$ 1.0 mm glued with two component clear epoxy glue. The fibres provide homogeneous collection of scintillation light across the plate and also guide light to the photo sensitive elements (PMT, SiPM). Moreover, each plate is wrapped into four layers (200 μm each) of teflon reflective layer (see Sec. 5.2) and a layer with gadolinium (see Sec. 5.3) ensuring the conversion of neutrons to gammas via (n,γ) reactions (described in detail in Section 3.2).

Overall dimensions of S^3 are 40 x 40 x 40 cm^3 (Fig. 3.1(b)) with eight channels. Every channel will be connected to the Hamamatsu R7600U-300 PhotoMultiplier Tube (PMT). Signals from these PMTs will be processed by a specially develop electronics. The entire detector will be surrounded by shielding whose optimal composition will have to be subjected to testing, however, proposed shielding, from outside to inside, is following: 8 cm of polyethylene to stop thermal neutrons from a nuclear reactor, 10 cm of 100-year lead to shield detector against gamma radiation, and another 8 cm layer of polyethylene, this time borated, to suppress fast neutrons produced by cosmic muons in the lead shielding which are the main source of the background signal.

Detector with shielding will be, after ground and background laboratory measurements and after the measurements of shielding influence, transported to the Kalinin Nuclear Power Plant (KNPP) in Russia and installed under a typical water cooled and moderated nuclear reactor WWER-1000 with thermal power 3 GW_{th}. Detector itself will be installed in the room located exactly under reactor (see Fig. 3.3) which provides, together with spent fuel pool and reactor vessel, another additional shielding against cosmic rays. All in all, detector will be shielded by $\simeq$ 50 m w.e. which stop cosmic fast neutrons completely and suppress cosmic muons by a factor of $\simeq$ 6 [19].

3.2 Detection Method

Electron antineutrinos are most often, as well as in our case, detected via Inverse Beta Decay (IBD) interaction

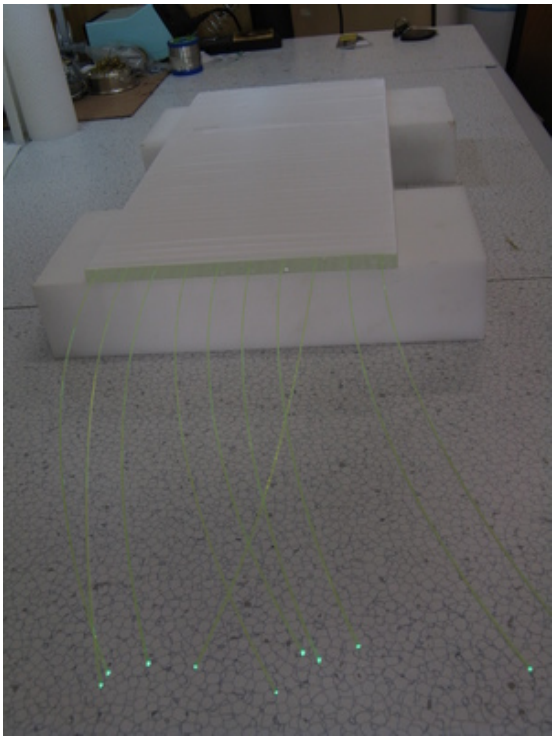

Figure 3.2: Scintillation plate with glued WLS fibres and four layers of 200 μm teflon prepared for testing.

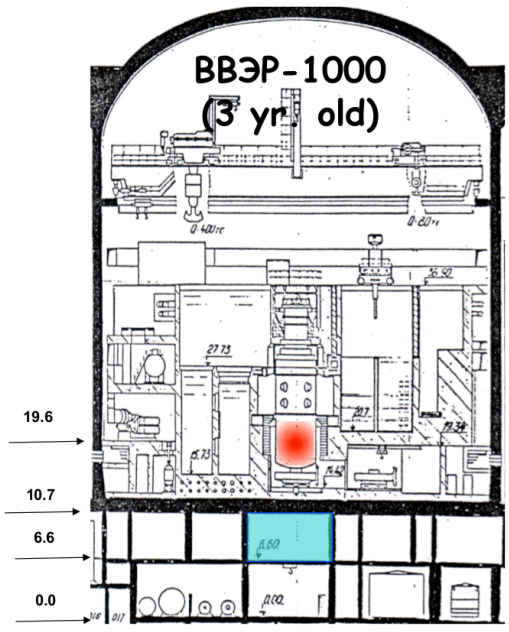

Figure 3.3: Ilustration of reactor WWER-1000 with reactor core in red and with room where S^3 will be located in blue [22].

$$\bar{\nu_e} + \mathrm{p} \rightarrow \mathrm{n} + \mathrm{e}^+ \tag{3.1}$$

when incoming antineutrino interacts with one of the protons inside a detector and creates neutron and positron. This interaction has energy threshold 1.806 MeV in the laboratory frame. The positron losses energy in a scintillation plate and finally annihilates thus creating two gammas. The emerging neutron is thermalized in the volume of detector by scattering on hydrogen and then captured on gadolinium layer producing the cascade of gammas with the summary energy $E_{\sum} = 8\,\mathrm{MeV}$. As a result we will detect IBD in the detector in two signals – prompt signal (positron and annihilation gammas) and delayed signal (gammas from neutron capture) separated by $\tau \sim(1 - 100)\,\mu\mathrm{s}$. The IBD provides very typical time and spacial pattern in our detector (see Fig. 3.4) which can be used to background reduction and improvement of S/B ratio.

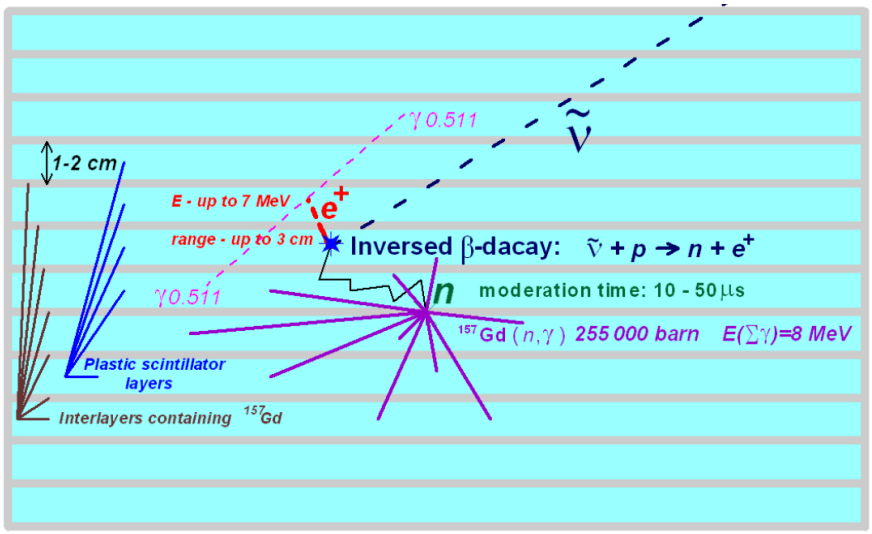

Figure 3.4: Schematic ilustration of the IBD interaction in a scintillator based detector [22].

Almost all energy of antineutrino is carried away by positron, thus enabling neutrino energy reconstruction, in the first order, from the prompt signal

$$E_{\bar{\nu}_e} = E_p + 0.8\,\mathrm{MeV}\ , \tag{3.2}$$

if we detect whole energy of annihilation gammas. The neutron's energy is negligible ($\sim 50\,\mathrm{keV}$) compared to energy of positron, on the other hand, the neutron is carrier of momentum, which means that proceeds almost in the direction of incoming antineutrino. Angular distribution of positrons is slightly backward peaked. These facts put strict demands on the detector energy resolution and segmentation. Through a tiny cross section of IBD [23]

$$\sigma_{tot}^{(0)} = \sigma_0(f^2 + 3g^2)E_e^{(0)}p_e^{(0)} = 0.0952\left(\frac{E_e^{(0)}p_e^{(0)}}{1\,\mathrm{MeV}^2}\right)\cdot 10^{-42}\,\mathrm{cm}^2\ , \tag{3.3}$$

where $f = 1$ and $g = 1.26$ are weak coupling constants, $E_e^{(0)}$ and $p_e^{(0)}$ are positron energy and momentum and σ_0 is normalizing constant, strict demands are put also on a detector size and distance from a nuclear reactor.

The number of detected antineutrinos is heavily dependent on the size of detector. With increasing volume there are two reasons for increase in the number of detection. The number of detected antineutrinos with respect to their energy is given as [24]

$$n(E_{\bar{\nu}_e}) = N_p \, \sigma(E_{\bar{\nu}_e}) \, \Phi(E_{\bar{\nu}_e}) \ , \tag{3.4}$$

where N_p is the number of target protons in the detector, $\sigma(E_{\bar{\nu}_e})$ is the IBD cross-section (Eq. 3.3) and $\Phi(E_{\bar{\nu}_e})$ is reactor $\bar{\nu}_e$ flux. With increasing volume the number of N_p is increased thus resulting in the increase of antineutrino detections. Furthermore, with bigger volume the detection efficiency is improved as well which is given by a larger volume, where corresponding gammas from annihilation and neutron capture can be detected.

Very small distance of the detector S^3 from a nuclear reactor results in antineutrino flux $\Phi_{\bar{\nu}_e} \sim 8 \cdot 10^{13} \bar{\nu}_e/\mathrm{cm}^2/\mathrm{s}$ at a distance of 10 m thus causing ~ 300 antineutrino detections in the detector per day.

The authors of paper [19] as well as author of presentation [25] pointed out that quite a large number of antineutrino-like events is produced by cosmic muons which produce fast neutrons during the interactions with heavy materials located close to the detector. The neutron can partly mimic the time pattern of IBD, however can be recognized by spacial pattern easily.

3.3 Motivation

"Why are we constructing such a detector?" or in other words "What is it good for?". There are many useful applications of detector S^3 in both applied research and basic research, however, the main two are:

- Verification or refutation of a sterile neutrino hypothesis
- Online monitoring of reactor core power and isotopic composition of nuclear fuel.

Both will be described in detail in the following sections. Moreover, electron antineutrino cross sections and flux could be studied with this detector.

3.3.1 Sterile Neutrino

In 2011, the reanalysis of the reactor antineutrinos spectra [26, 27], performed by two different groups, led to the formulation of the Reactor Antineutrino Anomaly (RAA) [28], which indicates the discrepancy between measured and expected antineutrino fluxes on short baselines (see Figs. 3.5 and 3.6). This discrepancy appears to favor the existence of the fourth "sterile" neutrino with $|\Delta m^2| > 1\,\mathrm{eV}^2$.

One of the approaches how to confirm or reject this hypothesis is a high sensitive antineutrino detector located close to the reactor. The detector S^3 due to its construction will be able to measure antineutrino flux at the very short distances from a nuclear reactor ($\sim 10\,\mathrm{m}$) and thus is ideal for this task.

Much has been written about sterile neutrino, nevertheless, the most comprehensive overview is 281-page book "Light Sterile Neutrinos: A White Paper" [2]. This book contains theoretic background as well as experimental observations.

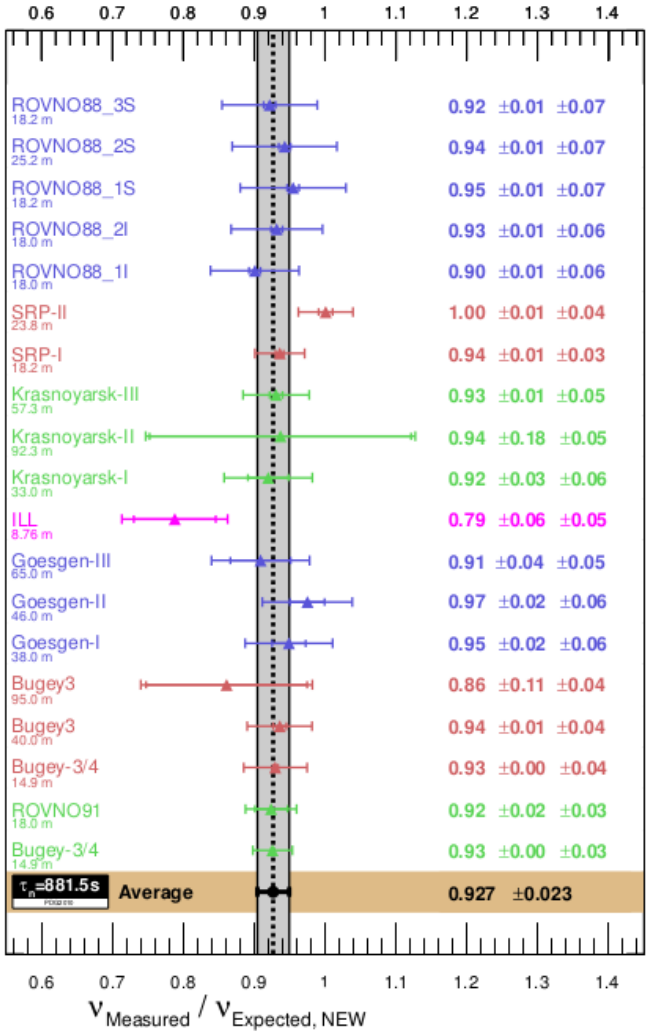

Figure 3.5: Weighted average (with correlations) of 19 measurements of reactor neutrino experiments operating at short baselines [2].

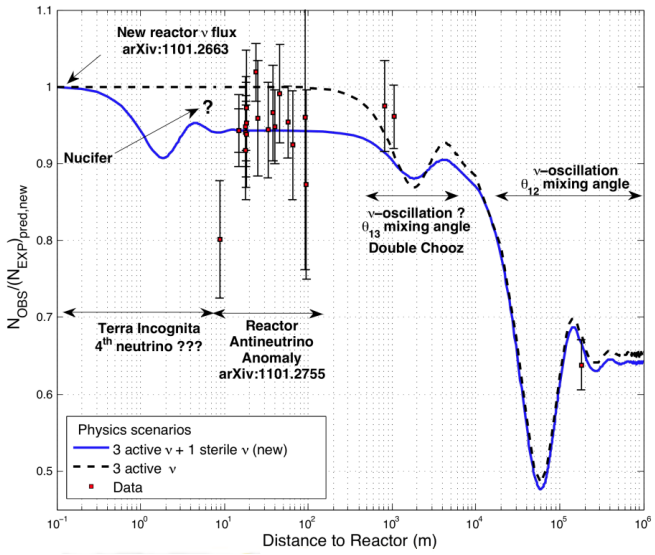

Figure 3.6: Ratio of observed to expected antineutrino detections depending on the distance from the source. The experimental results are compared to the prediction without oscillation, taking into account the new antineutrino spectra, the corrections of the neutron mean lifetime, and the off-equilibrium effects. The mean averaged ratio including possible correlations is 0.943 ± 0.023. The dashed line shows a possible 3 active neutrino mixing solution, with $\sin^2(2\theta_{13}) = 0.06$. The blue line displays a solution including a new neutrino mass state, such as $|\Delta m^2_{new}| \gg 1\,\mathrm{eV}^2$ and $\sin^2(2\theta_{new}) = 0.12$ (for illustration purpose only) [29].

The sterile neutrino, if it exist, is the fourth type, or "flavour", of neutrinos, which unlike its three active companions does not interact weakly, that is why, is almost completely undetectable. The only possibility how to prove its existence is due to neutrino oscillations, which would cause decrease in flux of the remaining types of neutrinos as is observed in RAA. However, RAA is not the only hint for a sterile neutrino. In the last few years, a new anomalies have appeared, which can be explained by the existence of the sterile neutrino as well. However, the experimental observation of the sterile neutrino has still not been done.

There are also theories which predict more than just one sterile neutrino [30]. These models are collectively referred as 3+N models, where the first number represents the number of active weakly interacting neutrinos, which was confirmed by Z boson decays at LEP, and the second number N represents the number of sterile neutrinos. The results show that data are much better consistent with scenarios when three or at least two sterile neutrino exist.

Besides, the sterile neutrino differs from its colleagues by much bigger mass squared splitting, which is expected to be higher than $|\Delta m^2_{new}| > 1\,\mathrm{eV}^2$. The sterile neutrinos are one of the candidates for dark matter particles. Allowed regions and the most probable value in the $\sin^2(2\theta_{new}) - (\Delta m^2_{new})$ plane obtained by the combination of the reactor neutrino experiments, Gallex and Sage calibration sources experiments and the ILL and Bugey-3 energy spectra are shown in Fig. 3.7.

The main strategy for sterile neutrino measurement is to use two S^2 detectors, which are as similar as possible, and measure $\bar{\nu}_e$ flux at two distances from core simultaneously. Second strategy is to use one detector together with a lifting

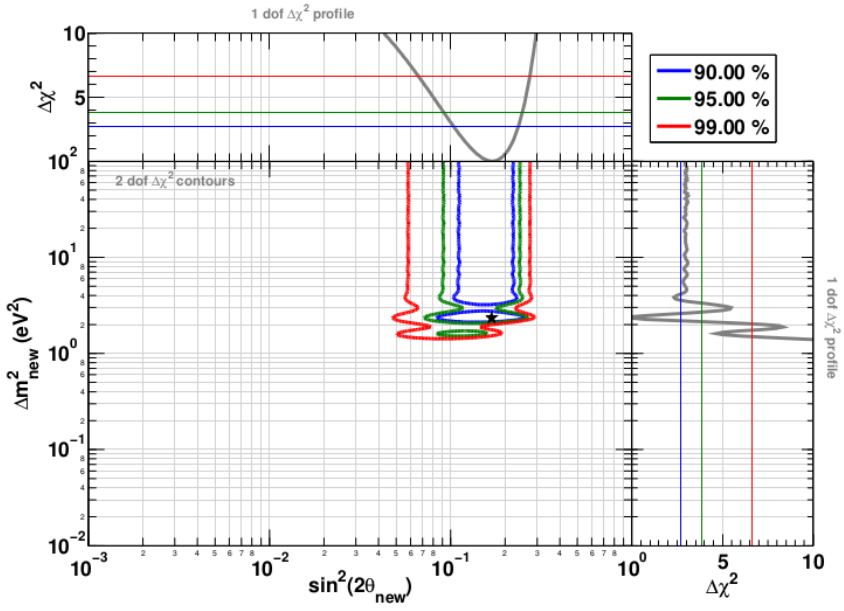

Figure 3.7: The sterile neutrino allowed regions in the $\sin^2(2\theta_{new}) - (\Delta m^2_{new})$ plane from the combination of reactor neutrino experiments, the Gallex and Sage calibration sources experiments (The Gallium anomaly), and the ILL and Bugey-3 energy spectra. The data are well fitted by the 3+1 neutrino hypothesis, while the no-oscillation hypothesis is disfavored at 99.97% C.L (3.6 σ) [2].

device, as it will be done in experiment DANSS, which allows to change the distance and perform measurements at various positions. These methods would enable to measure oscillation pattern at very short baselines.

Predicted sensitivity in the $\sin^2(2\theta_{new}) - (\Delta m^2_{new})$ plane for the detector S^3 was not calculated yet, however, should not be very far from the sensitivity of experiment DANSS, which is shown in Fig. 3.8. It is easily visible, that detector is capable to examine the most probable regions established by other experiments.

3.3.2 Reactor Monitoring

The detector S^3 is very interesting also from the point of view of industrial applications as a monitoring system for nuclear reactors. This idea was discussed in great detail in many papers [32, 33, 34, 35] by many authors.

These authors advise to use antineutrino detector to monitor nuclear reactors power and isotopic composition. The power is directly proportional to number of fissions, which also determine produced $\bar{\nu}_e$ flux as well, thus the number of detected antineutrinos carries information about reactor power.

Moreover, during nuclear fuel cycle, the quantity of each isotope present in the reactor core (^{235}U, ^{238}U, ^{239}Pu and ^{241}Pu) varies considerably (see Fig. 3.9) and since every isotope has a slightly different antineutrino energy spectrum (see Fig. 3.10) we will be able to monitor the isotopic composition of reactor core by measuring overall antineutrino energy spectrum [36]. As a consequence we could prevent illegal production and removal of ^{239}Pu, which is the essential part of nuclear weapons.

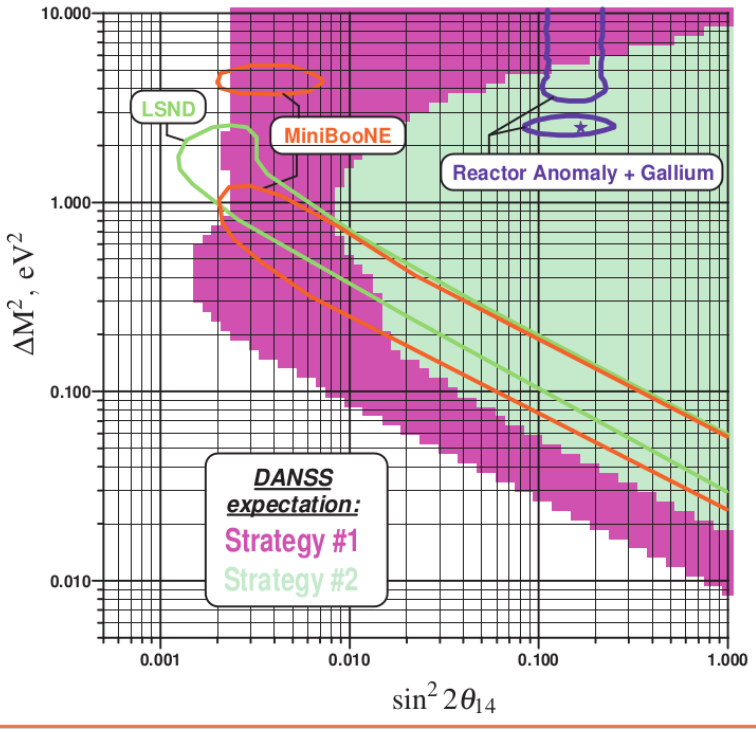

Figure 3.8: DANSS 95% C.L. sensitivity contours for one year of running in case of the shape information only (green) and the most optimistic case of known neutrino energy spectrum (magenta) [31].

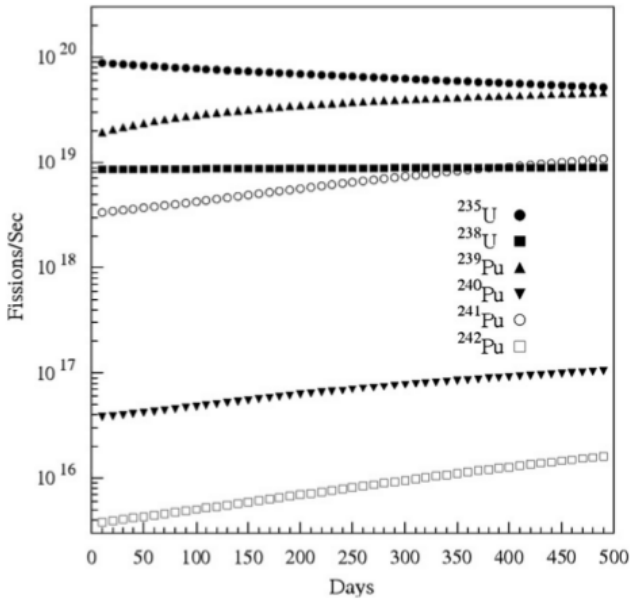

Figure 3.9: Time evolution of the most abundant isotopes in the reactor core [32].

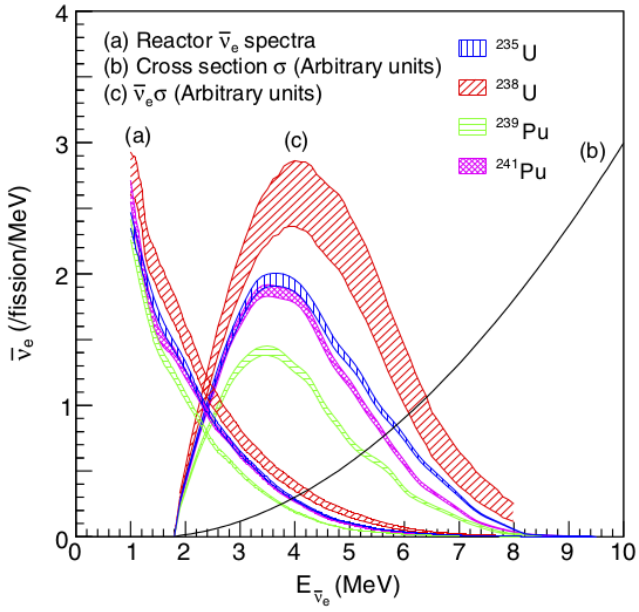

Figure 3.10: (a) Energy spectra of reactor's $\bar{\nu}_e$ for four main fissile isotopes. (b) Cross section of the IBD reaction. (c) Spectrum of observed reactor's $\bar{\nu}_e$ for each fissile isotope obtained as a convolution of (a) and (b) [24].

Nuclear core monitoring by antineutrino flux is another method how to control and safeguard the wide range of reactors. This method is completely independent of cooperation with nuclear power plants staff, can be also done externally (outside of the power plant) and due to inability to shield antineutrino flux, is applicable every time. Such a detector should be used as well for detection of hidden nuclear reactors or nuclear explosions [33].

In the common WWER-1000 reactors the third of the fuel is replaced every 18 months. All the time of the nuclear fuel cycle about 90% of the fissions are from ^{235}U and ^{239}Pu. For this reason it is possible, in the first order approximation, to study only evolution of these two isotopes without significant loss of accuracy. A few GEANT4-based simulations of antineutrino detector response to this evolution was already performed, for instance [32] and [37].

4. Geant4 Simulations

Proper understanding of every newly constructed detector is of vital importance, starting with the structure of inner processes inside the detector and ending with a detection mechanism and a signal pattern which we can expect. Also the knowledge of variation in detector behaviour connected with the change of parameters (number of fibers, dimensions, materials) can help to design even better detectors. Moreover, the simulations, if properly done, could ensure correct interpretations of data obtained under a nuclear reactor in the future. All this and much more can be done with the assistance of Monte Carlo (MC) simulations.

All presented simulations for S^3 detector are written using framework Geant4 [38], which is well-known object oriented simulation toolkit implemented in the C++ programming language and developed at CERN allowing one to perform the simulation of the passage of particles through matter. Geant4 also enables, under certain conditions, to simulate an optical processes as scintillation, WaveLenght Shifting (WLS), reflections and refractions and thus study scintillation detectors in detail.

In our case two stand alone Geant4-based MC simulations were developed:

1. Plate simulation
2. S^3 simulation.

Th first one concerning one scintillation plate including all optical processes which allow us to study light propagation and homogeneity inside the plate and the second one concerning the whole detector S^3 where we can study structure of IBD interaction in our detector (time distributions, paths of particles, etc.), antineutrino detection efficiency, and influence of dead layers as well as the impact of segmentation. Both simulations are described in detail in the following sections.

To verify the accuracy and to gain confidence in results obtained from simulations, the compar, 5.2 and 6.1 thus providing results which can be compared with simulations. Experiments with the whole detector S^3 are much more complicated and yet have to be done after the prototype construction. So the results from S^3 simulations have for the time being just a character of predictions.

4.1 Geant4

Geant4 [39, 40] is one of the most up-to-date and state of the art toolkit for the simulation of the passage of particles through matter. Due to its modularity and flexibility, Geant4 can be used in the various number of situations and enables to study different models and track all desired parameters in the simulations. That is why the Geant4 is used in many areas of research, for instance high energy physics, astrophysics,space science, medical physics and radiation protection.

The main source of information is **User's Guide: For Application Developers** accessible from [38] section guides. This source contains all the most important features which are necessary for application developer. All the simulations developed for detector S^3 were written in the Geant4 version 9.4 patch 04 (released 13 April 2012).

As was mentioned, Geant4 is a package of tools which allows us to use all the necessary components of the simulations [41]:

- the geometry of the system
- the materials involved
- the particles
- the generation of primary events
- the tracking of particles
- the physics processes
- the visualisation of the detector and particle trajectories
- etc.

which are almost always represented by stand alone class category in C++.

Geant4 contains almost all information which we know about particle interactions and incorporates it in easily applicable software. Used physics models are subject to detailed cross-checks with experimental data to confirm their accuracy. Moreover, Geant4 is continuously upgraded and updated with new information. Geant4 is supplemented with a wide range of examples which can be used as a starting point in the development of the new simulations.

In order to preserve versatility, Geant4 is based on the system of classes, which can or can not be initialized in the main function. However, five basic classes are mandatory and have to be initialized in every simulation, they are following : G4RunManager, G4UIanager, G4VUserDetectorConstruction, G4VUserPhysicsList, and G4VUserActionInitialization. The first two classes are so called toolkit class and control the flow of the simulation. The remaining three classes have to be written by user and should contain all necessary information about detector construction, used materials, and sensitive regions (G4VUserDetectorConstruction), particles and physics processes included in the simulation (G4VUserPhysicsList) and a primary particle generator (G4VUserActionInitialization).

Moreover, Geant4 provides also another classes, so called User action classes, which allow us to gain some results from simulations in different stages of simulation. They are G4UserRunAction, G4UserEventAction, G4UserStackingAction, G4UserTrackingAction, and G4UserSteppingAction. In every user action class, a few virtual methods are implemented to simplify interaction with simulation.

The geometry definition is three-phase process in Geant4. First of all, it is necessary to define a solid which contains geometry shape (sphere, box, tube) and dimensions. Then, a logical volume has to be created which holds the pointer to its solid and adds materials, sensitive volumes, or magnetic fields. Finally, a physical volume is defined which takes logical volume and places it on some position. All volumes in the Geant4 are defined in the mother-daughter relationship, it means every single volume has to be placed in some another volume. Only exception is world volume which is also the only mandatory volume.

The main unit of every simulation is an G4Event class. The G4Event contains all information about one experiment, starting with position, type, direction, and energy of the primary particle, continuing with a number and positions of secondary generated particles and ending with their energy losses and trajectories to the time when they are stopped or exit the world volume. It is much more often in the simulations to perform a big number of the experiments. All these events are aggregated into an another class called G4Run.

Propagation of particles through matter is done in the form of vertices. The particle start in the primary vertex and than is transported through defined volumes and according to the cross section of all defined physics processes is stopped and vertex is created. This repeats until the particle has zero energy or exits the world volume. The whole trajectory of one particle is represented by class G4Track. One part of the track between two vertices is represented by G4Step. Information about particles can be retrieved at the end of the track or even at the end of every single step.

4.2 Simulations of the Basic Detection Element

As was mentioned before this simulation package was developed to enable the study of optical processes inside the scintillation plate. Geant4 allows to simulate the optical processes, however, it does not provide any optical properties of used materials which are essential for correct results, thus forcing user to obtain these properties from another sources. The most important properties are the scintillation and absorption spectra of luminescent additives, light yield and its variation, refractive indexes of all used materials, absorption and emission spectra of WLS fibres, quantum efficiency of PMT cathode an much more. In addition, to make these simulations more realistic, it is necessary to know and use wavelength-dependent values of these properties.

The main results of this simulation package should be a number of detected p.e., resolution and also homogeneity of our scintillation plate. These results can and should be compared with experimentally obtained data to evaluate accuracy of the simulations. The simulation package, if found to be sufficiently precise, can also be used to predict behaviour of the plates under certain circumstances without necessity to perform real experiments.

The geometry of the scintillator plate was set according to the real dimensions and materials of plates used in the experiment S^3. The polystyrene scintillator plate with dimensions 40 x 20 x 1 cm^3 from scintillation material defined as 47.5 % of carbon and 52.5 % of hydrogen and density 1.03 g/cm^3 was wrapped by 800 μm of teflon (see Fig. 4.1).

WLS fibres with the length of 40 cm and the diameter of 1 mm were placed into the plate. The WLS fibres consist of three layers [42] : core (polystyrene, $\rho = 1.05\,g/cm^3$), inner cladding (PMMA, $\rho = 1.19\,g/cm^3$), and outer cladding (Fluorinated polymer, $\rho = 1.43\,g/cm^3$), while cladding thickness is 3 % of diameter for both inner cladding and outer cladding. Trapping efficiency of produced light is cited to be 5.4 %.

The geometry of fibres outside the detector and PMT was considerably simplified in our simulations. Instead of relatively complicated bending of fibres and their connection to the PMT, the small version of PMT was defined at the end of

every fibre which are fully nested in the volume of scintillator. However, this simplification has no effect on the functionality or results at all since the bending loss is significant for diameters smaller than 5 cm. The Hamamatsu PMT R7600U-300 was represented by entrance borosilicate window and aluminium photo cathode.

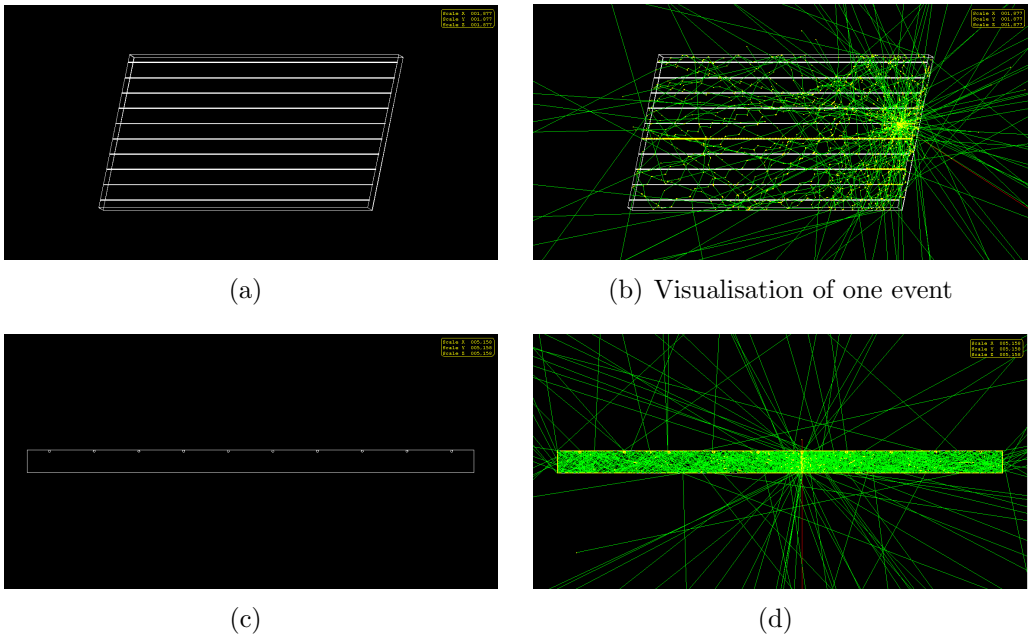

(a) (b) Visualisation of one event

(c) (d)

Figure 4.1: Different views of the visualisations of detector geometry and one event when primary particle (1 GeV muon) passes through the plate and create scintillation photons. Light yield of the scintillator is 100 times reduced for purpose of visualisation. a) Visualisation of plate geometry. b) Visualisation of one event. c) Visualisation of plate geometry (side view). d) Visualisation of one event (side view).

In the simulations, electrons and muons were used as a primary particles. First, the muons with energies $E = 2.5\,\mathrm{GeV}$ (with minimum ionization) were used, but because such a muon has fixed value of deposited energy per cm of scintillator which is quite high ($\geq 2\,\mathrm{MeV/cm}$) and thus thousands and thousands of optical photons are created and subsequently tracked in the single simulation it is not optimum method for testing due to long simulation times.

It is completely different with electrons. The desired deposited energy can be achieved easily by changing initial energy of electron. Even for electrons with energy 2 MeV is electron completely trapped in the volume of the scintillator and release almost all its energy in the volume. However even with electrons, 1000 events, which are necessary for sufficient statistics, are simulated longer then 12 hours.

As was mentioned, the primary particles are usually monoenergetic, nevertheless it is possible to set any desired energetic distribution. It also applies for primary vertex and direction of primary particles. If there is no special reason, particles are created about 1 cm over the plate (z axis) and are fired perpendicular to the plate (located in the x-y). In our simulations, various position distributions in the x-y plane were used. The simplest one is point-like source, although also

homogeneous distribution over different parts of the plate were used to mimic area covered by pair of the triggering scintillators used in measurements performed at JINR described in Sections 5.1 and 5.2.

All necessary particles and physics processes were defined. The most important particles are used primary particles (electron and muon) and also gamma and optical photon which is in the Geant4 implemented separately. For the purpose of simulations, all electromagnetic and optical processes for defined particles were set. For gamma they are photo effect, Compton scattering and pair production. For e^+/e^- they are multiple scattering, ionisation, Bremsstrahlung, and annihilation. For μ^+/μ^- is the set identical with processes activated for electron and positron except the last mentioned plus e^+e^- pair production. Moreover all possible optical processes : Cherenkov radiation, scintillation, optical absorption, and boundary processes were activated.

The most important parts of this simulation package are input optical parameters which reflect the level of conformity with reality. In this section, a brief review of all used properties and their wave-dependent behaviour are presented.

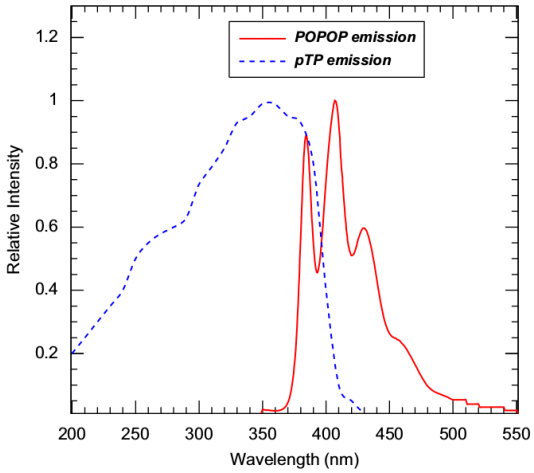

Figure 4.2: Emission spectra of pTP as a POPOP [43].

First of all, the world volume is filled with air whose refractive index is set to be one in the whole range of studied wavelengths.

The optical properties of the scintillator are much more complicated. To simulate behaviour of the three component scintillator : polystyrene (PS) matrix - first luminescent additive (pTP) - second luminescent additive (POPOP) we used approached described in the [43] where plastic scintillator properties were studied for the experiment SuperNEMO. Due to incapability of the GEANT4 to assign two different WLS processes to the one volume, we had to threat two first components (PS and pTP) as a single entity and only POPOP molecules could produce WLS. So the light produced according to the emission spectrum of pTP (Fig. 4.2) propagate through the volume and can be absorbed and stopped by mixture of PS and pTP or can interact with molecules of POPOP and be shifted to longer wavelengths. The probabilities of these two processes are dependent on the absorption spectra of PS/pTP mixture and WLS absorption spectra of POPOP (Fig. 4.3). Provided that the photon is absorbed by POPOP the is a chance that it will be consequently emitted with wavelength according to the

WLS emission spectrum of POPOP (Fig. 4.2).

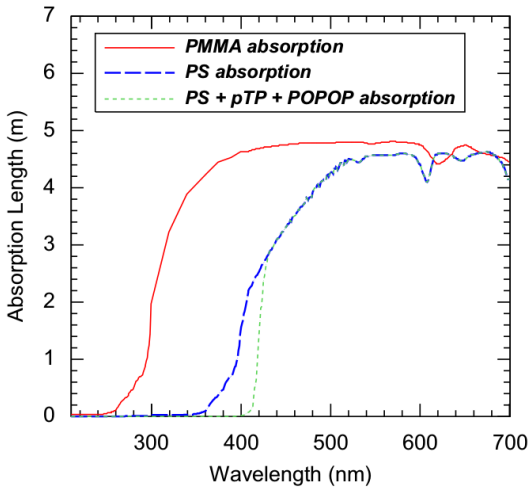

Figure 4.3: Absorption spectra of the PS alone and in the mixture of PS, pTP, and POPOP [43]. In our simulations the shape of the spectra were preserved, however the maximal absorption length were normalized to 3.2 m which is the value provided by producer.

From both emission spectrum and absorption spectrum is possible to get a basic understanding of the scintillator. The energy deposited in the scintillator on the polystyrene matrix which has no ability to produce light is transformed to excitations of pTP molecules which during the transition to the ground state can produce light according to the pTP emission spectrum shown in Fig. 4.2. The produced photons (mainly in the range 200-400 nm) then propagate through the volume of the scintillator and are either absorbed or shifted. Absorption spectra show that absorption length for absorption without re-emission (PS) in the range 350-400 nm is quite long in contrast with the absorption length for WLS (PS+pTP+POPOP), thus providing much higher probability to re-emit absorbed light according to the emission spectrum for POPOP (370-550 nm). Part of the light produced by POPOP (370-400 nm) is subjected to unceasing self-absorption since the light can travel through the PS/pTP/POPOP mixture almost freely up from 400 nm where absorption length for both light absorption and WLS are long enough.

The wave-dependent refractive index of the scintillator was also taken from [43] and is shown in Fig. 4.4. The light yield was set to be 11520 photons per 1 MeV of deposited energy. This number was calculated on the basis of documents provided by producer where relative light output compared with light output of NaI(Tl) (40 photons/keV) was given. Another optical non wavelength-dependent properties of the scintillator, like slow and fast time scintillation constants, spread in the number of produced photons and time constant of WLS, were set to correspond with basic type of scintillators (e.g. Saint Gobain's BC-420).

Information about optical properties of WLS fibres was taken from [44] and [45], the most importantly the absorption spectra without re-emission and with WLS (see Fig. 4.5) and emission spectrum for WLS additive labeled k27 (Fig. 4.6). The absorption spectrum of WLS fibre shows that the greatest absorption is up to 500 nm which is exactly the light produced by POPOP (350-550 nm),

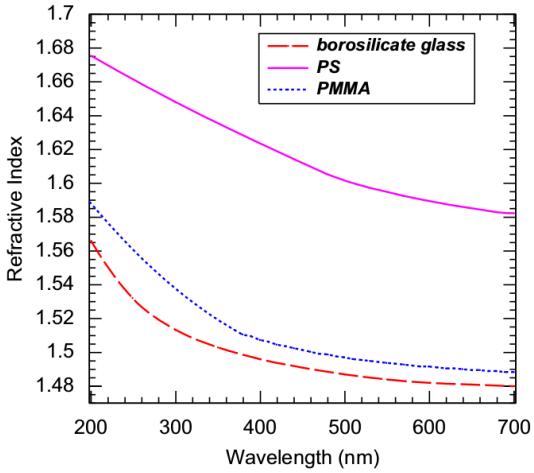

Figure 4.4: The refractive index of the scintillator and borosilicate glass [43].

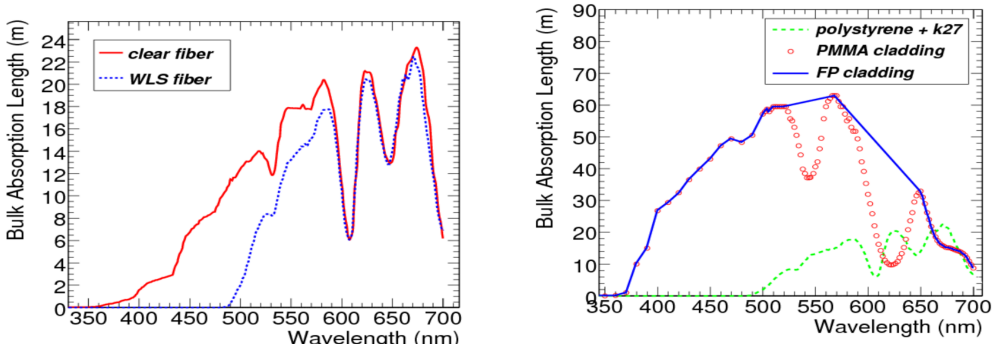

(a) (b)

Figure 4.5: The absorption spectra of clear fibre and WLS fibre (a) and also absorption spectra of both cladding layers (b) [44].

thus ensuring excellent capture of light from the scintillator in the fibres. The refractive indexes of all three layers inside the fibre were set to be constant and equal 1.6, 1.49, and 1.42 from the core to most outer layers. The absorption spectra of the cladding layers were set to be constant and equal 10 metres on the basis of Fig. 4.5 where one can see that this is fulfilled in the whole range of studied wavelengths.

The PMT is consisting of two parts in the simulations : borosilicate glass and aluminium photocathode. There are only two worth mentioning optical properties of borosilicate glass, absorption length and refractive index, and both were set to be constant. Refractive index is 1.49 and absorption length is 4.2 m. For the photocathode only spectral quantum efficiency was used (Fig. 4.7).

The optical properties of teflon reflective layer used in the simulations are constant refractive index 1.315 and spectral reflective coefficient shown in Fig. 4.8. Moreover, the teflon tape is modelled as a surface with only diffuse reflection.

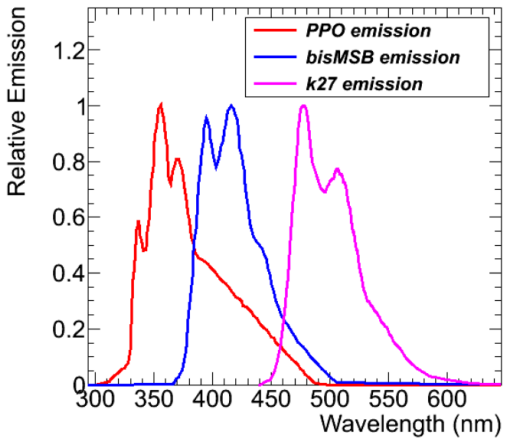

Figure 4.6: The emission spectrum of the luminescent additive k27 added to the core of Kuraray WLS fibres [44].

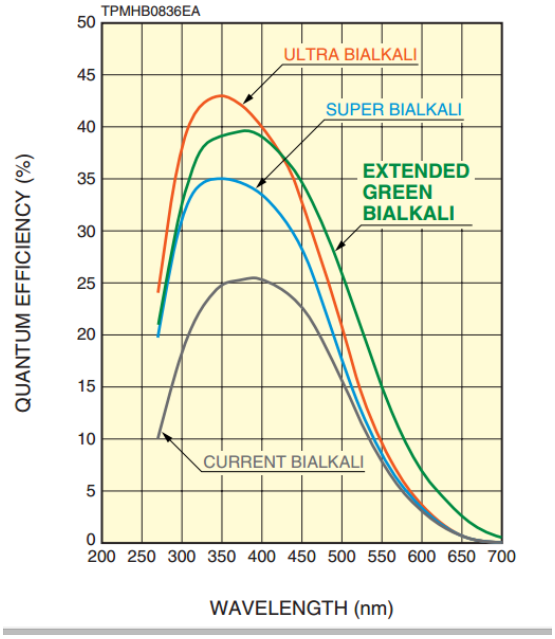

Figure 4.7: Quantum efficiency of the R7600U-300 PMT with extended green bialkali photocathode from the company Hamamatsu [46].

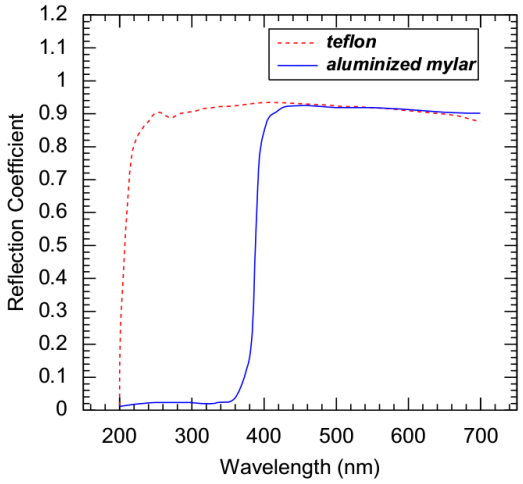

Figure 4.8: Reflection coefficient for the teflon tape [43].

4.2.1 Results

As was mentioned before, the main result of these simulations is the number of photoelectrons (p.e.) detected in one event. This number is obtained in the end of every event when all produced p.e. are counted and this value is saved in the histogram.

Figure 4.9 illustrates results of the single scintillation plate simulation as a histogram of number of photoelectrons for different tested positions. In the simulations 1000 electrons with energy 1 MeV are generated 1 cm above the plate uniformly distributed and directed perpendicularly to the plate. Figures 4.9(a) and 4.9(b) show results for positions a) and b) depicted in Fig. 4.9(d). These results allow us to calculate the homogeneity of light collection and compare this number with experimentally obtained data. Areas a) and b) match the area bounded by the size and shape of triggering scintillators described in Section 5.1 to be easier compared with the experiment. Area c) includes the whole plate and is used to determine total yield of the plate.

The number of detected photoelectrons (p.e.) normalized to 1 MeV of deposited energy obtained from simulations is equal $\mathrm{n}_{\mathrm{p.e.}}^{sim} = (30.7 \pm 0.2)$. Even though in every simulation more than 10 000 photons are created, the results from simulations are consistent with the results obtained in experiments.. The numbers of detected p.e. for areas a) and b) are $\mathrm{n}_{\mathrm{p.e.}}^{sim} = (34.2 \pm 0.2)$ and $\mathrm{n}_{\mathrm{p.e.}}^{sim} = (27.4 \pm 0.2)$ thus give homogeneity $H = 80,1\%$.

From the results shown in Fig. 4.9 is also possible to calculate expected energy resolution of the plates which is given by the relation

$$R = \frac{\Delta E}{E} = \frac{FWHM_E}{E} = \frac{2.35 \cdot \sigma_E}{E} \ . \tag{4.1}$$

Both values σ_E and E can be obtained from the aforementioned results in the form of the number of detected p.e. thus giving resolution $R = 47.8\,\%$ in the case of the whole plate.

If we assume that the number of detected p.e. is distributed according to the Poisson distribution the σ_E is equal to the $\sqrt{k_{p.e.}}$ where $k_{p.e.}$ is the very number of detected p.e. Therefore, for the whole plate the σ_E should be $\sigma_E = 5.5$ p.e. in

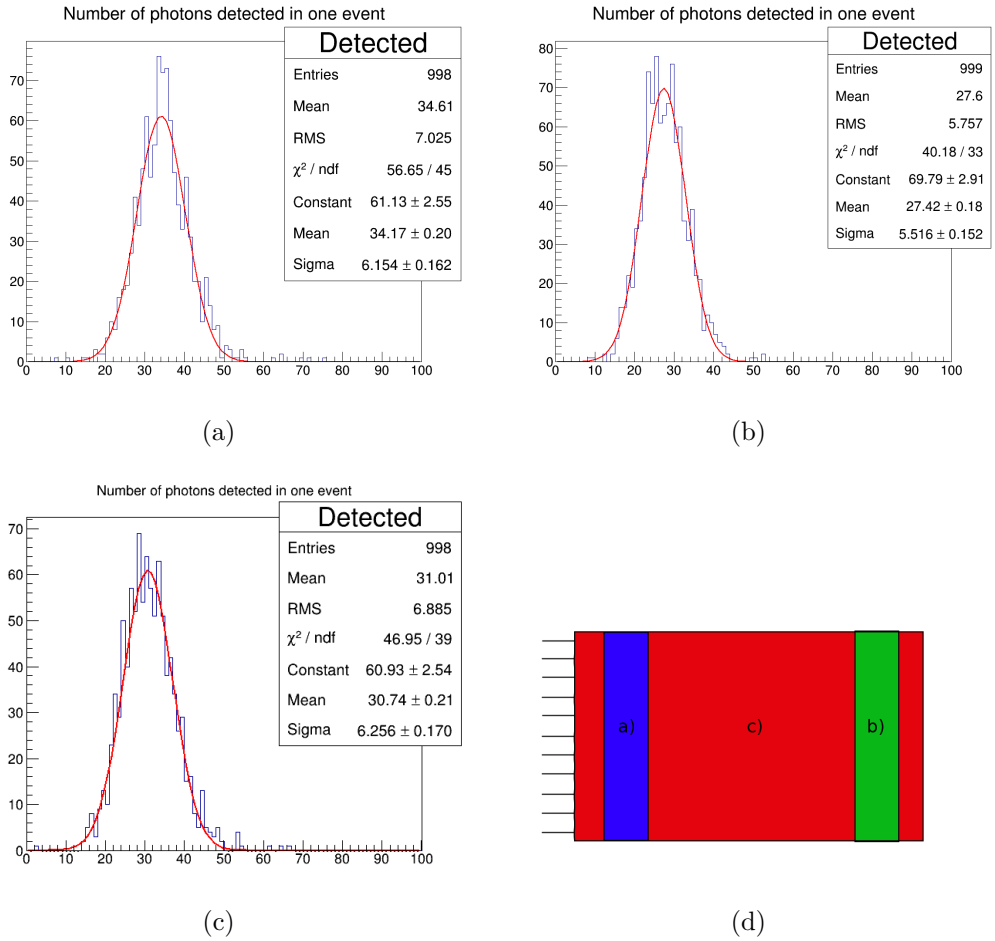

Figure 4.9: Results of the simulations of scintillation plate with different position distributions of primary particles. As primary particles were used 1 MeV e^- homogeneously distributed 1 cm over the plate and targeted perpendicularly to the plate. Figures a), b), and c) illustrate results for different tested areas which are shown in Fig. d).

comparison with the $\sigma_E^{sim} = (6.3 \pm 0.2)$ p.e. obtained from the simulations.

On the other hand, if we use point-like source of electrons the result $\sigma_E^{sim} = (5.9 \pm 0.2)$ p.e. (Fig. 4.10) is in great agreement with the sigma obtained if the distribution would be Poisson $\sigma_E = \sqrt{k_{p.e.}} = \sqrt{34,4} = 5.9$ p.e..

This simulation package can be also used to predict behaviour of the scintillation plate under different circumstances. For instance, strength of the signal from six positions (Fig. 4.11) on the plate was studied when

1. light collection is done through WLS fibres attached to the PMT

2. light is collected directly by the PMT attached to the one side of plate.

As a primary particle were used 1 MeV electrons produced in the point-like source 1 cm above the plate and heading perpendicularly.

Results of the simulations for option with fibres and option only with PMT are shown in Tables 4.1 and 4.2, respectively. Signal in the number of detected

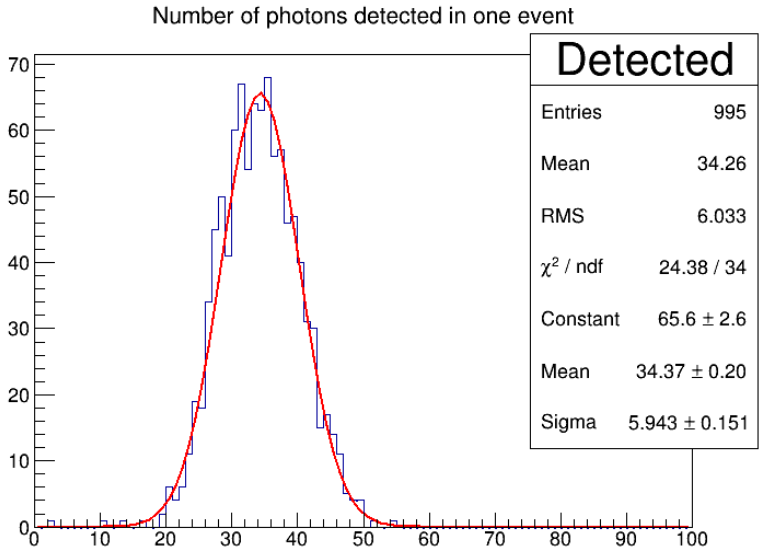

Figure 4.10: Results of the simulations of scintillation plate with point-like source of primary particles.

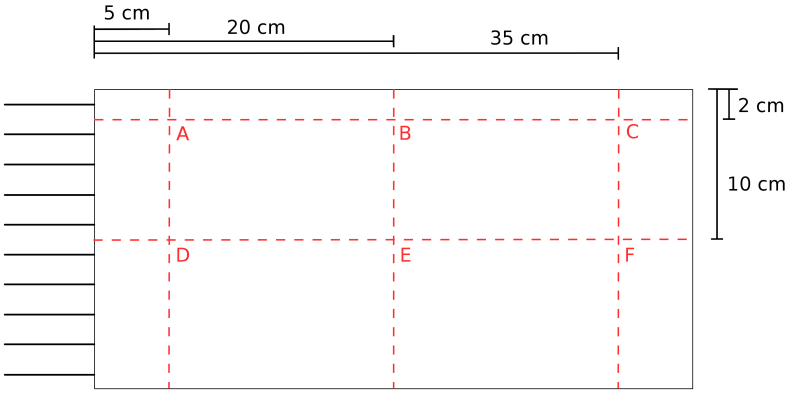

Figure 4.11: Tested positions labelled by letters A-F together with dimensions.

Position	Signal [$n_{p.e.}$]	Sigma [$n_{p.e.}$]	Signal/$Signal_D$	Signal/S [$n_{p.e.}/mm^2$]
A	33.21 ± 0.25	5.34	0.95 ± 0.01	3.32 ± 0.03
B	29.04 ± 0.26	5.45	0.83 ± 0.01	2.90 ± 0.03
C	26.20 ± 0.25	5.00	0.75 ± 0.01	2.62 ± 0.03
D	34.78 ± 0.28	5.98	1.00 ± 0.01	3.48 ± 0.03
E	30.31 ± 0.26	5.44	0.87 ± 0.01	3.03 ± 0.03
F	26.95 ± 0.26	5.48	0.77 ± 0.01	2.70 ± 0.03

Table 4.1: Signal strength from various positions on the plate for option 1 (WLS fibres). $Signal_D$ means the signal from the position D. Signal/S refers to the signal normalized to the $1\,mm^2$ of the photosensitive area.

Position	Signal [$n_{p.e.}$]	Sigma [$n_{p.e.}$]	Signal/$Signal_D$	Signal/S [$n_{p.e.}/mm^2$]
A	78.90 ± 0.51	9.98	0.41 ± 0.00	0.44 ± 0.00
B	93.23 ± 0.47	9.72	0.49 ± 0.00	0.52 ± 0.00
C	84.09 ± 0.52	10.45	0.44 ± 0.00	0.47 ± 0.00
D	190.6 ± 0.9	16.50	1.00 ± 0.01	1.06 ± 0.00
E	95.51 ± 0.53	10.16	0.50 ± 0.00	0.53 ± 0.00
F	87.39 ± 0.49	9.80	0.46 ± 0.00	0.49 ± 0.00

Table 4.2: Signal strength from various positions on the plate for option 2 (PMT directly). $Signal_D$ means the signal from the position D. Signal/S refers to the signal normalized to the $1\,mm^2$ of the photosensitive area.

photoelectrons, sigma of fitted Gaussian and ratio of signal strength to the signal from position D are shown. Also signal strength of the signal normalized to the $1\,mm^2$ of the sensitive area of PMT is calculated for every particular simulation. For the option 1 the used sensitive area of the PMT is $10\,mm^2$ (10 fibres). For the option 2 the area is $180\,mm^2$ (18 mm - dimension of the PMT sensitive area x 10 mm - dimension of the plate).

Results show that option 2 provides up to six times higher signal strength depending on the position. It seems like a better results, however there is much more drawbacks of this option. Transverse and longitudinal homogeneity is more than twice worse, obtained sigma demonstrate that signal is not distributed according to the Poisson distribution anymore ($\sigma \neq \sqrt{\text{Signal}}$) and moreover signal strength normalized to the unit area ($1\,mm^2$) of the PMT sensitive area proves that option 1 is much more effective in the sense "Price/Signal Strength".

One of the last studied properties of the scintillation plate was time distribution of detected photoelectrons and subsequent signal reconstruction. During the simulation times of the photoelectrons detection can be easily saved in the txt files and then processed by the ROOT script. The saved times are measured according to the time of emission of the primary particle. Four such a time distributions are shown in Figure 4.12 in red.

To reconstruct the signal, which is normally obtained from the PMT, from time distribution of detected photoelectrons a few simplifications had to be applied. We based the reconstruction procedure on the real experiments which are

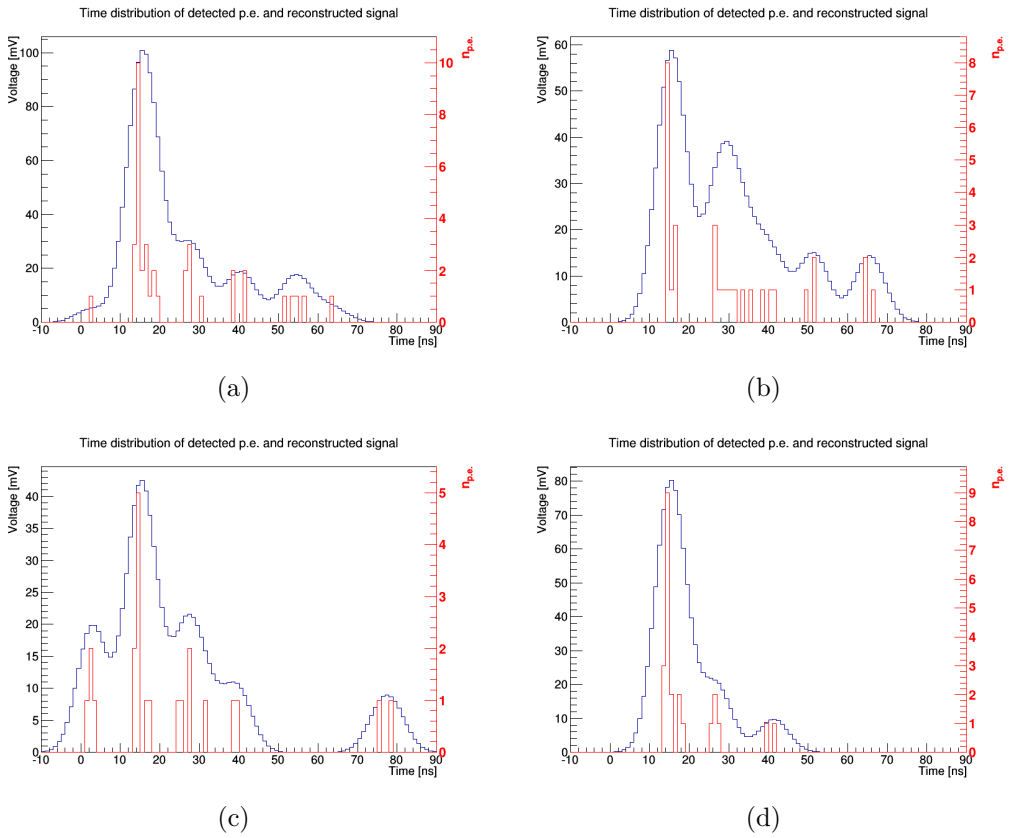

Figure 4.12: Four examples of the time distributions of detected photoelectrons obtained from simulations (in red) and signals (in black) reconstructed from these distributions via method described in the text. These signals are in the experiment measured as the output of the PMT and thus can be efficiently compared.

described in the detail in Section 6. We were measuring individual plates using electron source developed by IEAP CTU, which provides flux of mono-energetic electrons. Results of one such a measurement are shown in Fig. 4.13. Integral of the signal from the scintillation plate is shown in yellow and is measured in the units of nVs. If we find out the number of produced photoelectrons and if we assume that every single photoelectron causes approximately the same signal we can calculate number of nVs produced by one photoelectron. Another assumption is that the time course of the signal produced by the PMT after detection of a photoelectron can be described by the Gaussian function

$$S(t) = A \cdot \mathrm{e}^{-\frac{(t-t_0)^2}{2\,\sigma^2}} \ , \tag{4.2}$$

where A and σ are unknown and t_0 are obtained from the simulation. If we integrate this function over time we obtain $S_{int} = A \cdot \sigma \cdot \sqrt{2\,\pi}$. This value should be equal to the number of nVs produced by one photoelectron mentioned above which is obtained from experiment. If we get one of the unknown parameters A and σ the second one can be calculated. The final reconstructed signal is obtained by superposition of Gaussian signals from the individual photoelectrons. The reconstructed signals are shown in Fig. 4.12 together with initial time dis-

tribution of photoelectrons. These results are dependent on the determination of the value of unknown parameters A or σ. The reconstructed signals can be processed and their amplitudes and integrals can be histogramed and compared with experimental results.

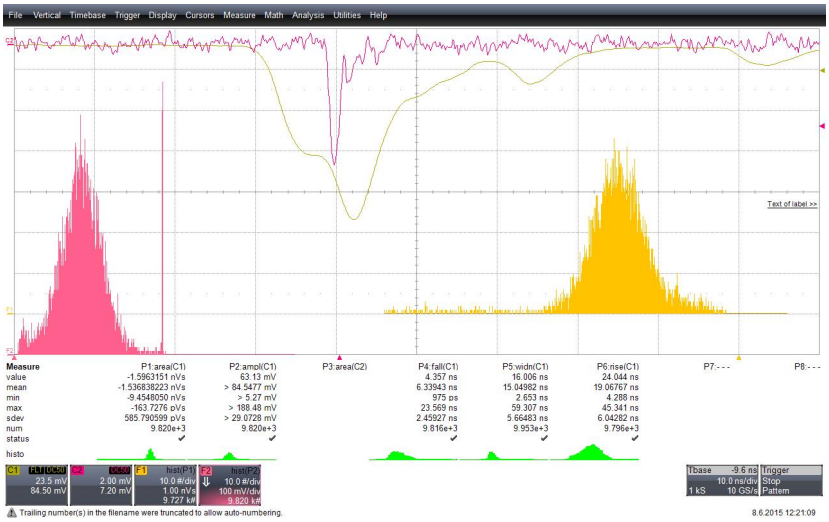

Figure 4.13: Results of the testing of one scintillation plate using mono-energetic electron source. Signals from the plate (in yellow) and triggering device (in pink) as well as histograms of amplitude (in pink) and integral (in yellow) of signals from the plate are shown.

4.3 S^3 Detector Simulations

The second simulation package enables to simulate and study response of the whole detector to the detected antineutrino. Simulations of the whole detector should give us basic image of detector behaviour and provide us better understanding of inner processes and easier interpretation of obtained data. Furthermore we can obtain the idea of characteristics behaviour (e.g. efficiency) depending on the changing parameters like dimensions, thickness of gadolinium layer, segmentation etc. We can also study spacial and time structure of IBD, like path length of produced particles, time between positron annihilation and neutron capture, efficiency of neutron capture etc.

Simulation geometry is based on the real construction described in Section 3.1 and used materials are described in Section 4.2. If it is not specifically mentioned, 80 plates with dimension 40 x 20 x 1 cm^3 are used in all simulations. However, the number of plates in all directions and their dimensions can be changed easily as well as the thickness of gadolinium layer in the startup macro shown in the Appendix A. In addition, refractive and gadolinium layers are simulated to study the influence of dead layers to the deposited energy.

Due to limited computing power and time these simulations are for the time being used without activated optical processes and WLS fibres. It means that no optical photons are created and propagated through the detector. The results of these simulations provide only information about deposited energy and do not contain its conversion to the light. Visualisation of one antineutrino detection

together with the detector is shown in Fig. 4.14. Plates where more energy than E_{thr} was deposited are displayed in red (in this case $E_{thr} = 10\,\mathrm{keV}$).

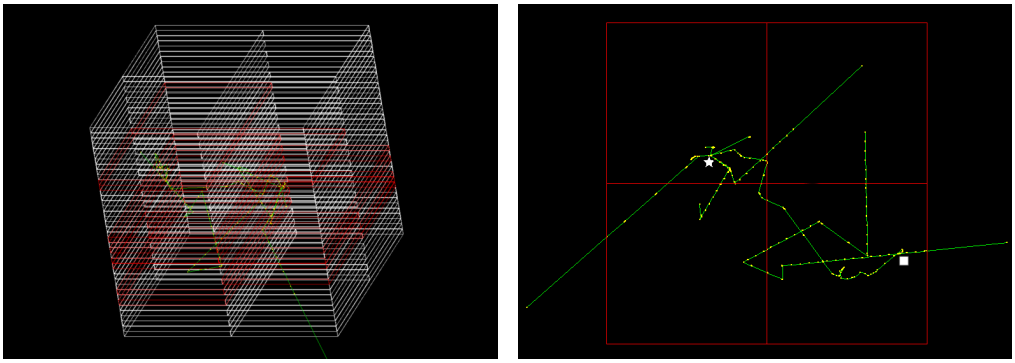

(a) (b)

Figure 4.14: Simulation of the detector S^3. a) View of the detector with produced particles while plates with deposited energy higher than $E_{thr} = 10\,\mathrm{keV}$ are displayed in red. b) Visualisation of simulation in the top view. Square indicates position of positron annihilation and two 511 keV gamma creation. Asterisk shows position of neutron capture.

Interactions of the antineutrinos are not implemented in the Geant4 at all (at least up to version 10.1). It means that IBD interaction have to be mimicked as best as possible artificially. From the articles about IBD structure [23],[47] the IBD cross section with respect to the energy of incoming antineutrino, energy and angular distribution for produced neutron and positron and ratio of antineutrino energy carried away by positron and neutron can be obtained. [23] shows that at zeroth order in $1/M$ whole energy of the incoming antineutrino is transferred to the positron according to the equation

$$E_e^{(0)} = E_\nu - \Delta \tag{4.3}$$

where $E_e^{(0)}$ is the energy of positron at zeroth order, E_ν is the energy of antineutrino and $\Delta = M_n - M_p$, while M_n and M_p are masses of neutron and proton, respectively. Energy distribution of the neutrons is shown in Fig. 4.15(a). Cross section of the IBD at zeroth order in $1/M$ is

$$\sigma_{tot}^{(0)} = 0.0952 \left(\frac{E_e^{(0)} p_e^{(0)}}{1\,\mathrm{MeV}^2} \right) \times 10^{-42}\,\mathrm{cm}^2 \,, \tag{4.4}$$

where $p_e^{(0)}$ is positron momentum. Angular distributions of both product are shown in Fig. 4.15(b). In this figure you can see that positron is distributed almost isotropically. On the other hand neutron, as a carrier of momentum, is strongly forward peaked.

IBD is in the simulation package mimicked as follows. Firstly, random position in the volume of the detector is generated. Secondly, primary particles, positron and neutron, are generated in this point. Secondly, antineutrino energy is generated (described below in detail), positron energy is calculated according

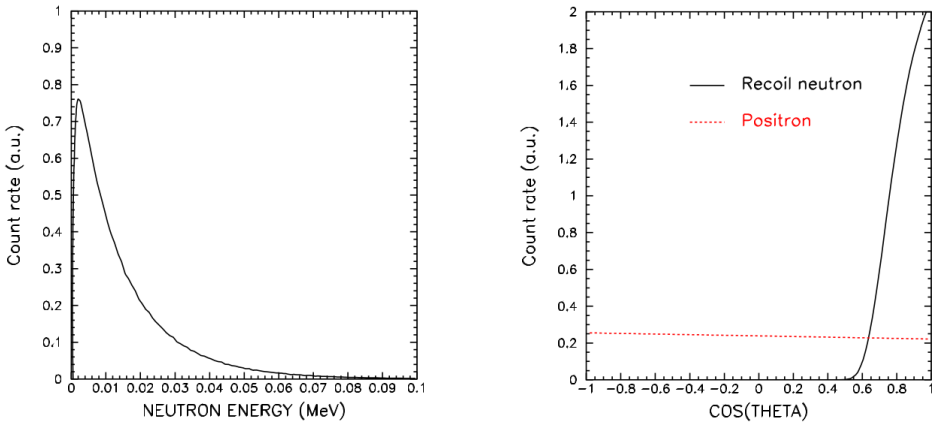

(a) (b)

Figure 4.15: Energy and angular distributions of products of IBD [47]. a) Energy distribution of neutron. b) Angular distribution of neutron and positron.

to Eq. 4.3 and neutron energy is generated on the basis of Fig. 4.15(a). Finally, the direction of positron momentum is generated isotropically and the direction of neutron momentum is set to be down-going (we are under reactor and antineutrinos are also down-going, from the top of the detector to the bottom, in other words in the -z direction). Also another position, direction and energy distribution for both primary particles can be easily set by startup macro (see App. A).

The energy spectrum of primary antineutrinos is very variable and can be set in different ways. The energy of antineutrinos can be defined as fixed or distributed according to the real energy spectrum of individual isotopes created in a nuclear core. Also energy spectrum obtained as the combination of few isotopes with different abundance can be set to study changes in the number of detected events and in the shape of positron energy spectra.

The real energy spectra of antineutrinos produced by different isotopes are intensively studied due to neutrino oscillations. In 2011, the reanalysis of these spectra which used improved conversion of an electron energy spectrum into an antineutrino energy spectrum [26] gave new estimates. The spectra of different isotopes can be parametrised, with high precision, as the exponential of a polynomial [26]

$$S_k(E_\nu) = \exp\left(\sum_{p=1}^{6} \alpha_{pk}\, E_\nu^{p-1}\right) \ , \tag{4.5}$$

where $S_k(E_\nu)$ is antineutrino spectrum for isotope k, α_{pk} are coefficients obtained by fit and E_ν is the energy of antineutrino. The values of coefficients α_{pk} used in our simulations are taken from [26] and shown in Table 4.3 for uranium isotopes and in Table 4.4 for plutonium isotopes. The spectra (dashed lines) are also shown in Fig. 4.16 together with the cross section of IBD (black line) according to the Eq. 4.4 and supposed detected spectra of antineutrinos for various isotopes obtained by folding IBD cross section and emitted spectra (solid lines).

	$k = {}^{235}\mathrm{U}$		$k = {}^{238}\mathrm{U}$	
p	α_{pk}	$\delta_{\alpha_{pk}}$	α_{pk}	$\delta_{\alpha_{pk}}$
1	3.217	4.09(-2)	4.833(-1)	1.24(-1)
2	-3.111	2.34(-2)	1.927(-1)	5.86(-2)
3	1.395	4.88(-3)	-1.283(-1)	1.11(-2)
4	-3.690(-1)	6.08(-4)	-6.762(-3)	1.92(-3)
5	4.445(-2)	7.77(-5)	2.233(-3)	2.84(-4)
6	-2.053(-3)	6.79(-6)	-1.536(-4)	2.86(-5)

Table 4.3: The values of coefficients α_{pk} from Equation 4.5 for isotopes $k = {}^{235}\mathrm{U}$, ${}^{238}\mathrm{U}$ [26].

	$k = {}^{239}\mathrm{PU}$		$k = {}^{241}\mathrm{Pu}$	
p	α_{pk}	$\delta_{\alpha_{pk}}$	α_{pk}	$\delta_{\alpha_{pk}}$
1	6.413	4.57(-2)	3.251	4.37(-2)
2	-7.432	2.85(-2)	-3.204	2.60(-2)
3	3.535	6.44(-3)	1.428	5.66(-3)
4	-8.820(-1)	9.11(-4)	-3.675(-1)	7.49(-4)
5	1.025(-1)	1.38(-4)	4.254(-2)	1.02(-4)
6	-4.550(-3)	1.29(-5)	-1.896(-3)	9.03(-6)

Table 4.4: The values of coefficients α_{pk} from Equation 4.5 for isotopes $k = {}^{239}\mathrm{Pu}$ and ${}^{241}\mathrm{Pu}$ [26].

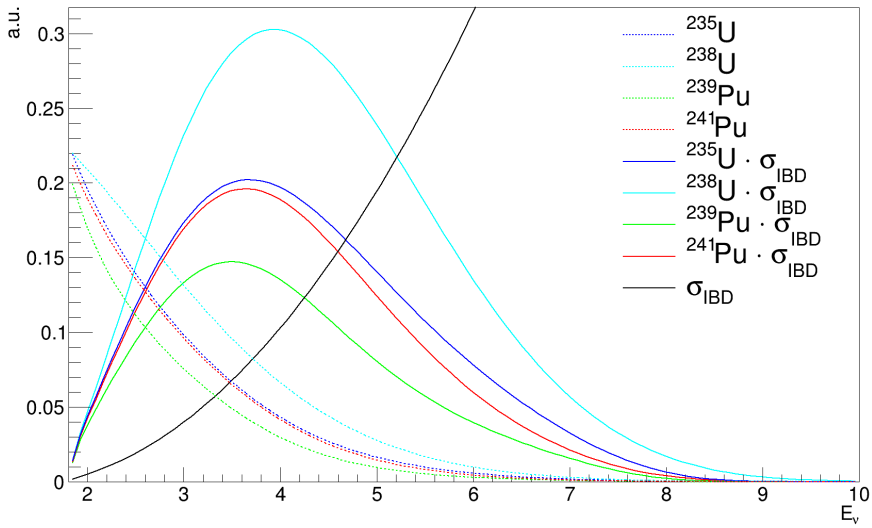

Figure 4.16: IBD cross section, emitted antineutrino spectra for different isotopes (dashed lines) and detected antineutrinos spectra (solid lines) which are constructed by folding IBD cross section and emitted spectra.

All parts of the detector are set as a sensitive volumes. It means if some interaction occurs in this volume, special class is called and all relevant information are saved about this interaction point. There are two types of sensitive volumes in our simulations, one representing real sensitive (active) volumes where energy can be measured (scintillators) and second one representing the rest of volumes (gadolinium layer, refractive layer, world volume). The list of information about every interaction point is following:

- Run, Event, Track, Particle and Step identification number
- Particle encoding
- Numbers representing in which scintillator the interaction happened
- Name of the particle
- Name of the creation process of the particle
- Name of the process in this interaction
- Vertex position
- Position of interaction
- Global time
- Track length
- Vertex kinetic energy
- Kinetic energy
- Step length
- Total deposited energy
- If the interaction was in the active volume
- If the particle leave the world volume.

For purpose of the reasonable handling with data, specialized class (AnalysisManager.cc) was written. In the beginning, root file is created and TTree with branches representing all above mentioned information about interaction points is allocated. When any interaction happen the sensitive volume class is called, all the information is forwarded to the analysis manager which calculate a few quantities (multiplicity of hits for positron and neutron, number of interaction etc.) and save them together with the rest of information to the TTree. Detailed processing of this information is done in the external program which we developed especially for this task.

4.3.1 Results

A few basic quantities for positrons and neutrons can be evaluated directly using results of MC simulation package. These quantities from simulation of 10 000 antineutrino events are shown in Fig. 4.17. The left column shows results for positrons and the right column shows results for neutrons. The first two pictures show deposited energy for positrons and neutrons in active layers, in passive layers and in total. The second two pictures show number of interaction which positron or neutron had undergone before he stopped of left the world volume. Third row of pictures shows multiplicity of hits or in other words number of scintillator plates where tracked positron or neutron undergone some interaction. And the last pair of pictures shows two distances. The first one is track length when the length of individual steps is summed and the result is the distance which particle really passed in the detector. The second one is called distance from vertex and is calculated as a difference of final position and initial position where the tracked particle was created.

Much more information can be obtained when the results from simulation are processed by another program called Analyser which was written specifically for this task. This program takes root TTree as an input data and use the information from interaction point to reconstruct tracks of all important particles and get another information as a number of produced gamma after neutron capture, their energies, time between positron annihilation and neutron capture etc.

Several studied quantities are shown in the following figures. In Figure 4.18 is shown if the initial neutron from IBD was captured or escaped without interaction. The x axis represents this information in the binary format, it means number one represents successful neutron capture while zero represents escaping neutron. The results show that 46.0 % of simulated neutrons are captured in our detector.

Neutron can be also captured on hydrogen atom producing gammas with significantly smaller total energy of produced gammas (2.2 MeV). The probability of capture on Gd is shown in Figure 4.19. The x axis represents this information again in the binary format. If neutron is captured on Gd the bin 1 is incremented. If the neutron is captured on hydrogen or not captured at all the bin 0 is incremented. The results show that 41.1 % of neutrons is captured on Gd while only 4.9 % of them is captured on hydrogen. In combination with results from previous paragraph we can calculate that 10.6 % of all captured neutrons is captured on hydrogen. This information is important for determination of energy threshold for delayed signal.

Another interesting quantity crucial for proper understanding of our detector, specially for structure of the delayed signal, is number of gammas created after neutron capture. This quantity is illustrated in Fig. 4.20. The results show that the most probable number of created gammas is 3 however more than 10 gammas can be also created. The total energy of all produced gammas is shown in Fig. 4.21. In this Figure the number of neutrons captured on hydrogen can be obtained too from the intensity of 2.2 MeV line. However, not all energy of gammas created from the neutron capture is deposited in the detector. Figure 4.22 provides an estimate of how much energy from gammas is deposited in the detector itself. This information is important for us to know how strong the delayed signal will be.

And the last studied properties of neutron is its initial energy (see Fig. 4.23) which is monitored purely in order to control the correctness of simulated data. This histogram is consistent with Fig. 4.15(a).

Positrons were studied in many different ways as well. For instance, a few basic examined properties are shown in the following figures. In Fig. 4.24 is shown the probability of positron annihilation in our detector. Due to short positron track length this probability is 96.66 % which is much more higher in comparison with probability of delayed signal.

Figure 4.25 shows the energy spectrum of gammas produced in annihilation of positron. The result exhibits behaviour that is expected, it means 511 keV gammas are created. On the other hand, if sufficient zoom is applied on the Y axis, the reader can notice that there are also several incidents when positron annihilated in flight and produced two gammas with different energy which in total give more than 1.022 MeV. Only about 5 % of all annihilations are not in rest, nevertheless, this fact should be taken into account.

As well as with neutrons, the initial energy spectrum of positrons is histogramed, again mainly for monitoring purposes. For instance, the initial spectrum for 100 % ^{235}U fuel is shown in Fig. 4.26. This spectrum is strongly dependent on the composition of the fuel.

The properties of IBD are studied, too. Time distribution between positron annihilation and neutron capture which is very important to set the optimal size of the time window between prompt and delayed signal is shown in Fig. 4.27. Also energy deposition of gammas from annihilation and their distances to the first interaction is studied in detail. The results are shown in Fig. 4.28 and 4.29 where the amount of energy deposited in the first interaction and the distance to this interaction is shown for every single gamma from positron annihilation, respectively.

Moreover, efficiency of detection (in their first interaction) of gammas from positron annihilation with respect to the lowest detectable energy E_l in the scintillator can be studied. For instance, if the $E_l = 100$ keV (in DANSSino) the efficiency of detection at least one gamma is 69.84 % and both gammas is 19.26 %. On the other hand for our scintillators the $E_l \simeq 35$ keV and therefore efficiency of detection at least one gamma is 81.69 % and both gammas are detected with efficiency 32.25 %.

Finally, energy deposited in every single plate is evaluated and examined. Efficiency of the antineutrino detection is strongly dependent on the energy threshold E_{thr}. This value should be higher than lowest detectable energy and will affect S/B ratio. Both signals, prompt as well as delayed, are strong enough to be easily distinguished from background events.

Energy depositions in the plates, which are higher than $E_l = 35$ keV, are accumulated and than divided to the two channels (X,Y) and prompt and delayed component, thus enabling to study antineutrino detection efficiency with respect to the E_{thr}. The efficiency of detection is calculated as the ratio of detected events to all events. True antineutrino detection should cause prompt signal with energy higher than E_{thr} in at least one channel (X,Y) and delayed signal with energy higher than E_{thr} in one or both channels in time window shorter than 150 μs. Efficiency of antineutrino detection with respect to the value of E_{thr} is shown in the Tab. 4.5.

	Detection efficiency [%]	
E_{thr} [MeV]	OR condition	AND condition
0.035	39.58	31.70
0.1	39.22	29.11
0.25	38.18	24.46
0.5	35.81	18.72
0.75	32.25	13.94
1	27.83	9.65
1.5	18.26	4.16

Table 4.5: The antineutrino detection efficiency of the detector S^3 with respect to the E_{thr} and with respect to the condition on the delayed signal. If deposited energy has to outreach E_{thr} in both channels (AND) or at least in one channel (OR).

All aforementioned properties and quantities can be studied for completely different geometries of our detector and they are illustrated for the $1\,\mathrm{m}^3$ detector in the Appendix B. There are thousands of quantities and properties which can be studied in detailed thanks to this simulation package and their behaviour with respect to the another parameters can be evaluated. To sum up, this simulation package provides strong method for S^3 detector study and enables to find optimal values of many quantities.

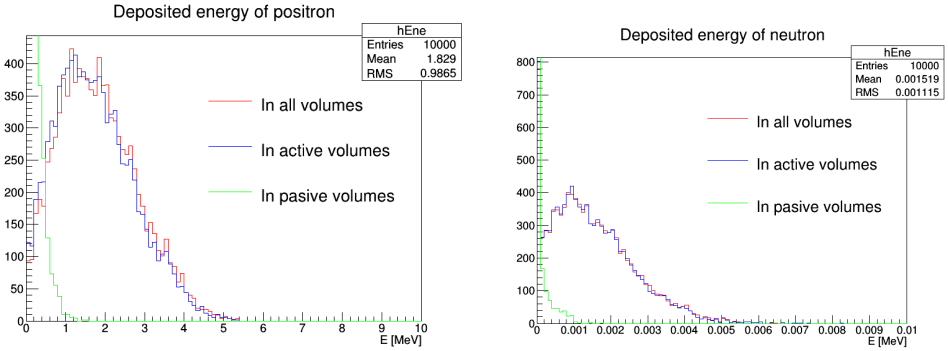

(a)

(b)

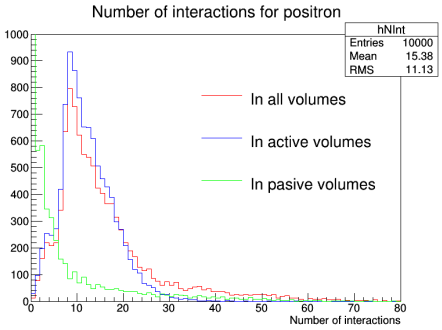

(c)

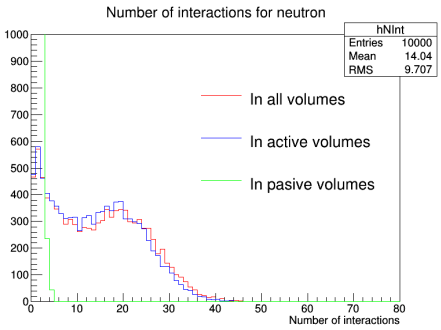

(d)

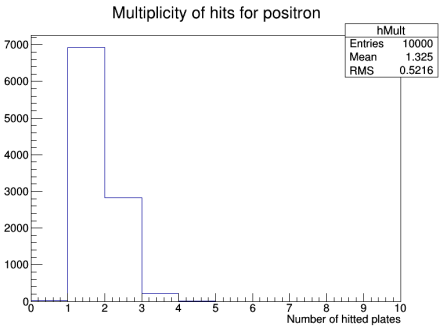

(e)

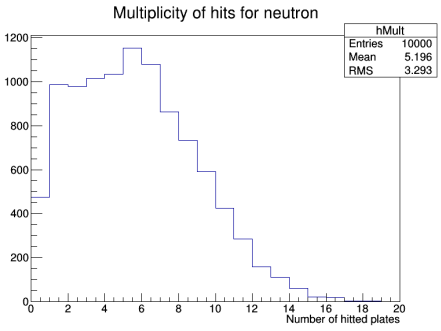

(f)

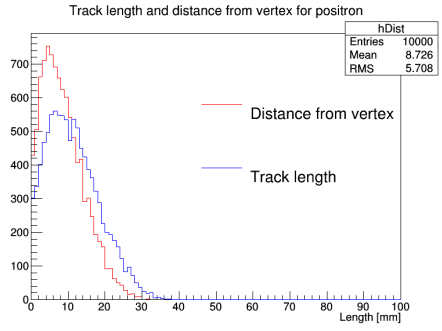

(g)

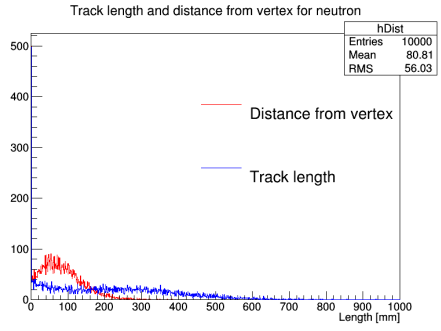

(h)

Figure 4.17: Illustration of basic quantities which can be obtained from simulations directly. The description of individual histograms is closely explained in the text.

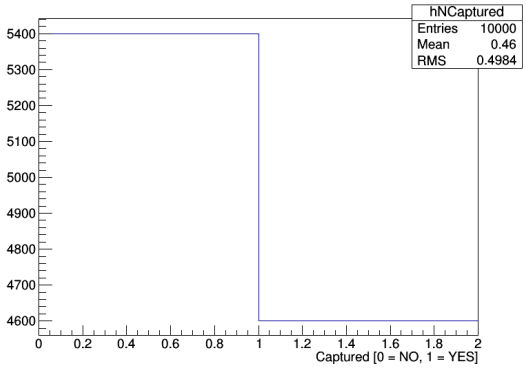

Figure 4.18: Number of neutrons captured on some atom (gadolinium, hydrogen). Bin 0 represents neutrons escaping from the volume of the detector without being captured, on the contrary, bin 1 represents captured neutrons. As you can see, 46.0 % of neutrons is captured in our configuration.

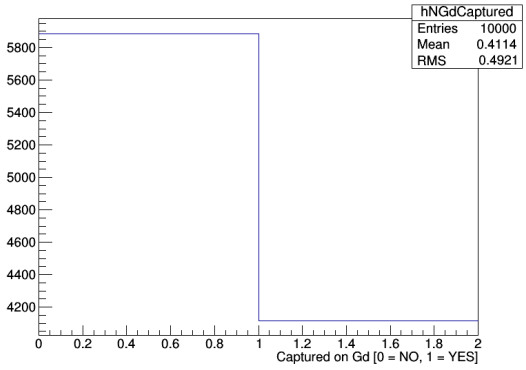

Figure 4.19: Number of neutrons captured and only on gadolinium atom. Bin 0 represents neutrons escaping detector or detected on the hydrogen atom. Bin 1 represents neutrons captured on gadolinium.

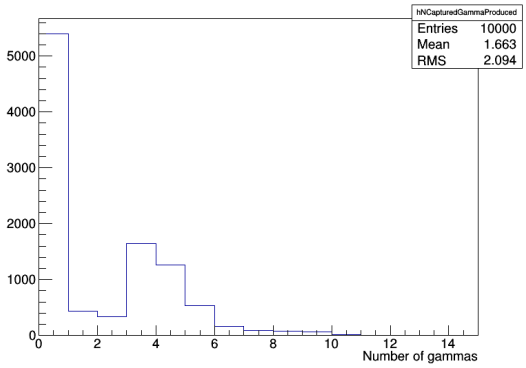

Figure 4.20: Number of gammas created from neutron capture on both types, hydrogen and gadolinium, atoms. If the neutron was not captured, the 0 bin is incremented.

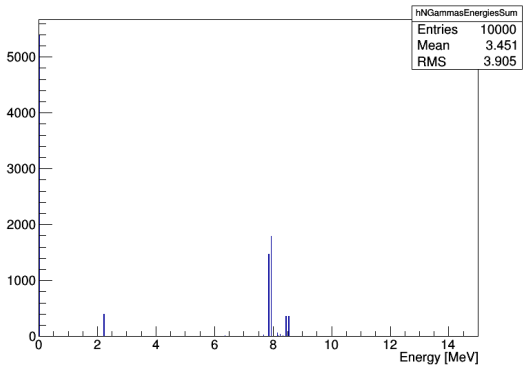

Figure 4.21: Total energy spectrum of gammas produced after neutron capture. Number of captures on hydrogen or gadolinium atoms can be easily determined from the energy released in de-excitation of newly created atom.

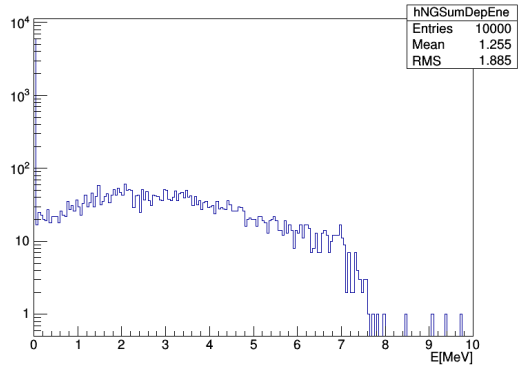

Figure 4.22: The amount of energy deposited in the detector by the gammas produced after neutron capture (Y log scale).

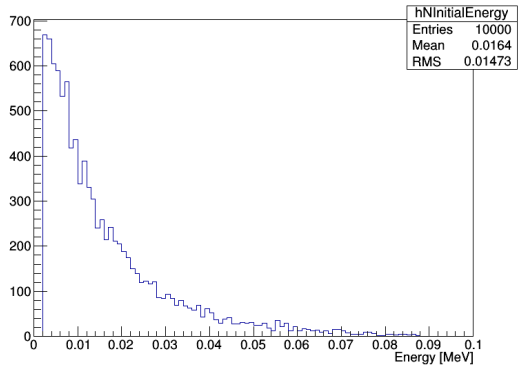

Figure 4.23: Initial energy spectrum of simulated neutrons. This quantity is consistent with input data shown in Fig. 4.15(a).

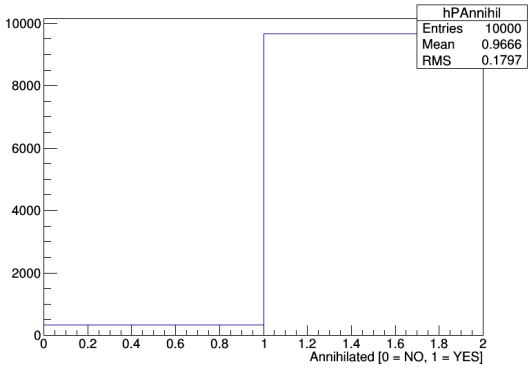

Figure 4.24: Number of annihilated positrons. Bin 0 represents positrons escaping from the volume of the detector without annihilation, on the contrary, bin 1 represents annihilated positrons. The simulation shows that 96.66 % of positrons annihilate in our configuration.

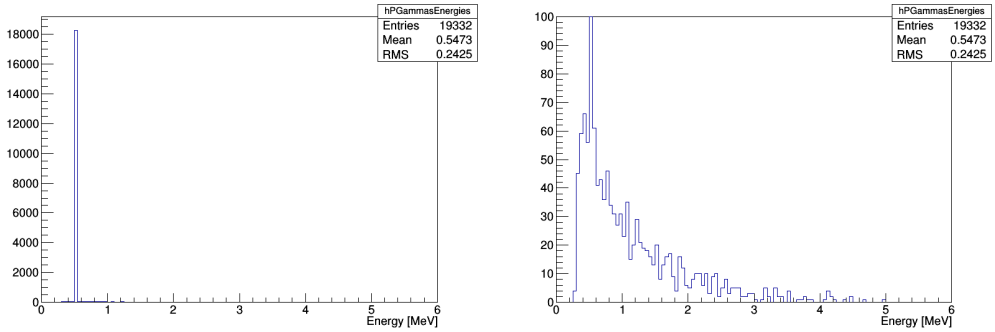

(a) (b)

Figure 4.25: a) Energy spectrum of gammas produced after positron annihilation. b) The same spectrum as in Figure a) with zoom applied on the Y axis. The figure shows that about 5 % of all annihilations takes place in flight when gammas with energies different from common 511 keV are created.

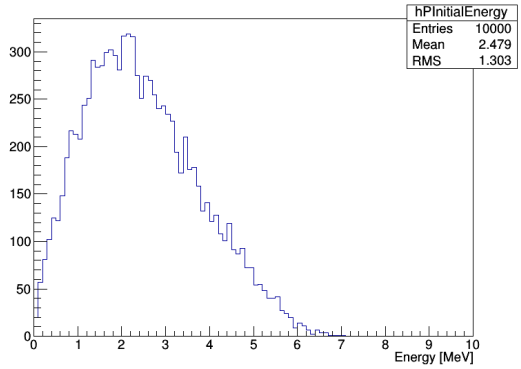

Figure 4.26: Initial energy spectrum of simulated positrons for 100 % ^{235}U fuel. This quantity is strongly dependent on the composition of simulated fuel.

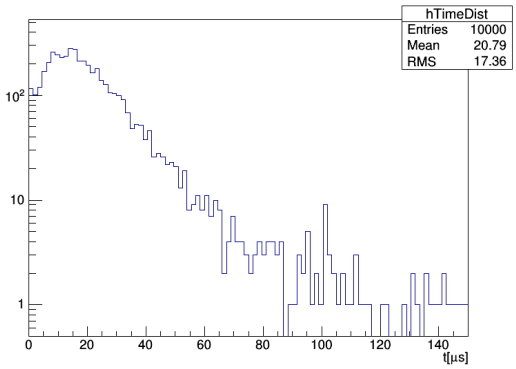

Figure 4.27: Time distribution between positron annihilation and neutron capture (Y log scale). This quantity is very important to set optimal size of the time window between prompt and delayed signal.

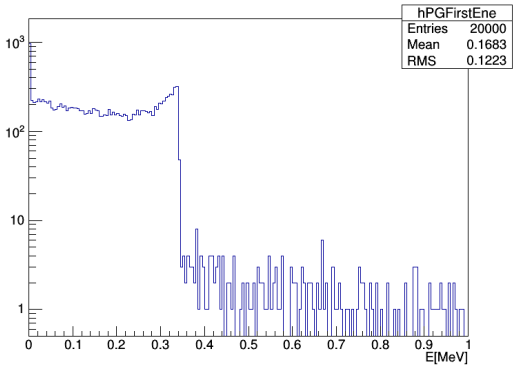

Figure 4.28: Energies deposited by gammas from positron annihilation in their first interaction (Y log scale).

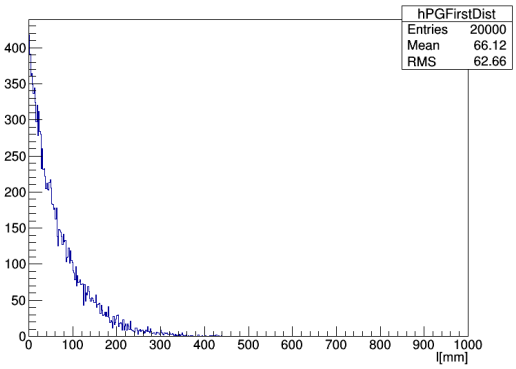

Figure 4.29: Distance to the first interaction of gammas produced after the annihilation of the positron.

5. Optimization of Detection Efficiency

Although we have been building on ideas and experience of our JINR colleagues, individual parts of our experiment, for instance: scintillators, wrapping material, electronics etc., were optimized from scratch because of different geometry and also different production method of the scintillators. For these reasons, it was necessary to perform a considerable number of experiments to optimize individual parts of the detector.

Our main goal, before construction of the detector itself, was the improvement of optical properties of one basic detection element. Results in the experiment DANSSino indicate that even scintillators created by co-extrusion, which is generally considered as a more coarse method than polymerization, are good enough for antineutrino detection. In brief, our ambition were to increase the light production inside the plate and improve the light guidance as well. Both properties are very important from point of view of measuring the positron energy.

The amount of light detected by a photo sensitive element like PMT or SiPM can be expressed in a number of photo electrons (p.e.). The number of p.e. means a number of electrons produced via the photoelectric effect by incident photons emitted from a photocathode inside a PMT. These electrons are then accelerated and multiplied through interaction with dynodes and finally detected as electric signal at anode. PMT conversion efficiency from light to electrons is described by quantum efficiency which is heavily dependent on the wavelength of incident photons. In the case of SiPM, number of p.e. is determined as a number of activated avalanche photodiodes (APD).

An another obstacle to solve was gadolinium application. Two main methods, how to apply gadolinium together with plastic scintillators, are to add it to the scintillator during its production or use a commercially produced gadolinium foil. The former causes significant degradation of optical properties and the latter is very expensive. In other words, it was necessary to invent another method of gadolinium application which would ensure at least the same or even better outcomes together with price reduction.

To sum it up, in order to improve detection efficiency we performed three sets of experiments:

- optimization of chemical composition of the scintillators
- selection of the most suitable reflection material
- finding new method for gadolinium application ,

which will be described in detail in the following sections.

All the measurements were performed at Joint Institute for Nuclear Research (JINR) in Dubna, Russia in cooperation with Russian group led by Mr. V. Egorov. The tests of chemical composition and reflective materials were carried out using cosmic muons and pairs of triggering scintillators. For the experiments with gadolinium was used a neutron source, a moderator and a high purity germanium detector (HPGe).

pTP concentration [$\%_{wt}$]	0.6	1.0	1.5	2.0	2.5	3.0	3.5

Table 5.1: Compared concentrations of the first luminescent additive – pTP.

POPOP concentration [$\%_{wt}$]	0.005	0.010	0.025	0.050	0.100

Table 5.2: Compared concentrations of the second luminescent additive – POPOP.

5.1 Concentration of Luminescent Additives

The scintillators for our detector are produced by polymerization in Czech company Envinet. Basic polystyrene matrix is doped by two luminescent additives (pTP and POPOP) which provide transformation of deposited energy to the visible light. It is well known that amount of these additives influences the light yield and optimal amount is dependent on the size and shape of manufactured scintillators [48]. In Envinet, normally manufactured scintillator contains 0.6 $\%_{wt}$ of pTP (paraterphenyl) and 0.05 $\%_{wt}$ of POPOP.

The goal was to find optimal concentration of pTP and POPOP for our scintillator plates. First of all Envinet produced for us scintillator plates with seven different concentrations of pTP while the POPOP concentration was fixed at the standard value. Secondly after finding the optimal concentration of pTP another scintillator plates were produced this time with fixed optimal concentration of pTP and five different concentrations of POPOP. Studied concentrations of pTP can be found in Table 5.1 and POPOP in Table 5.2. Results of this studies were presented at Low Radioactivity Techniques conference, 2015 in Seattle [49].

Firstly, WaveLength-Shifting (WLS) Kuraray fibers Y-11 with $\oslash$ 1.2 mm had to be prepared for gluing. One end of the fibers were polished and covered by a mirror paint and afterward glued with two-component clear epoxy glue Araldit (Fig. 5.1(a)) into the grooves in the plates. To reduce time, it was decided to use only five fibres from each plate providing sufficient signal strength and statistics. The plates were subsequently wrapped in aluminized mylar foil (Fig. 5.1(b)) and fibres were attached to the 3D-printed adapter for PMT (Fig. 5.1(c)). Fibers from all plates were connected to one PMT (Fig. 5.1(d)) to ensure minimum possible differences in electronic processing. For all our measurements was utilized Hamamatsu photomultiplier R7600U-300 with extended green bialkali photocathode.

As was mentioned above, plates were tested using cosmic muons and pairs of triggering scintillators. Simplified drawing of electronic measurement circuit is shown in Fig 5.2 and in reality was realized by NIM create and modules. The part of the circuit with red connections is used for calibration through LED which allows us to recalibrate our measurement from ADC channels to a number of photoelectrons. The LED is positioned about ten centimetres from the end of one additional fibre (calibration fibre) which is also attached to the PMT and produces calibration flashes with frequency $f = 100$ Hz.

The fibres from plates are attached to the PMT, via optical grease, which is connected to ADC. When incoming particle passes through pair of associated

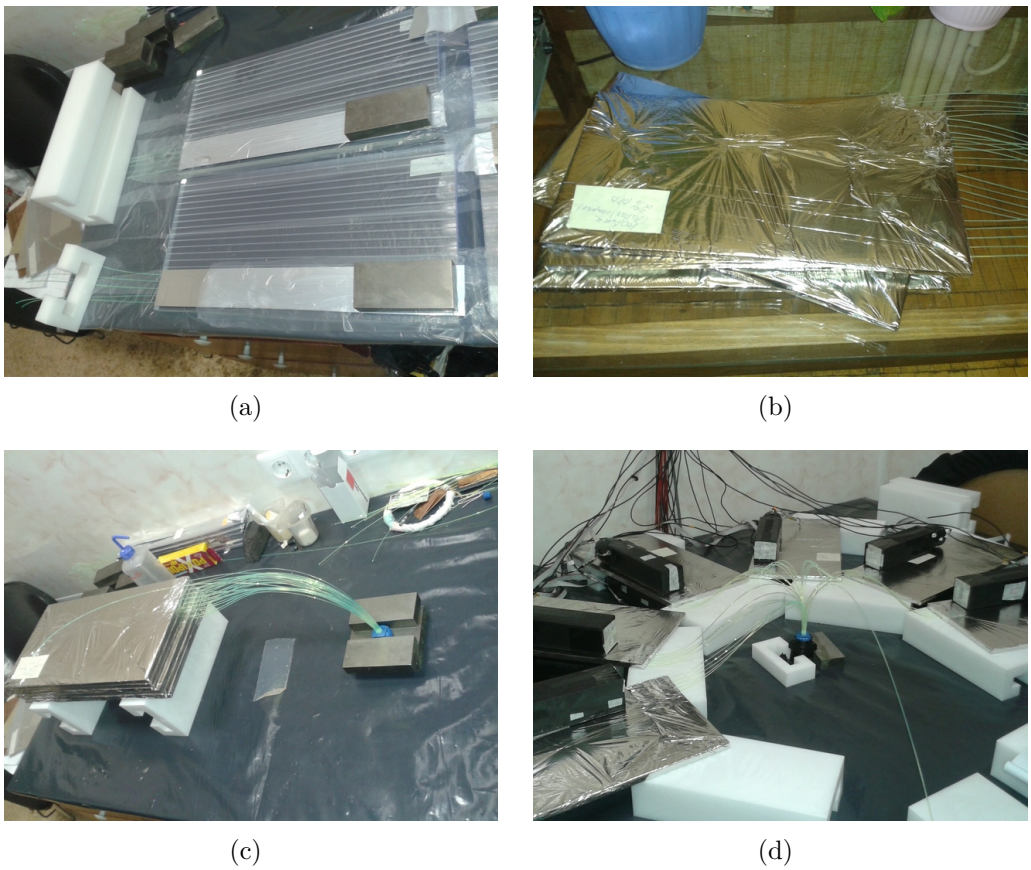

(a) (b)

(c) (d)

Figure 5.1: Preparation of the scintillator plates for the measurement of light yield. a) Plates with glued fibres. b) Scintillators after wrapping. c) Fibres attached to the adapter for PMT. d) Measurement layout.

triggering scintillators this information is recorded in Hodoscope (database of fired channels) and then send to the computer as well as signal strength from ADC. All further processing, like scintillator logic and histogram filling, is done in the programme written in Pascal in a computer.

Every measurement consists of eight measured spectra. One spectrum for calibration LED and seven spectra from scintillator plates associated with seven pairs of the triggering scintillators. It is very difficult to set optimal amplification for signal from PMT because signals with very wide range of strength are measured. On one hand we have to measure signals from LED which have to be weak enough to produce signals about one photoelectron. On the other hand proper signal from plates caused by cosmic muon can reach more than hundred of photoelectrons.

In experiments was used 10-bit charge ADC LeCroy 2249 A with 1024 channels. It was impossible to set such a amplification of signal to fit both low energy part (LED) and high energy part (cosmic muons) into 1024 channels spectrum. The low energy part with LED signal is much more important thus we set higher amplification which resulted in the distortion of higher energy part which was summed in the last bin. Thus we could not use for data processing usual statistical quantities such as mean etc. which would be distorted. For this reason, the

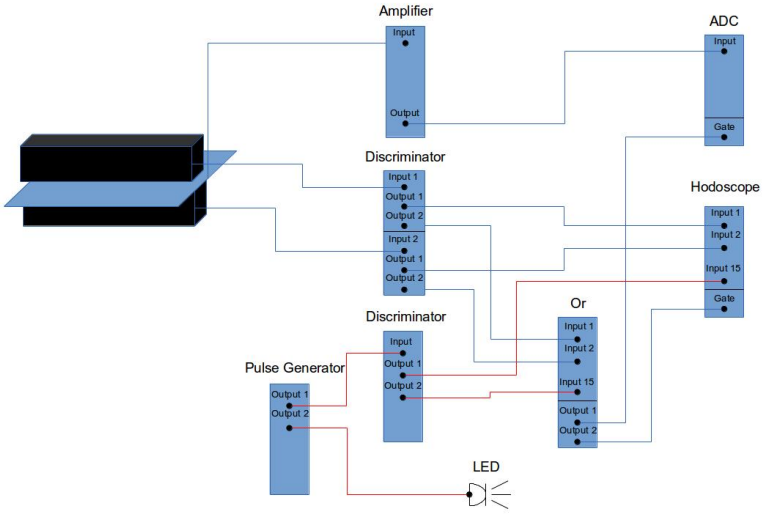

Figure 5.2: Drawing of electronic measurement circuit.

median x_{med} which can be properly calculated and retains its statistical properties as long as is less than 1024 channel was used. Spectra from LED and from plates with different concentrations can be found, for instance, in upper left and right part of Fig. 5.3, respectively.

5.1.1 Calibration

As was mentioned above, LED spectrum is important for recalibration of our x axis from channels to the number of photoelectrons which determine resolution of the detector. The position of LED relative to the end of calibration fibre is adjusted at the beginning of measurement to produce adequately weak signal that in significant number of events signal from LED controlled by external generator do not cause detection of any photoelectrons in the PMT. These events are illustrated by a peak at the beginning of the LED spectra in Figure 5.4. Events, when one or more photoelectrons are detected, are represented in the rest of the spectrum. So the rest of the spectrum is composed from the Gaussian signals corresponding to detection of one, two, three, etc. photoelectrons (Fig. 5.4). Two most important points for calibration are position of zero photoelectron peak x_0 and position of minimum between zero photoelectron peak and the rest of the spectra x_{min}.

To create one photoelectron in PMT, it is necessary to deposit some amount of energy ΔE in the detector. When a particle deposit in the detector energy E, expected number of detected photoelectrons is $k = \frac{E}{\Delta E}$. The expected number of detected photoelectrons will be little bit different in every event due to statistical dispersion. If the signal is weak enough the number of detected photoelectrons k can be described by Poisson distribution

$$\mathrm{P}(k|\mu) = \frac{\mu^k \cdot \mathrm{e}^{-\mu}}{k!} \ , \tag{5.1}$$

where μ is mean number of detected photoelectrons. When we invert this proce-

dure, we can calculate mean number of detected photoelectrons from probability that zero photoelectrons are detected.

$$\mathrm{P}(0|\mu) = \mathrm{e}^{-\mu} \rightarrow \mu = -\ln P(0|\mu) \ . \tag{5.2}$$

The probability $\mathrm{P}(0|\mu)$ is area under the zero photoelectron peak, which is from right bounded by x_{min}, divided by the whole area (number of calibration events). We can also calculate mean channel of calibration spectra $\bar{x}$ corresponding to the μ p.e.. Our calibration parameters a and b from linear calibration

$$k = a \cdot x + b \ , \tag{5.3}$$

where k is number of photoelectrons and x is ADC channel, can be simply calculated from two points. First point is [x_0, 0 p.e.] and second point is [$\bar{x}$, μ p.e.]. At the moment we know a and b, we can calculate number of p.e. k_{med} corresponding to the particular channel such as median x_{med}. From the Monte Carlo simulations developed by the Russian colleagues we also know that the energy corresponding to the median in the spectrum of deposited energy from cosmic muons is $E_{med} = 1.935\,\mathrm{MeV}$. If we combine these two pieces of information we can get number of p.e./MeV easily by dividing k_{med} by E_{med}.

For the comparison of strength of different signals in one single measurement is adequate to compare just median values from the measured spectra. If we want to compare signals from various measurements we have to use number of p.e./MeV which is independent on signal amplification etc.

5.1.2 pTP Concentration

As was already mentioned, seven concentrations of the first luminescent additive (pTP) with fixed concentration $0.05\,\%_{wt}$ of the second luminescent additive (POPOP) were compared. Extensive C library was written for the purpose of data analysis. The analysis itself is performed using ROOT scripts utilizing this library. Measured data are provided in the form of txt files.

The measurement results of optimum pTP concentration are illustrated in Fig. 5.3. In the upper left figure you can see LED calibration spectrum. Upper right figure illustrates measured spectra from the plates with different concentrations. Lower figures show signal strength normalized to signal from plate with standard concentration ($0.6\,\%_{wt}$). Both pictures illustrate the same with different scales on the y axis. An apparent inconsistency between signal for $1.0\,\%_{wt}$ concentration and general trend of the rest of the data is considered to be a systematic error caused during the plate production.

Calculation of the errors is based on the law of error propagation assuming independent variables. As we calculated error of ratio of two medians, the error in median determination had to be computed. If we have histogram with channels on the x axis consisting of N events the median is channel which contains the $N/2^{\mathrm{th}}$ event. The error in median determination can be calculated as $\sigma_m = \max\{x_m - x_l, x_u - x_m\}$ where x_m is median and x_l and x_p are channels which contain $(N - \sqrt{N})/2^{\mathrm{th}}$ and $(N + \sqrt{N})/2^{\mathrm{th}}$ events, respectively. This errors are added in quadrature with the error caused by inhommogenities in scintillators production and fibres gluing which was calculated in experiment where three identical scintillator plates were glued and measured and is equal $\sigma_i = 12.0\,\mathrm{bins}$.

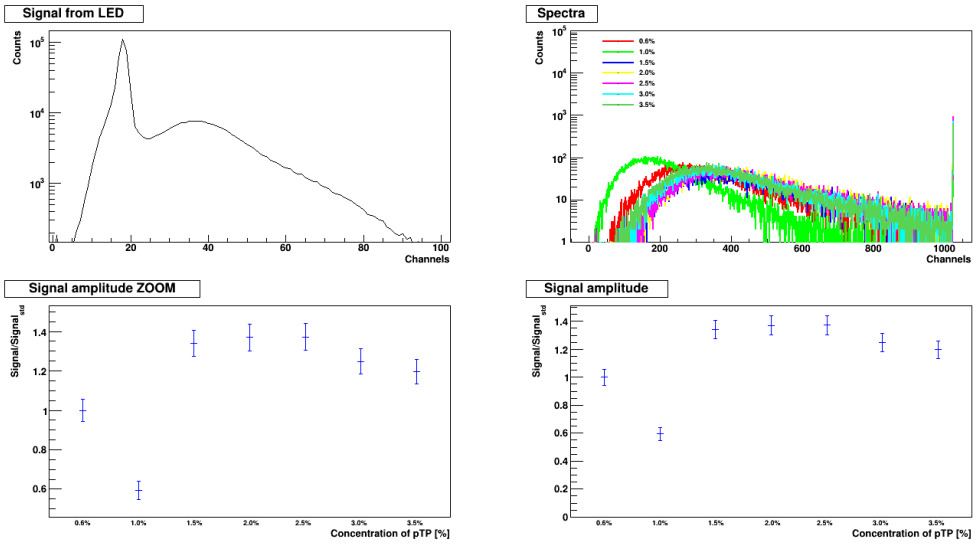

Figure 5.3: Results of pTP concentration comparison experiment. Description of individual figures can be found in the text.

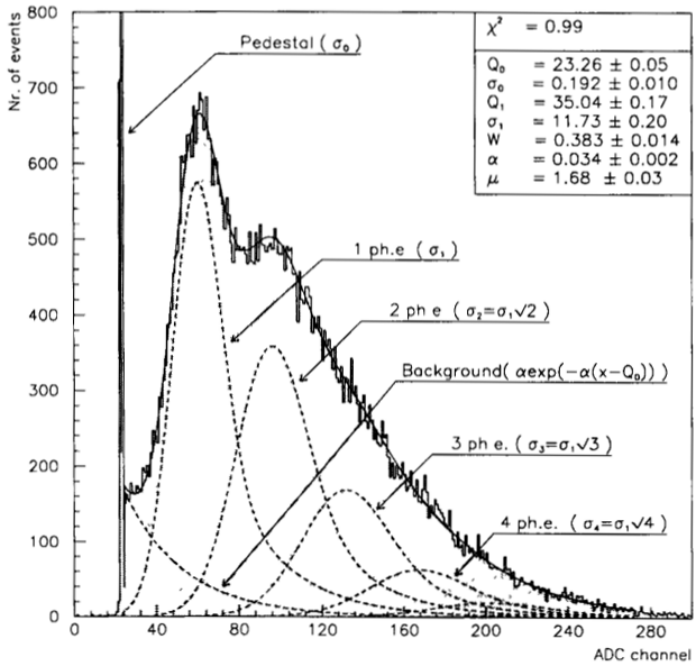

Figure 5.4: LED calibration spectrum with outlined Gaussian signals for different signal strength [50].

Parameter	value
No. events	551 855
x_0 [channel]	18
x_{min} [channel]	23
$\bar{x}$ [channel]	27.11
μ [p.e.]	0.48
a [p.e./channel]	0.052
b [p.e.]	-0.95
x_1 [channel]	36.9
x_1 [channel]	55.8

Table 5.3: Parameters of calibration for pTP concentration measurement.

pTP con [$\%_{wt}$]	0.6	1.0	1.5	2.0	2.5	3.0	3.5
No. events	16 878	19 287	14 296	18 204	16 628	17 042	17 928
Median [chnl]	303	180	406	415	416	378	363
σ_{Median}	12.0	12.0	12.2	12.2	12.2	12.2	12.2
Signal/Signal$_{std}$	1.00	0.594	1.34	1.37	1.37	1.25	1.20
$\sigma_{\text{Signal/Signal}_{std}}$	0.06	0.046	0.07	0.07	0.07	0.06	0.06
No. p.e./MeV	8.28	4.92	11.1	11.3	11.4	10.3	9.92

Table 5.4: Results for pTP concentration measurement.

Selected values of boundaries for calibration calculation and obtained parameters are included in Table 5.3. x_1 and x_2 represent calculated mean positions of 1 p.e. peak and 2 p.e. peak (Fig 5.4), respectively, which can sometimes provide visual control, when peaks are visible in the LED spectrum.

Obtained results for different concentrations in the form of medians and also in the form of number of p.e./MeV are shown in Table 5.4. The table also contains results expressed as the ratio of signal strength to the signal strength from plate with standard concentration of pTP.

In conclusion, in the experiment was shown that the light yield of our scintillation plates is heavily dependent on the amount of the first luminescent additive and that optimum amount is between 2.0 $\%_{wt}$ and 2.5 $\%_{wt}$. With regard to the price the 2.0 $\%_{wt}$ option was chosen to be used in the detector prototype. Due to this experiment the light yield was improved 1.37 times compared with the signal from standardly produced scintillators.

5.1.3 POPOP Concentration

After optimization of the first luminescent additive, new set of scintillator plates were produced this time with fixed concentration of pTP (2.0 $\%_{wt}$) and with variable concentration of second luminescent additive – POPOP. Envinet produced for us five plates with different POPOP concentration ranging from 10 % to 200 % of standard concentration (0.05 $\%_{wt}$).

The newly produced plates were again taken to the JINR and were measured

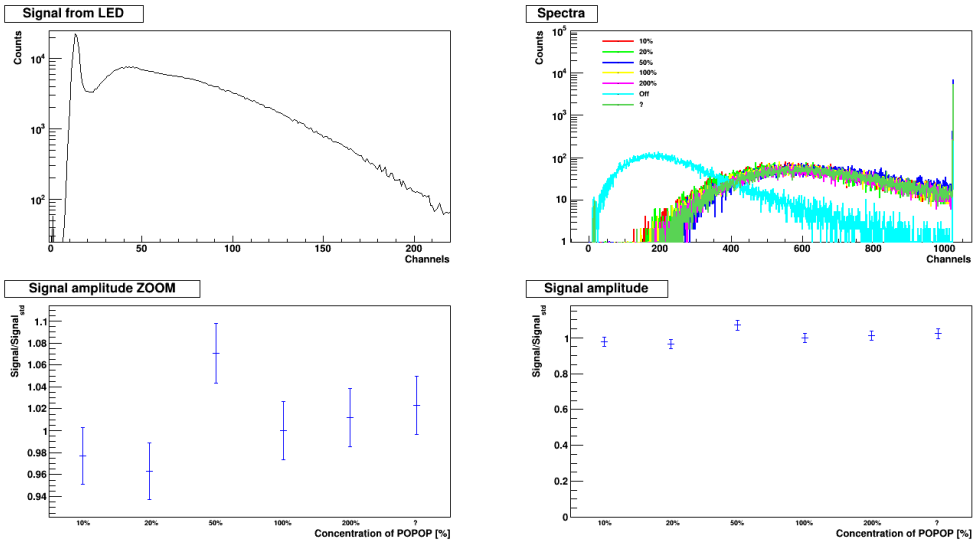

Figure 5.5: Results of POPOP concentration comparison experiment. Description of individual figures can be found in the text.

Parameter	value
No. events	651 879
x_0 [channel]	13
x_{min} [channel]	22
$\bar{x}$ [channel]	63.6
μ [p.e.]	1.81
a [p.e./channel]	0.036
b [p.e.]	-0.47
x_1 [channel]	40.9
x_1 [channel]	68.9

Table 5.5: Parameters of calibration for POPOP concentration measurement.

using the same method as in the case of pTP it means cosmic muons and pairs of triggering scintillators. Since we had seven pairs of triggering scintillators avaible but at the same time just five investigated plates we decided to use one unused triggering pair in order to determine POPOP concentration of one plate where the POPOP concentration was not known from the producer. Data from this plate are in figures labeled by question mark instead of known concentration. Seventh pair labeled by "Off" sign was located on one randomly chosen plate however not in the region where the fibres were glued which explains much lower light yield.

Selected values of boundaries for calibration calculation and obtained parameters are included in Table 5.5. Results of POPOP concentration measurement are illustrated in Figure 5.5 and in Table 5.6. LED calibration spectrum is illustrated in the upper left picture. Upper right picture again illustrates measured spectra from plates with different concentration. Lower pictures show resulting medians normalized to median from plate with standard POPOP concentration with two different ranges on the y-axis.

POPOP con [$\%_{wt}$]	0.005	0.010	0.025	0.050	0.100
No. events	31120	29752	31840	28989	26864
Median [chnl]	638	629	699	653	661
σ_{Median}	12.2	12.2	12.2	12.2	12.2
Signal/Signal$_{std}$	0.977	0.963	1.07	1.00	1.01
$\sigma_{\text{Signal/Signal}_{std}}$	0.026	0.026	0.03	0.03	0.03
No. p.e./MeV	11.8	11.6	12.9	12.1	12.2

Table 5.6: Results for POPOP concentration measurement.

Both the figure and the table indicate that the concentration of POPOP has no significant influence on the light yield of plates, hence determination of POPOP concentration for the plate with unknown concentration is impossible. Results indicate that, within the error, light yield is already saturated with POPOP concentration at least ten times smaller than standard concentration. Thus, much smaller amount of very expensive POPOP could be used in plates in the detector prototype which will lead to price reduction. On the other hand the amount of added POPOP is already so small that savings will not reach staggering sums.

From comparison of results for pTP and POPOP we can summarize that influence of pTP concentration is much more significant than POPOP concentration. Both data sets are shown in Figure 5.6, when POPOP data set is normalized through the common point with 2 $\%_{wt}$ pTP and 0.05 $\%_{wt}$ POPOP. Small discrepancy in the number of p.e. in these two measurements is caused by different wrapping procedures in pTP and POPOP experiment.

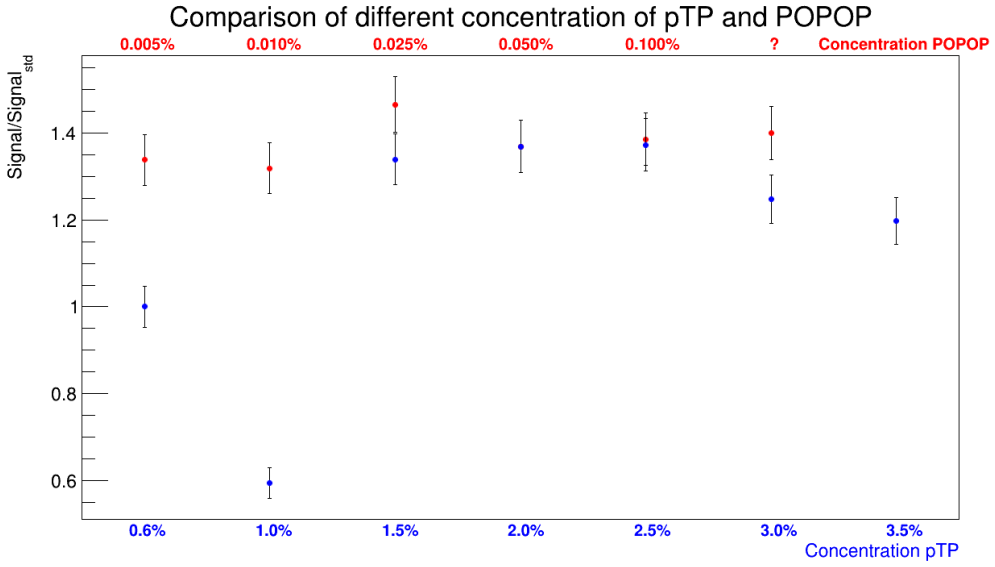

Figure 5.6: Combination of results from pTP and POPOP optimization experiments.

5.2 Wrapping Material

After optimization of chemical composition, the selection of the most suitable wrapping material was carried out. In the experiment DANSSino the reflective surface coating was produced by co-extrusion during the scintillator production. Scintillator production using polymerization does not allow to use this method and is thus necessary to use external reflective foil or paint.

In our test two plates with all 19 fibres glued (in each plate) were used. Ten fibres with diameter 1.2 mm from both plates were attached to the PMT and nine fibres from both plates with diameter 1.0 mm were not used in this experiment however will be used in the experiments with SiPM, when signals from both SiPM and PMT will be compared.

Between individual measurements was necessary to change wrapping material which required to enter the dark room, manipulate with tested plate and switch off and on High Voltage (HV) generator for PMT. To avoid uncertainties associated with all above mentioned changes we used one plate as a reference (no changes were applied for this plate) to observe potential changes in the signal strength which were not caused by a change of wrapping (different temperature, HV stability, fibres position, etc.).

The reference plate was measured without any wrapping (bare) and with three pairs of triggering scintillators. Second plate, so called PUT (plate under test), was measured with four pairs of triggering scintillators and with different wrapping materials. Geometry and examples of wrapping materials are illustrated in Fig. 5.7.

Tested wrapping materials can be divided into two groups:

- Specular reflectors - mirror-like reflection
- Lambertian reflectors - diffuse reflection

while the former group is recommended for scintillators with spherical shapes (cubes etc.) and latter for scintillators where one side is significantly bigger than the others (our case). The list of all examined materials together with the assignment to the individual reflective groups is presented in Table 5.7. The bare plate as well as a large number of standardly used wrapping materials were tested, for instance: three different types of tyvek from Russia and the Czech Republic, two different types of mylar and reflective paint based on TiO_2 from the Envinet company. The structured mylar is material whose surface is very similar to usual mylar except that it is not completely smooth but is covered with small protrusions.

Maximum light yield characterized by the value of median is as well important as the homogeneity of the light collection. As was mentioned before, PUT were studied with four pairs of triggering scintillators which were located at positions $l_1 = 5\,\text{cm}$, $l_2 = 15\,\text{cm}$, $l_3 = 25\,\text{cm}$ and $l_4 = 35\,\text{cm}$ from the edge where fibres emerge plate to test the homogeneity. Results of the experiment are shown in Fig. 5.8 and in Table 5.8. In the table are shown medians (described in detail in Sec. 5.1) measured at positions l_1 to l_4 with errors of median determination σ_m described in Section 5.1.2 and homogeneity H calculated by the equation

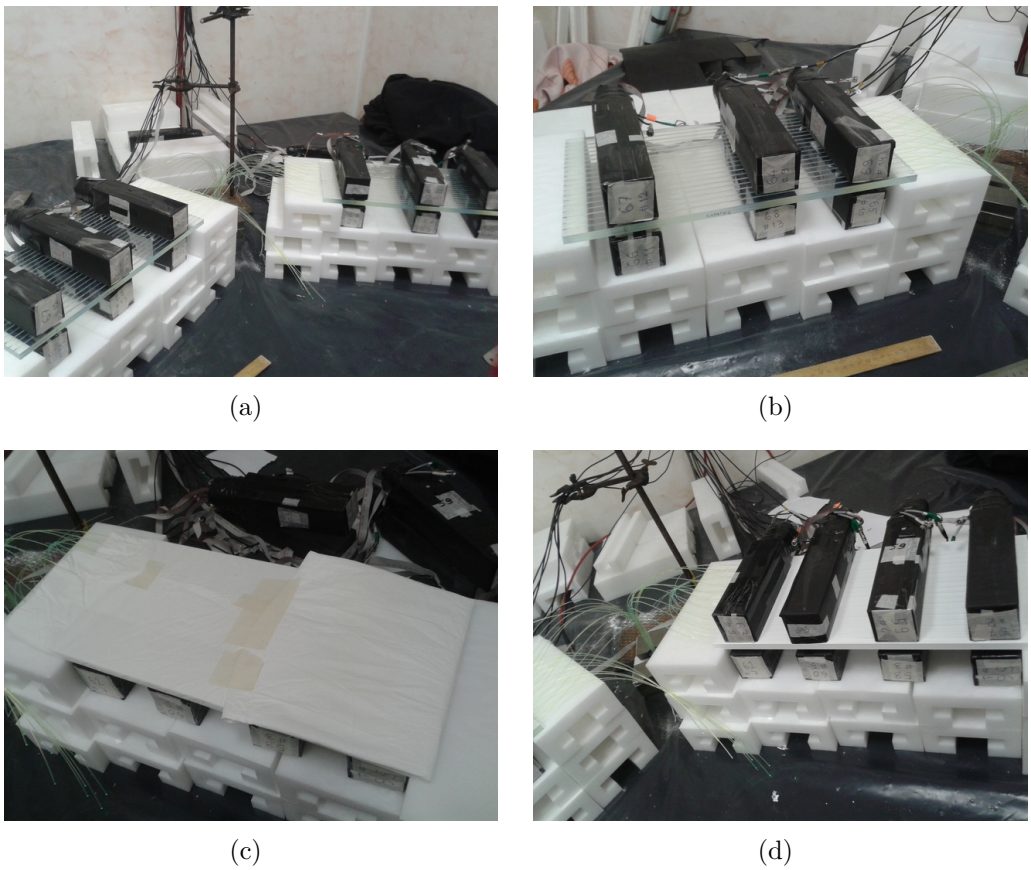

(a) (b)

(c) (d)

Figure 5.7: Measurement of wrapping materials. a) Experimental arrangement. b) Reference plate. c) PUT with tyvek wrapping. d) PUT with TiO_2 paint.

$$H = \frac{\text{Median}_4}{\text{Median}_1} \ , \tag{5.4}$$

which describes attenuation of signal depending on the position simply as the strength of the signal at l_4 relative to l_1. In this experiment is not necessary to count with σ_i which is caused by inhomogeneity in plate production and preparation (wrapping, gluing) because all measurements were carried out on the single plate and thus these effects have no influence. On the other hand with the reference plate variance in the medians was found to be $\sigma_{ref} = 3.64$.

Figure 5.8 illustrates results shown in Table 5.8 normalized to the value Median_1 for the bare plate in two distinct ways. Upper figure is showing positions of triggering scintillators on the x-axis and the ratio of appropriate medians on the y-axis while materials are distinguished by colors. Lower figure is showing materials on the x-axis and positions are distinguished by colors. Lower image much better illustrates H which is indicated by the spread of values for individual materials. Errors are smaller than the size of markers and are calculated by the error propagation while error of one median is calculated as σ_m and σ_{ref} added in quadrature.

In conclusion, if we take into account both studied parameters, value of light yield as well as homogeneity, and try to choose the best material to maximize

Material	Specular	Lambertian
Mylar	x	
Structured mylar	x	x
Bare plate	x	
Tyvek paper (CZE)		x
Tyvek Tim (Rus)		x
Tyvek Rhl (Rus)		x
Teflon		x
White paper		x
Envinet's (TiO_2) paint		x

Table 5.7: Examined wrapping materials with the assigment to the individual reflective groups.

Material	Median_1	Median_2	Median_3	Median_4	H [%]
Mylar	476 ± 3	429 ± 2	387 ± 2	359 ± 2	75.42 ± 1.15
Structured mylar	435 ± 3	398 ± 4	355 ± 2	325 ± 3	74.71 ± 1.35
Bare plate	289 ± 2	264 ± 2	230 ± 3	207 ± 1	71.63 ± 1.66
Tyvek paper (CZE)	529 ± 1	471 ± 2	423 ± 1	394 ± 2	74.48 ± 0.95
Tyvek Tim (Rus)	422 ± 4	382 ± 3	340 ± 3	318 ± 4	75.36 ± 1.61
Tyvek Rhl (Rus)	516 ± 1	466 ± 1	420 ± 1	393 ± 1	76.16 ± 0.92
Teflon	522 ± 2	489 ± 2	453 ± 1	419 ± 1	80.27 ± 0.97
White paper	425 ± 2	386 ± 3	348 ± 2	323 ± 2	76.00 ± 1.23
Envinet's paint	410 ± 3	361 ± 2	313 ± 2	285 ± 2	69.51 ± 1.29

Table 5.8: Medians with different materials and positions $l_1 = 5\,\text{cm}$, $l_2 = 15\,\text{cm}$, $l_3 = 25\,\text{cm}$ and $l_4 = 35\,\text{cm}$ from the edge where fibres exit the plate and homogeneity H.

both these parameters at once we get teflon as material with relatively high light yield which is in average 1.6 times higher than light yield of bare plate and with homogeneity exceeding 80 % which is by far the best result of all studied materials.

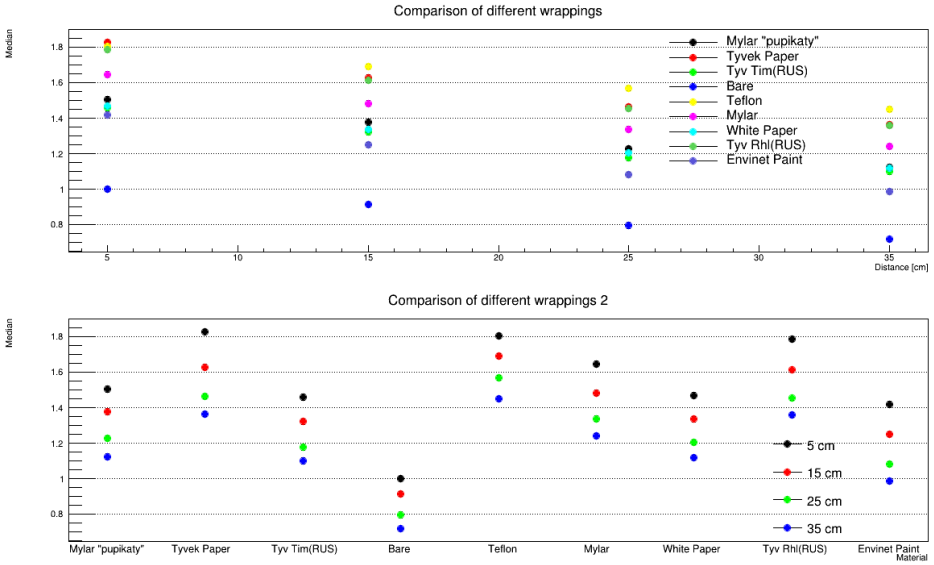

Figure 5.8: Results of the wrapping materials measurements. Both figures illustrates obtained medians normalized to the value Median_1 for the bare plate. The upper figure illustrates these values with respect to position of the triggering scintillator. The lower figure illustrates the same, however with respect to the measured materials. Errors of individual data points are smaller than size of the point.

5.3 Gadolinium

Next inalienable part of the experiment S^3 is layer providing conversion neutrons from IBD reaction to gammas which can be detected in the scintillator plates. Gadolinium is standardly used for this task due to its high cross section for thermal neutrons. Whereas in the experiment DANSSino gadolinium was added into the reflective layer produced by co-extrusion, in the experiment S^3 was decided to use gadolinium foil whereas application of gadolinium into the volume of scintillator during the production significantly worsens the optical properties and thus the energy resolution. Our original plan was to buy commercially produced gadolinium foil, however astronomically high price of the foil (for instance 419 £ per 5 x 5 cm^2 of 99 % purity gadolinium foil from GoodFellow company) would increase costs several times over the planned budget.

It was decided to test another compounds and application methods of gadolinium in order to obtain the same efficiency to neutron capture simultaneously with price reduction. Two gadolinium compounds

- $GdCl_3$ (gadolinium trichloride) - 99.99 % purity, water-soluble
- Gd_2O_3 (gadolinium oxide) - 99.9 % purity, insoluble in water

in the form of powder were bought in company Sigma-Aldrich for 20 979 and 5 697 CZK per 25 g, respectively. Moreover two simply achievable application methods were planned to be tested

- Home-made foil - application of powder on the scotch tape
- Gadolinium solution - aqueous solution of gadolinium and its application to paper towels.

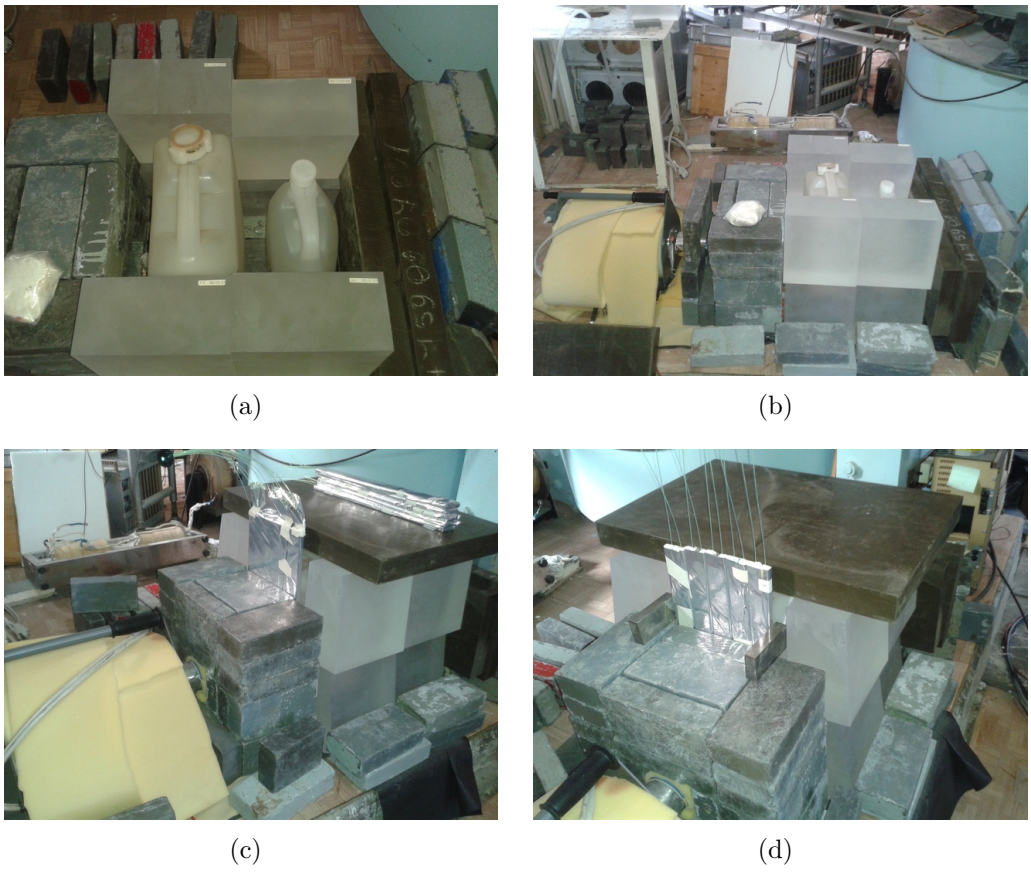

(a) (b)

(c) (d)

Figure 5.9: Measuring apparatus composed of neutron source, shielding and HPGe detector for gadolinium layer testing. a) Detail of shielding. b) Whole testing apparatus. c) Envinet plate testing. d) Testing of DANSS strips.

All measurements were again carried out in JINR, Dubna, Russia using measuring apparatus (see Figure 5.9) composed of neutron source, neutron and gamma shielding and HPGe detector. The PUT with layer of gadolinium was located between neutron source and the germanium detector. As was mentioned gadolinium's cross section for neutron capture is huge. The biggest cross section $\sigma = 255\,\text{kb}$ has isotope ^{157}Gd with the abundance 15.68 %. When neutron capture occurred a newly produced atom is in excited state and subsequently release this energy in the form of gamma cascade. The energy of the most intensive gamma line produced in the neutron capture by ^{157}Gd is $E = 181.9\,\text{keV}$ with total cross section 7200 kb and intensity 139 produced gammas per 100 neutron captures [51].

As source of neutrons was used plutonium-beryllium (Pu-Be) emitter which produces wide energetic range of neutrons. Produced neutrons were moderated by approximately ten centimetres of water and then were captured on Gd and produced gammas. Some of these gammas were consequently detected by HPGe detector with volume 100 cm^3 located behind the plate. Data processing consisted of the analysing the spectrum from HPGe detector and evaluating the number of events in the Region Of Interest (ROI) about 181.9 keV.

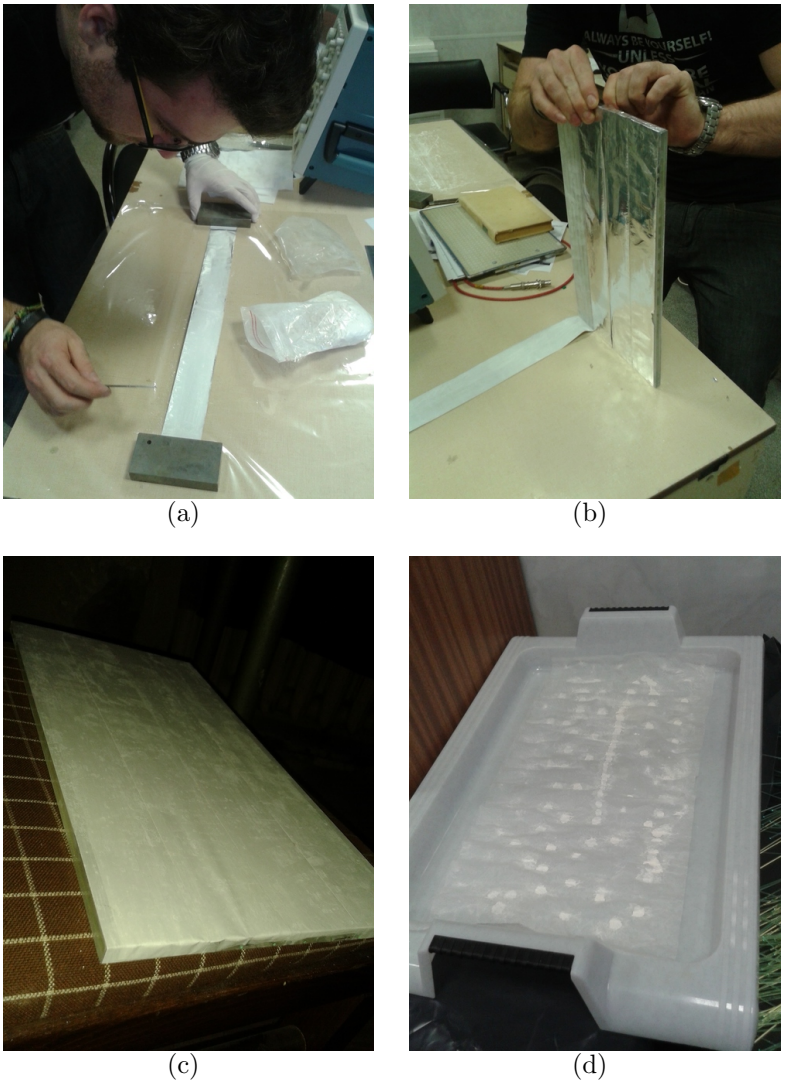

(a) (b)

(c) (d)

Figure 5.10: Alternative methods of gadolinium application. Production and illustration of use. a) Foil production. b) Foil mounting. c) Plate with gadolinium foil. d) Gadolinium "napkin".

The measurements were not analysed in the absolute number of neutron captures. In fact, it was comparative measurement, when results obtained from one S^3 scintillator plate with different layers of gadolinium were compared with the results obtained from strips used in the experiment DANSSino, which were used as an etalon. Our goal was not to determine exact amounts, but rather show that even much more cheaper methods can be used without loss of efficiency.

Measurements were performed with two compounds and two application methods of gadolinium. Gd_2O_3 is cheaper version, however is insoluble in water which can be an obstacle when you try to do a aqueous solution. Our first attempt was to apply Gd_2O_3 on the different types of a scotch tape – common one used in the offices and aluminized one. The production of such a "home-made" gadolinium "foil" is shown in Fig. 5.10(a) and its application on the surface of a scintillator plate is shown in Figures 5.10(b) and 5.10(c) for alluminized one and regular one, respectively. We also experimented with a number of layers and with arrangement, for instance gadolinium layer - plate - gadolinium layer ("sandwich" arrangement) or two gadolinium layers on one side of plate.

The second tested application method was production of aqueous solutions from 20 ml of water and both gadolinium compounds with the various amount of gadolinium from 0.5 to 2.5 g. These solutions were then applied on the sheets of a highly absorbent and very thin paper. Thereafter, wet papers were left at the warm place until they dried up. Subsequently dry papers with layers of gadolinium were attached to the plates and measured. $GdCl_3$ due to its water-soluble character creates homogeneous solution and after application on the paper and drying there were not any visible changes and paper was covered with gadolinium homogeneously. On the other hand Gd_2O_3 is insoluble in water and when we applied the solution on the paper, spots with high concentration of gadolinium were created which resulted in inhomogeneous gadolinium coverage (see Fig. 5.10(d)).

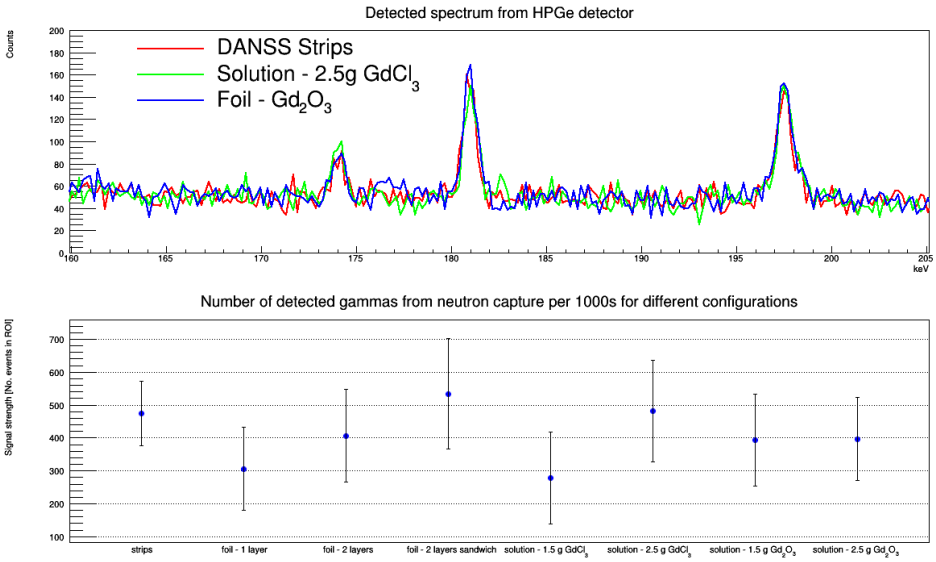

Figure 5.11: Results of experiments with gadolinium application methods and compounds. The upper figure illustrates the part of the measured spectrum from HPGe around 181.9 keV for three specific variants. The lower figure illustrates results for a various range of possibilities of application and concentration with the size of area under the 181.9 peak on the y-axis.

All measured spectra were analysed using short script utilizing our own aforementioned C library. Results for a few examined combinations are illustrated in Fig. 5.11. The upper figure illustrates the part of the measured spectrum from HPGe about energy of 181.9 keV where should be signal from a neutron capture for three specific variants – DANSS strips which hold as an etalon and versions

Variant	Peak area [No. events]
DANSS strips	474 ± 98
One layer of foil	306 ± 126
Two layers of foil	407 ± 140
"Sandwich" arrangement	534 ± 168
Solution - 1.5 g $GdCl_3$	279 ± 140
Solution - 2.5 g $GdCl_3$	481 ± 154
Solution - 1.5 g Gd_2Cl_3	393 ± 140
Solution - 2.5 g Gd_2Cl_3	397 ± 126

Table 5.9: Results for measurement with different gadolinium compounds and application methods. Detailed description of individual variants can be found in the text.

with the solution and the foil. The lower figure shows results for the wider range of variants. On the y-axis is plotted area of the 181.9 keV peak. Exposition time of every single measurement was relatively short $t = 1000$ s due to limited time and a large number of tested variants. For this reasons, errors are quite large however this measurement proved that both application methods, under certain conditions, are able to provide sufficiently good results.

The area of peak was calculated as a signal - background in every bin in ROI, while the background strength was estimated by a fit with a polynomial of the first order in the range (175,195) keV except the signal region (180,182) keV. Thereafter, the value of background strength $B \pm \sigma_B$ was used to estimate the areas which are reported in Table 5.9 and in the upper part of Fig. 5.11.

6. Construction of the Detector S^3

In March 2015 we obtained first 20 scintillation plates with new improved chemical composition for the construction of the detector S^3 from the producer. Our first goal was to prepare every single plate for measurements. The whole preparing procedure was delayed by the fact, that producer made grooves narrower than is necessary for the fibres, thus grooves had to be widened first (see. Fig 6.1(a)). Next every plate was cleaned, ten WLS fibres were cut (Fig. 6.1(b)) and glued into odd grooves by transparent two component epoxy glue (Fig. 6.1(c)) while the ends of the fibres were polished with sandpapers with four different roughness and with grinding paste and after that the plates were wrapped into four layers of teflon, which was chosen as an optimal reflective material for the plates (see Sec. 5.2), from all six sides (see Fig. 6.1(d)). The complete preparation process of one scintillation plate takes about 2 days in total.

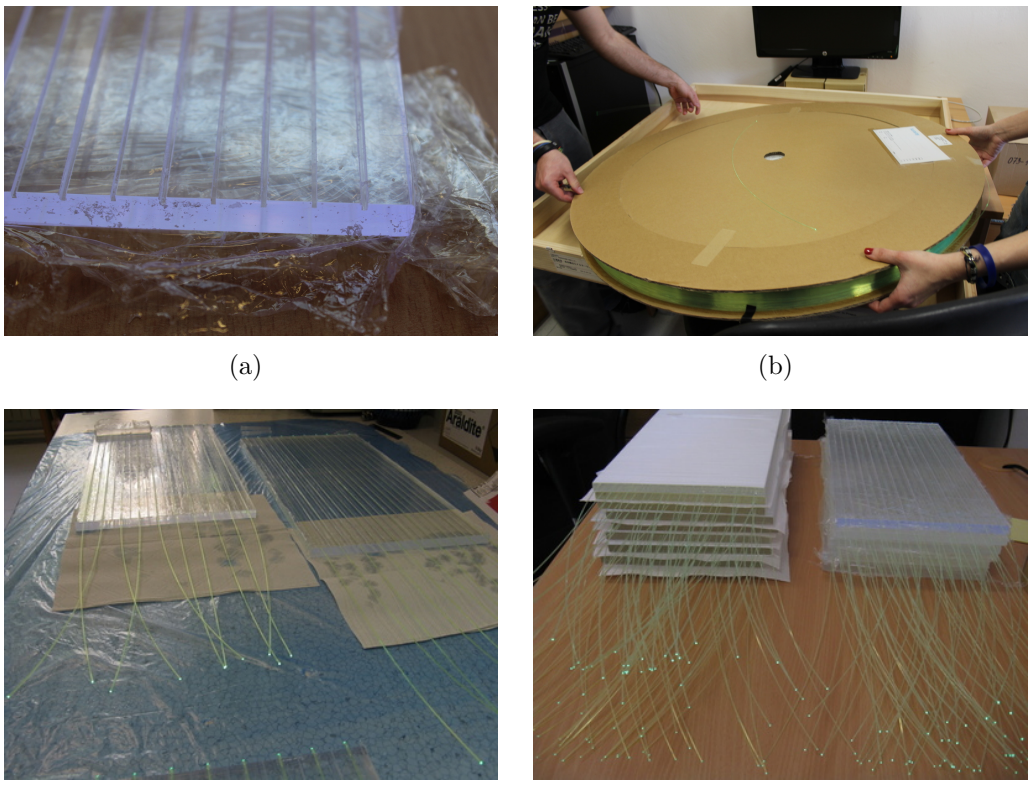

(a) (b)

(c) (d)

Figure 6.1: Preparation of the newly produced scintillator plates for the measurement of light yield. a) Grooves widening. b) Fibres cutting. c) Fibres glueing. d) Plates wrapping.

6.1 Plates Testing

In order to identify the differences in light production between individual plates, it was decided to test every scintillation plate by cosmic muons. The differences could be caused by the inaccuracies during the production of the scintillation plates or by the inaccuracies during the fibres gluing and plates wrapping (air bubbles between teflon and plates may cause poor optical contact and thus light leakage) which will be very difficult to prevent in next batch of scintillators.

For the testing with cosmic muons the small holder for one plate was created (see Fig. 6.2(a)). It is wooden desk with two metal straps for plate fixing and with plastic adapter for PMT where fibres from plate are attached. On every plate the fibres were brought together and fixed by heat-shrink tubing without heating (Fig. 6.2(b)). Then plate was fixed in the holder and PMT (R7600U-300) was attached to the adapter by electrical scotch. In the first measurements the plates were also wrapped in black paper and WLS fibres were tucked inside the heat-shrink tubing (see Fig. 6.2(c)).

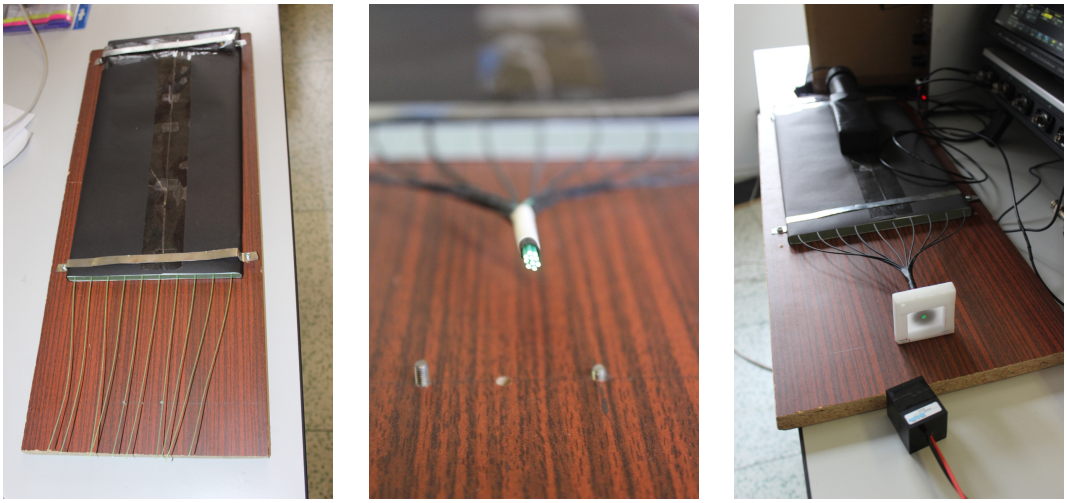

(a) (b) (c)

Figure 6.2: Photos of the holder for testing individual scintillation plates. a) Holder with plate. b) Ten fibres from one plate bring together and fixed by heat-shrink tubing. c) Complete holder with fixed plate and PMT ready to be attached. On the end of the plate is visible small triggering scintillator wrapped in a black paper.

The PMT bias was set to -800 V according to the datasheet and signal was detected by the 12-bit digital oscilloscope with 2 GS/s. The whole measuring system is shown in Fig. 6.3 and the results of the measurement in Fig. 6.4. The pink waveform is signal from triggering scintillator, the yellow waveform is the signal from plate under test. The yellow histogram stores areas of signal from plate and the pink histogram holds amplitudes of these signals. Both histograms show the cosmic muon spectrum.

Due to the measurements with cosmic muons it was found that the producer of the scintilation plates was not able to keep the same production standard in the thickness of the scintillators for all 20 scintillators. We measured the thickness of

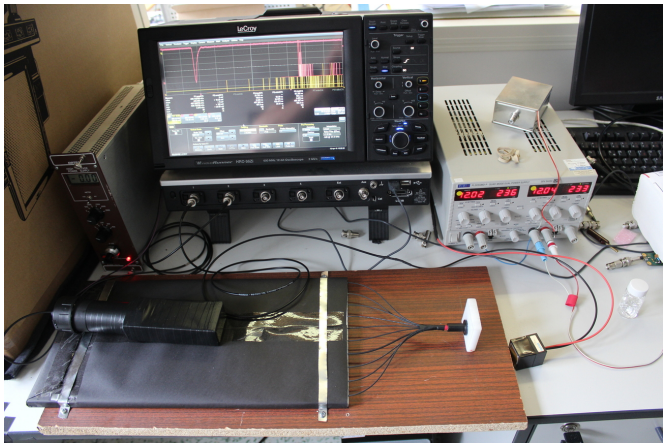

Figure 6.3: Photo of the whole measuring system. Testing holder, plate, PMT, digital oscilloscope, and high voltage.

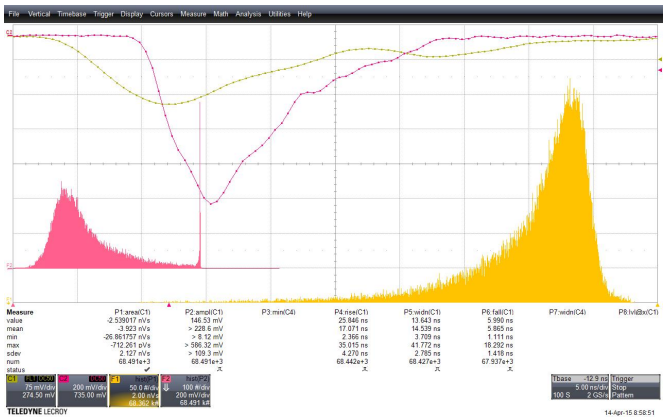

Figure 6.4: Print screen of the oscilloscope for one plate testing with cosmic muons. The pink waveform is signal from triggering scintillator, the yellow waveform is the signal from plate under test. The yellow histogram stores areas of signal from plate and the pink histogram holds amplitudes of these signals. Both histograms show the cosmic muon spectrum.

every plate in six positions and we found out that there are significant differences in thickness within one plate and also across the plates. This fact forced us to re-measure the thickness of scintillators tested at JINR which were produced by the same company, however these scintillator plates were produced with equal thickness. Later we found out, that company changed their production procedure. The scintillators tested at JINR were produced as a huge blocks and scintillator plates were cut out of this blocks, however, a new plates for S^3 were produced between two glass plates when it is much more difficult to ensure the required thickness.

Due to the different thicknesses and as it is not possible to obtain the information about the thickness from the whole plate and at the same time the deposited energy from cosmic muons is proportional to the thickness of the scintillator, it is very difficult to estimate energy left by muons in the plates. To avoid such a problem it was decided to use monoenergetic electrons with energies, which guarantee absorption of all energy in the scintillation plates, instead.

For testing was used monoenergetic electron source (see Fig. 6.5) which was

developed at Institute of Experimental and Applied Physics (IEAP), CTU, located at Kralupy n. Vltavou in the Envinet company. This tuneable source of electrons with energy in range from 300 to 1800 keV provides flux about 4 electrons per second and its walls are completely light tight (Fig. 6.5(a)). Due to two electromotors (Fig. 6.5(b)) the source is movable in two directions without the need to open the light tight box and enables to change the tested position. For the plate fixing is used the same holder (see Fig. 6.5(c)) as in the case with cosmic muons. Testing with monochromatic electrons has many advantages, for instance: point-like tested location, higher flux than cosmic muons, fixed narrow energy peak, etc.

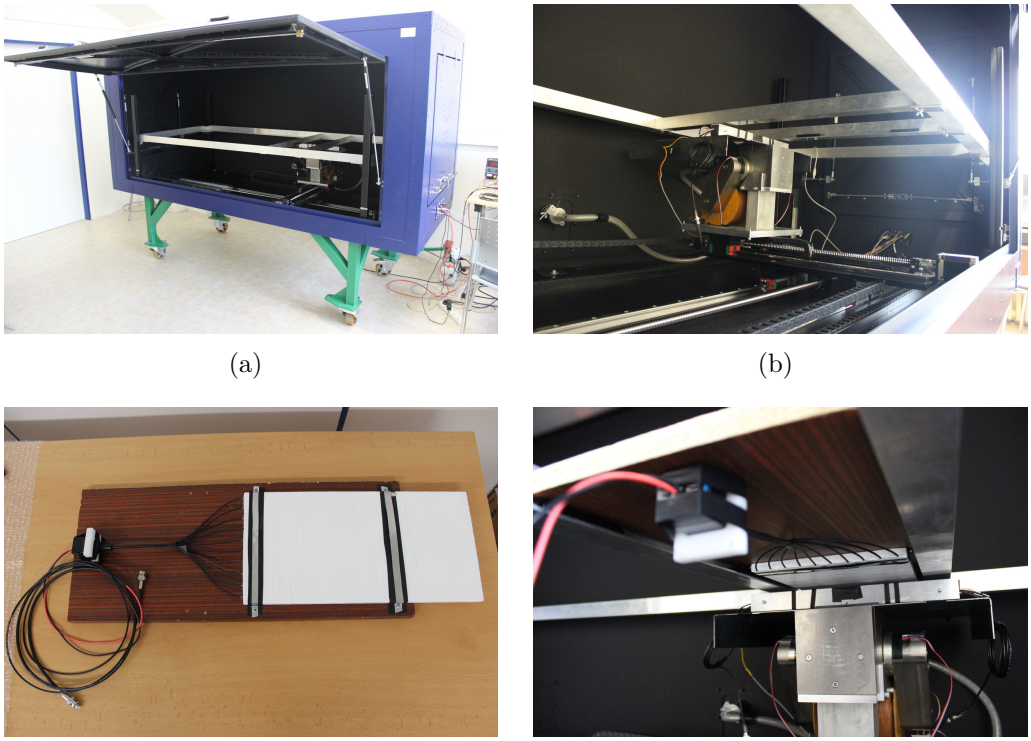

(a) (b)

(c) (d)

Figure 6.5: Testing of the individual scintillation plates with monoenergetic source of electrons a) Light tight box. b) Two electromotors ensuring motion of the electron source. c) The plate holder for testing. d) Experimental arrangement of testing.

To ensure that there will not be the same problem with electrons as with the muons, the simple simulation was done which should reveal the range of the monoenergetic electrons with different initial energies in the scintillator plate. Providing that the range of electrons is smaller than thickness of the plates, the testing method would not be sensitive to the thickness of the plate but only to the quality of the scintillator, the fibres gluing, and wrapping. In the simulations 10 mm thick scintillator with 0.8 mm layer of teflon were studied. The simulation was done for six initial energies of electrons (600, 800, 1000, 1200, 1400, and 1600 keV) and the results for three of them (600, 1000, and 1600 keV) are shown in Fig. 6.6. Two figures for every initial energy are shown. The first one shows

the energy deposition in the four layers of teflon (0.8 mm in total) before the electron enters the volume of the scintillator and the second one illustrates the maximum deepest position in the z axis of the electron with respect to its real energy with which enters the scintillator (initial electron energy minus energy lost in the dead layer). The electrons are incoming from positive part of the z axis and the scintillator is located between -5 mm and 5 mm. The result show that for all studied initial energies the electrons are completely absorbed in the scintillator (even for 8 mm thick scintillator) and thus this method is ideal for plate testing.

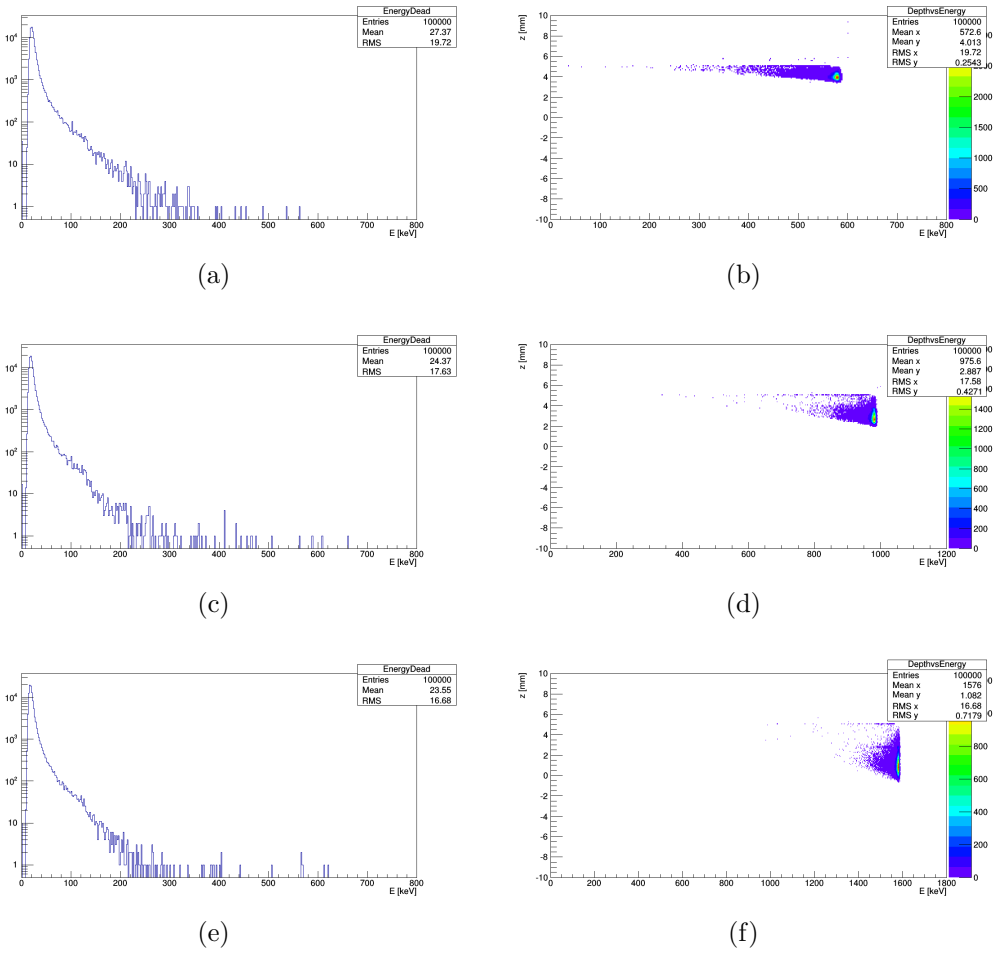

Figure 6.6: The results of the simulation where range of the monoenergetic electrons in the scintillator were studied. In the first row are results for electrons with initial energy 600 keV, in the second row or 1000 keV and in the last one for 1600 keV. The left column shows the energies deposited in the dead layer (teflon) and the right column shows the maximum deepest position in the z direction with respect to the real energy of electron with which enters the scintillator while the scintillator is located between -5 mm and 5 mm.

The first measurements with electrons was carried out to estimate the effect of PMT re-coupling to the fibres. Five measurements with the same plate were performed with 1 MeV electrons aimed to the center of the plate. The PMT was remounted after every single measurement and re-connected again with new layer of optical grease. It is a triggered measurement since electron on its way towards

the plate is passing through very thin (100 μm) scintillator which is used as a trigger. The print screen of the measured signal and measured histograms are shown in Fig. 6.7. For every measurement, an area and amplitude histogram from plate signals were obtained, however only area histogram was further processed by the RooFit library. The area histogram was fitted by the convolution of the Gaussian function (resolution of the detector) and Landau function (energy deposition of the electron in the plate), the results of the fitting is shown in Fig. 6.8. After fitting procedure the required parameters of both functions were obtained. The measured data is listed in Table 6.1. The maximum of the Landau function is important for the comparison of the light yield and the σ of the Gaussian function is important for calculation of the plate resolution η according to the equation

$$\eta = \frac{2.355 \cdot \sigma}{E} \ . \tag{6.1}$$

The standard deviation obtained from five measurements includes effect of the PMT recoupling and also uncertainty of the fitting procedure. Both standard deviations are less than 1 % of measured value and thus re-coupling as well as fitting procedure have negligible effect on measured parameters.

Figure 6.7: Print screen of the digital oscilloscope for one plate testing with electrons. The pink waveform is signal from triggering scintillator, the yellow waveform is the signal from plate under test. The yellow histogram stores areas of signal from plate and the pink histogram holds amplitudes of these signals. Both histograms show the spectrum of 1 MeV electrons.

As the next step, different types of fibre ends treatment like polishing, fixing with epoxy glue and reflective paint application were tested. Also study of different reflective materials for rear wall of the scintillation plate where fibres ends were performed. After all these measurements the optimal preparation procedure was established and all remaining plates were prepared according to it.

During the measurements with 1 MeV electrons the new procedure for calculation of the number of photoelectrons was developed. If the distribution of the detected photoelectrons follows the Poisson distribution (and the simulations says so) we can use equation for the resolution calculation to calculate this number. The resolution equation is the following

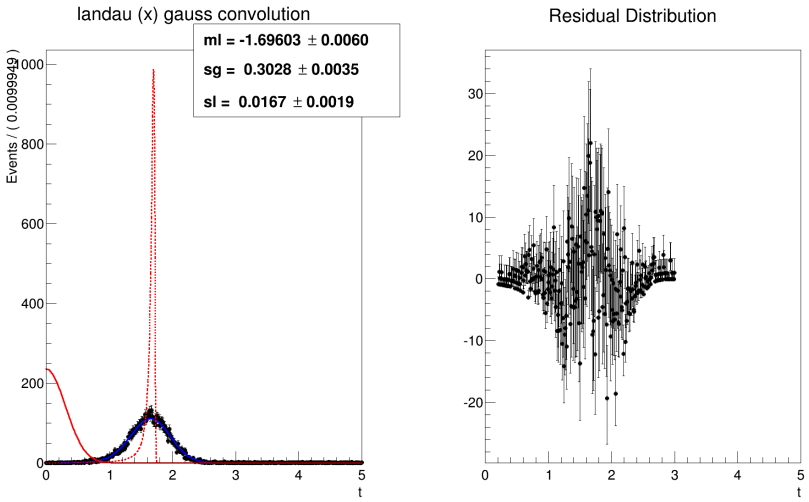

Figure 6.8: Results of the RooFit fitting procedure. On the left the measured signal (black dots), the fit with convolution (in blue) and Gauss (in red, solid) and Landau (in red, dashed) function whose parameters are obtained from the fit are shown. On the right residuals between data points and convolution fit are shown for the monitoring purposes.

Measurement No.	Landau Max [nVs]	σ [nVs]	η [%]
1	1.696	0.303	42.04
2	1.666	0.297	41.97
3	1.663	0.299	42.38
4	1.664	0.302	42.78
5	1.683	0.303	42.43
Average	1.674 ± 0.015		42.32 ± 0.32

Table 6.1: Experimental data from five measurements are presented – position of Landau max, sigma of the Gaussian function and calculated resolution. The standard deviation representing changes caused by recoupling of the PMT and uncertainties caused by convolution fit is calculated.

$$\eta = \frac{\text{FWHM}}{E} = \frac{2.35 \cdot \sigma_E}{E} \ . \tag{6.2}$$

If we assume that the number of detected p.e. is distributed according to the Poisson distribution the σ_E is equal to the $\sqrt{k_{p.e.}}$ where $k_{p.e.}$ is the very number of detected p.e. and measured energy E can be replaced by the $k_{p.e.}$. Therefore the resolution can be calculated just with the knowledge of $k_{p.e.}$ as

$$\eta = \frac{2.35 \cdot \sqrt{k_{p.e.}}}{k_{p.e.}} = \frac{2.35}{\sqrt{k_{p.e.}}} \tag{6.3}$$

and thus number of detected photoelectrons equals

$$k_{p.e.} = \left(\frac{2.35}{\eta}\right)^2 \ . \tag{6.4}$$

If the Equation 6.4 is used with the average resolution value from Table 6.1 the result is $k_{p.e.} = 30.96 \pm 0.47$ which is in the great agreement with the results obtained at JINR with completely different method.

All plates were prepared for testing and every single plate was studied with the same procedure as was described above. Measured spectra were fitted by the convolution function and the Landau maximum and resolution were calculated for every plate. The data is listed in Table 6.2 and is shown in Fig. 6.9.

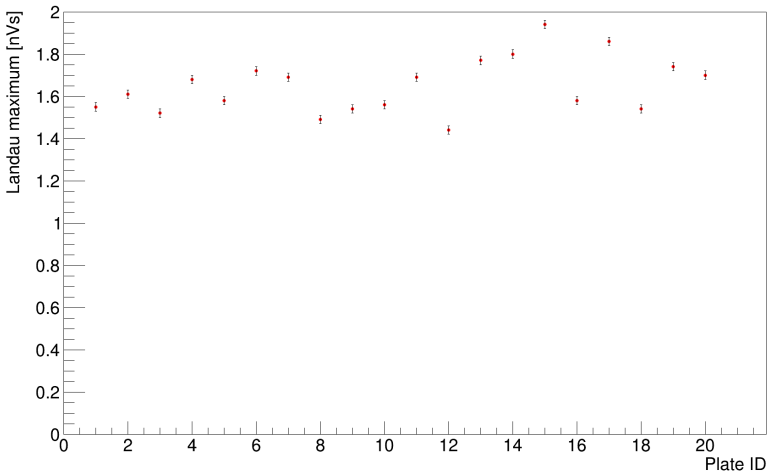

Figure 6.9: Comparison of signal strength from individual plates.

From the obtained results is possible to assume that there are differences between individual plates in the energy resolution as well as in the light yield. The weakest signal reaches 74% of light yield of the strongest one. The average light yield is (1.65 ± 0.13) nVs and thus σ is 7.95 % of the average value. This result is relatively good considering the complexity of one plate (polymerization, fibres gluing, wrapping, fibres polishing, etc.). The average value of energy resolution is $(39.51 \pm 2,81)$ % and thus $\sigma = 7.13$ % of the average value.

6.2 S^3 Construction

When all plates were tested and their parameters were know, the construction of the prototype of the detector S^3 started. First of all, the gadolinium foils were prepared. We decided to create gadolinium foil from the scotch tape (more in Section 5.3) due to its easier manipulation and shorter time demands for production. Figures 6.10 show gadolinium scotch tape and its installation on the plate.

The main purposes of the prototype were to tune full procedure of preparation, to produce detector holder composed from as least material[1] as possible, to evaluate background, and to try construction of the detector itself, fibres handling, and work with two electronic channels. The prototype should have been constructed from 20 plates, however, during the manipulation with the plates,

[1]To limit additional creation of fast neutrons by cosmic muons in close vicinity of our detector, heavy construction materials should be avoided.

Plate ID	Landau Max [nVs]	η [%]
1	1.55 ± 0.02	40.41 ± 0.69
2	1.61 ± 0.02	40.44 ± 0.75
3	1.52 ± 0.02	42.57 ± 0.81
4	1.68 ± 0.02	38.86 ± 0.73
5	1.58 ± 0.02	41.37 ± 0.68
6	1.72 ± 0.02	36.74 ± 0.70
7	1.69 ± 0.02	39.11 ± 0.75
8	1.49 ± 0.02	43.30 ± 0.78
9	1.54 ± 0.02	41.76 ± 0.72
10	1.56 ± 0.02	40.76 ± 0.72
11	1.69 ± 0.02	38.57 ± 0.67
12	1.44 ± 0.02	44.55 ± 0.80
13	1.77 ± 0.02	37.38 ± 0.68
14	1.80 ± 0.02	35.93 ± 0.73
15	1.94 ± 0.02	33.10 ± 0.74
16	1.58 ± 0.02	41.60 ± 0.74
17	1.86 ± 0.02	35.94 ± 0.75
18	1.54 ± 0.02	40.82 ± 0.77
19	1.74 ± 0.02	37.71 ± 0.71
20	1.70 ± 0.02	39.25 ± 0.81

Table 6.2: Resolution and position of the Landau maximum is listed for every scintillation plate.

(a) (b) (c)

Figure 6.10: Photos of the gadolinium foils. a) Box with all gadolinium scotch tapes for S^3 plates. b) Detail of one gadolinium scotch tape. c) Illustration of installation of gadolinium foils on the plate. Four pieces are necessary for one plate.

one fibre was partially broken and the final decision was to use only 18 plates, nine odd and nine even, for the first measurements.

We started with the production of the holder, where all plates are properly fixed and fibres from all even plates are attached to the one PMT and from all odd plates to the second one (see Fig. 6.11(a)). Thereafter, fibres from individual plates were untied and again brought together (Fig. 6.11(b)). Then, the fibres were polished (Fig. 6.11(c)) and PMTs were attached (see Fig. 6.11(d)).

As was mentioned before, the crucial question, in such a low background measurements, is suppression of the background. The main source of background in our case are the fast neutrons [19]. Of course, there is also a necessity to suppress external gammas. In order to suppress all types of the background radiation, the shielding of our detector will be segmented: pure polyethylene (8-16 cm), low background lead (10 cm) and borated polyethylene (8 cm). Both types of polyethylene are already prepared.

Simultaneously, one hundred years old lead was ordered for the detector shielding due to its very low internal activity which is greatly beneficial in the case of low background measurements. The illustration of the shielding structure is attached as Appendix C. The figure shown in the appendix is for illustration only, in reality the structure is the same, but the dimensions are 120 x 120 x 120 cm^3. The whole shielding is composed from 376 bricks with dimension 10 x 10 x 10 cm^3. And the ceiling of the shielding is composed from 12 joist with dimensions 120 x 10 x 10 cm^3. We already obtained all bricks and we are waiting for the ceiling part.

To verify the functioning of the prototype, we performed the first measurement, when the cosmic muons were used. With the 18 plates and roughly 2 MeV of deposited energy per 1 cm of the scintillator, the signal from the detector should reach about 18 MeV. Also the number of events was recorded to calculate approximate flux of detected muons. The expected detected energy is so large that can

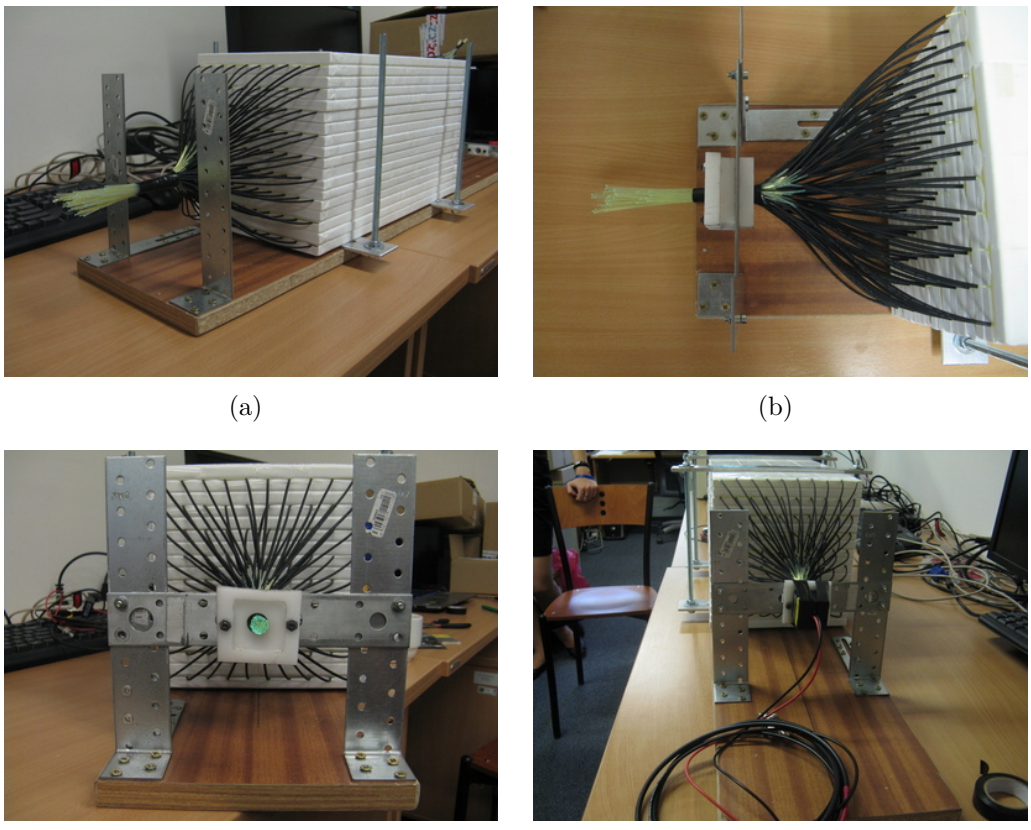

(a) (b)

(c) (d)

Figure 6.11: Photos of the detector construction. a) The fibres from the individual plates were untied and brought together and fixed. b) Top view. c) Polished fibres. d) With attached PMT.

be clearly distinguished from any other type of background.

The PMTs used for the measurement (Hamamatsu R7600U-300) were operated with the bias -800 V which is the recommended value from the data sheet. Another PMT parameters from the final test sheet are shown in Table 6.3. From the ratio of the anode and cathode luminous sensitivity is possible to obtain the gain of a PMT. The gain of the first PMT (EA0125) is $G_1 = 3.269 \cdot 10^6$ and the second PMT (EA0126) is $G_2 = 4.364 \cdot 10^6$. And thus the second PMT amplifies 1.335 times more than the first one. We could change this by the readjustment of the bias applied to one of the PMTs, however we prefer to supply both PMTs from one high voltage to ensure the relative stability between them.

To measure the difference in amplification of both PMTs and moreover to

Serial number	EA0125	EA0126
Cathode Luminous Sens. [μA/lm]	165.8	165.2
Anode Luminous Sens. [A/lm]	542.0	721.0
Anode Dark Current [nA]	0.66	0.20

Table 6.3: Parameters of both used PMTs.

	Arrangement 1	Arrangement 2
No. Events	179 151	187 113
No. Events/1 s	16.59	17.32

Table 6.4: Number of events detected in different arrangements for the whole measurement (3 hours) and per second.

evaluate the asymmetry in the signal strength from odd and even plates we performed measurement with the detector when the PMT EA0125 was attached to the right side and PMT EA0126 to the left side (arrangement 1) and during three hours measurement cosmic muons were detected. Then we switched PMTs (arrangement 2) and again measured three hours. The amplitude of the signal from cosmic muons reached in average about 1 V and the threshold was set at 200 mV to ensure that the majority of the muons exceeds the threshold. Moreover both channels had to be fired simultaneously. The results of both measurements are shown in Fig. 6.12.

The number of detected events for the whole measurement and number of detected events per second for both arrangements are shown in Table 6.4. Differences in the number of detected events for arrangement 1 and 2 can be explained by small asymmetry of the signal strength from even and odd plates and by different gain of the PMTs. The average flux of the cosmic muons is estimated as 1 muon per 1 cm^2 per minute at the sea level. It means that our detector (40 x 20 cm^2) should detect about 13.5 muons per second. The numbers detected by the detector are slightly higher than theoretically calculated numbers which is caused by the slightly larger area than is used in the calculations and by the detection of another types of background.

From the measurement with one plate and 1 MeV electrons we know that the average strength of the signal (per 1 MeV of deposited energy) for the PMT EA0126 is 1.65 nVs. It means that the signal from 18 MeV should be about 30 nVs which can be compared with the yellow histogram in Fig. 6.12. Both figures show that the position of the second peak is about 30 nVs.

In order to determine the asymmetry of the signal strength from even and odd plates the histograms from one PMT and both sides had to be compared. Difference in the signal strength (area spectrum) from both sides provides direct measure of this asymmetry. For comparing two histograms, the mean values were used. The result is shown in Table 6.5. The results show that left part of the detector systematically provides stronger signal than the left part. This asymmetry is dependent on the gain of the PMT, however should not be bigger than 10 %. From this measurements also a ratio of gains from both PMTs was evaluated and is little bit lower than value obtained from the parameters from the final test sheet.

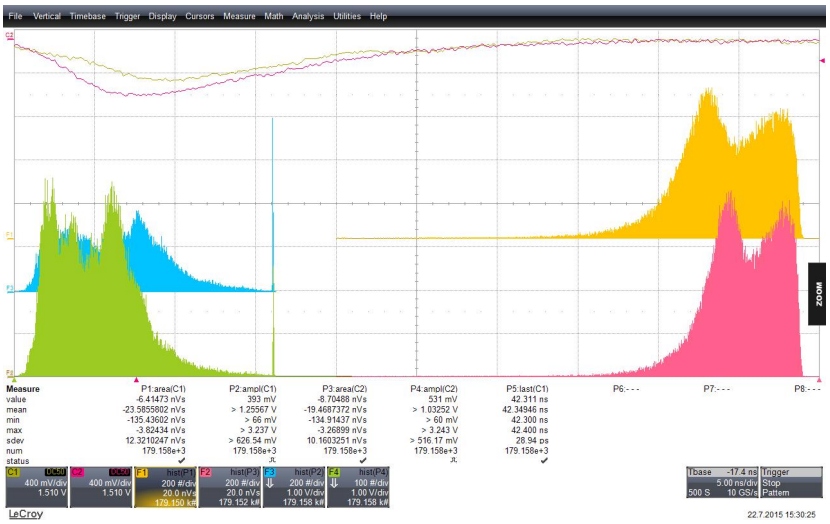

(a)

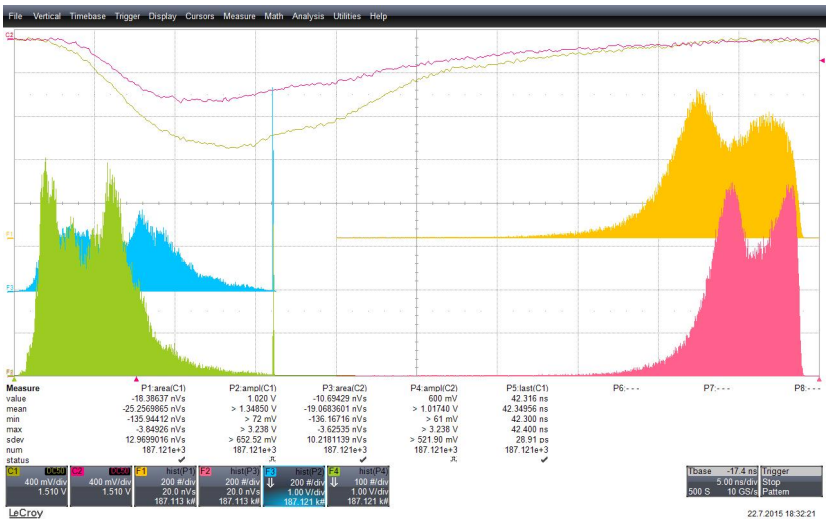

(b)

Figure 6.12: Results of the first two measurements with the detector. The yellow waveform is the signal from the PMT EA0126 and the pink waveform is the signal from the PMT EA0125. The yellow histogram shows the area spectrum of the PMT EA0126 and the blue histogram shows amplitude spectrum of this PMT. The pink histogram shows the area spectrum of the second PMT and the green one the amplitude spectrum of this PMT. The difference in gains is easily visible from all histograms. The origin of the yellow and pink histograms is on the right side and the green and blue histograms on the left side. a) The arrangement 1. b) The arrangement 2.

	Mean_{left} [nVs]	Mean_{right} [nVs]	$\text{Mean}_{right}/\text{Mean}_{left}$
PMT EA0125	19.068	19.469	1.021
PMT EA0126	23.586	25.257	1.071
Gain ratio	1.237	1.285	

Table 6.5: Evaluation of the asymmetry in the signal strength from even and odd plates and ratio of gains from PMT EA0125 and EA0126.

7. Conclusion

The subject of the diploma thesis is connected to very exciting and interesting branch of today's physics, neutrino physics. In the frame of the thesis the first prototype of the antineutrino detector based on scintillating plates was constructed. The current status of R&D as well as the obtained results are further summarized.

For the purposes of better understanding and a potential optimization of the detetor S^3, two Geant4 simulation packages were developed. The first simulation enables to study the light propagation through the scintillation plate and its collection on the photosensitive elements. To ensure the accuracy of this simulation a lot of the wavelength-dependent optical properties had to be set. The results of this simulation, number of detected photoelectrons per 1 MeV and homogeneity of the light collection, very accurately corresponds with the results obtained from the real experiments with electrons and cosmic muons performed at JINR and Kralupy. Using the results of the simulations it is possible to predict behaviour of scintillation plates with different dimensions and shapes. In addition, using these simulations, the electric signal obtained from the PMT could be reconstructed properly.

The second simulation package enables to study IBD pattern in the detectors with different overall dimensions as well as different plate dimensions. For illustration the results from two detectors, S^3 and $1\,m^3$, were provided. A lot of very important properties of the antineutrino detection signal were studied and were used during the design and the development of needed electronics. The most important result of this simulation is the prediction of the supposed antineutrino detection efficiency with respect to the energy threshold. It was found from the results of simulations and from the results of experiment DANSSino that it is possible to detect about $300\,\bar{\nu}$ per day in a distance of 11 m with the detector S^3.

Very important parameter of the scintillation plate is its energy resolution. This parameter is vital for the measurement of the positron energy which determines the ability to monitor isotopic composition and also can extend the studied $(\theta - \Delta m)$ space of a sterile neutrino. The energy resolution is dependent on the amount of the detected light. Due to our benchmark tests performed at JINR we increased the amount of the light twice in comparison with standardly produced Envinet's scintillators and more than three times in comparison with strips used in the experiment DANSS. This was achieved by the optimization of the chemical composition of the scintillator and a better choice of wrapping material. The amount of detected light was obtained by two independent methods and is equal 31 photoelectrons per 1 MeV od deposited energy. At the beginning of this year (2015) the patent application with this improvement was submitted and author of this thesis is one of the authors of this patent application.

In order to reduce the cost of the detector construction, two new methods for the production of the gadolinium layers were invented. The layers prepared by both methods exhibit excellent properties and are incomparably cheaper in comparison with commercially produced gadolinium foils. Moreover, the layers do not influence the quality of the light yield unlike the methods where the gadolinium is added to the volume of the scintillator.

Finally, all the scintillation plates were individually tested with monoenergetic electrons to evaluate the variance in the quality of production. Then the first prototype of the detector S^3 was created from the scintillating plates and the first measurements with cosmic muons were performed. This prototype is equipped with two electronic channels and the signals are processed with the digital oscilloscope.

In September of this year, next 160 scintillation plates will be supplied from the producer and the construction of two S^3 detectors will begin using the results of this diploma thesis. One of the detector will be located under Temelin's reactor and the second one will be sent to Russia and will be installed under a nuclear reactor at Kalinin in cooperation with the JINR team. Estimated time for construction of both detectors is 3-4 months, while time needed for the calibration and testing is about the same. Realistically, both detectors could be installed at the end of next year. Meanwhile, the study of behaviour of our first prototype under various circumstances (influence of the shielding, underground tests, etc.) will continue.

Bibliography

[1] BERNARDINI, E., *Neutrinos in Cosmology*. From http://darkuniverse.uni-hd.de/pub/Main/WinterSchool08Slides/CosmologicalNeutrinos.pdf.

[2] ABAZAJIAN, K. N. et al., *Light Sterile Neutrinos: A White Paper*. ArXiv:1204.5379 [hep-ph] (2012).

[3] LEITNER, R., *Experimental Checks on Standard Model I - lectrures*. Held in 2014 at Faculty of Mathematics and Physics, Charles University in Prague.

[4] Pauli neutrino letter - MicroBooNE Document 953-v1 [online]. Retrieved March 11, 2015, from http://microboone-docdb.fnal.gov/cgi-bin/ShowDocument?docid=953.

[5] HOŘEJŠÍ, J., *Fundamentals of electroweak theory*. Prague : The Karolinum Press, 2002. ISBN 80-246-0639-9.

[6] COWAN, C. L. et al., *Detection of the free neutrino : a Confirmation*. Science 124, 103 (1956).

[7] DANBY, G. et al., *Observation of High-Energy Neutrino Reactions and the Existence of Two Kinds of Neutrinos*. Phys. Rev. Lett. 9 (1962).

[8] DONUT Collaboration, *Observation of tau neutrino interactions*. Phys. Lett. B504 (2001).

[9] AGARWALLA, S. K., *Some aspects of neutrino mixing and oscillations*. Kolkota, 2008. PhD thesis. University of Calcutta.

[10] Lecture writeups, *Neutrino oscillations, March 24, 2015*. From http://www2.warwick.ac.uk/fac/sci/physics/current/teach/module_home-/px435/lec_oscillations.pdf.

[11] OLIVE, K.A. et al. (Particle Data Group), *2014 Particle Physics Booklet*. Chin. Phys. C, 38, 090001 (2014).

[12] LASSERRE, T., *Light Sterile Neutrinos in Particle Physics: Experimental Status*. Phys. Dark Univ. 4, 81 (2014).

[13] KATORI, T., *Short Baseline Neutrino Oscillation Experiments*. J. Phys. Conf. Ser. 598, no. 1, 012006 (2015).

[14] ABE, Y. et al., *Improved measurements of the neutrino mixing angle θ_{13} with the Double Chooz detector*. JHEP 1410, 086 (2014).

[15] SEO, S. H. et al., *New Results from RENO*. PoS Neutel 2013, 018 (2014).

[16] HU, B. Z. et al., *Recent Results from Daya Bay Reactor Neutrino Experiment*. ArXiv:1505.03641 [hep-ex].

[17] KIM, S. B., *Status and Prospects of Reactor Neutrino Experiments*. ArXiv:1504.08268 [hep-ph].

[18] EGOROV, V., *Status of the DANSS project*. Talk at NDM15, Jyvaskyla, Finland, June 1-5, 2015.

[19] ALEKSEEV, I. et al., *DANSSino: a pilot version of the DANSS neutrino detector*. Phys. Part. Nucl. Lett. 11 (2014) 473.

[20] BELOV, V. et al., *Registration of reactor neutrinos with the highly segmented plastic scintillator detector DANSSino*. JINST 8, P05018 (2013).

[21] Envinet a.s. - Nuvia Group [online]. Accessible from http://www.envinet.cz/.

[22] EGOROV, V. et al., *Antineutrino detector development for safeguards in Russia: DANSS*. Talk at AAP2011, Vienna, Austria, Sept. 15-16, 2011.

[23] VOGEL, P. et al., *The angular distribution of the reaction* $\bar{\nu}_e + p \rightarrow e^+ + n$. Phys.Rev. D60 (1999).

[24] NAKAJIMA, K. et al., *A simple model of reactor cores for reactor neutrino flux calculations for the KamLAND experiment*. Nucl. Instrum. Meth. A 569 (2006).

[25] BATTAGLIERI, M., *An antineutrino detector to monitor nuclear reactor's power and fuel composition*. Talk at Frontier Detectors for Frontier Physics – 11^{th}Pisa meeting on advanced detectors, La Biodola, Italy, May 24-30, 2009.

[26] MUELLER, Th. A. et al., *Improved predictions of reactor antineutrino spectra*. Phys. Rev. C 83 (2011).

[27] HUBER, P., *On the determination of anti-neutrino spectra from nuclear reactors*. Phys. Rev. C 84 (2011).

[28] MENTION, G. et al., *Reactor antineutrino anomaly*. Phys. Rev. D 83 (2011).

[29] VIVIER, M., *Nucifer: toward anti-neutrino detection 7 m away from a reactor core*. Talk at Applied Antineutrino Physics Conference, Hawai'i, 2012.

[30] CONRAD, J. M. et al., *Sterile neutrino fits to short baseline neutrino oscillation measurements*. Adv. High Energy Phys. 2013 (2013).

[31] DANILOV, M. on behalf the DANSS collaboration, *Sensitivity of DANSS detector to short range neutrino oscillations*. PoS EPS-HEP2013 493 (2013).

[32] BATTAGLIERI, M. et al., *An anti-neutrino detector to monitor nuclear reactor's power and fuel composition*. Nucl. Instrum. Meth. A 617 (2010).

[33] SUEKANE, F., *Application of reactor antineutrinos: Neutrinos for peace*. Nucl. Phys. B 235-236 (2013).

[34] NIETO, M. M. et al., *Detection of antineutrinos for non-proliferation*. Nucl. Sci. Engin. 149 (2005).

[35] BERNSTEIN, A. et al., *Nuclear reactor safeguards and monitoring with antineutrino detectors*. J. Appl. Phys. 91 (2002).

[36] HUBER, P. et al., *Precision spectroscopy with reactor anti-neutrinos*. Phys. Rev. D 70, 053011 (2004).

[37] ANJOS, J. C., *Current Status of the Construction of the Angra Antineutrino Detector*. Talk at Vienna University of Technology, Austria, Sept. 15-16, 2011.

[38] Geant Collaboration. Geant4 Web page [online] http://geant4.web.cern.ch/.

[39] AGOSTINELLI, S. et al., *Geant4 - a simulation toolkit*. Nucl. Instrum. Meth. A 506 (2003).

[40] ALLISON, J. et al., *Geant4 Developments and Applications*. IEEE Transactions on Nuclear Science 53 No. 1 (2006).

[41] Geant4 collaboration, *Introduction to Geant4*. Accessible from http://geant4.web.cern.ch/geant4/support/userdocuments.shtml.

[42] Kuraray CO [online]. Accessible from http://kuraraypsf.jp/psf/

[43] ARGYRIADES, J. et al., *Spectral Modeling of scintillator for the NEMO-3 and SuperNEMO detectors*. Nucl. Instrum. Meth. A 625 (2011).

[44] PAHLKA, B., *Photon Transport Simulations and some measurements*. Presentation accessible from https://indico.fnal.gov/getFile.py/access?contribId=8&resId=0&materialId=slides&confId=4351.

[45] Kuraray CO [online]. Accessible from http://kuraraypsf.jp/psf/ws.html.

[46] Hamamatsu Photonics K. K., *2014 Photonic devices - Electron tube devices and applied products*. Accessible from http://www.hamamatsu.com/resources/pdf/etd/pdev_2014_TOTH0022E.pdf.

[47] GUO, X., *A Precision Measurement of the Neutrino Mixing Angle Θ_{13} Using Reactor Antineutrinos At Daya Bay*. ArXiv:hep-ex/0701029 (2007).

[48] ADADUROV, A. F. et al., *Optimizing concentration of shifter additive for plastic scintillators of different size*. Nucl. Instrum. Meth. A 599 (2009).

[49] FAJT, L. et al., *Present status of sensitive detector of reactor's antineutrinos using scintillating detectors*. Poster at Low Radioactivity Techniques conference, Seattle, USA, March 18-20, 2015.

[50] BELLAMY, E. H. et al., *Absolute calibration and monitoring of a spectrometric channel using a photomultiplier*. Nucl. Instrum. Meth. A 339 (1994).

[51] ABDUSHUKUROV, D. A. et al., *Modeling the registration efficiency of thermal neutrons by gadolinium foils*. JINST 2 (2007).

List of Tables

List of Figures

A. Startup macro for the S^3 simulations

```
1
2 #
3 /run/verbose 0
4 /event/verbose 0
5 /tracking/verbose 0
6 #
7
8 #
9 #/gun/particle e+
10 #/gun/energy 300 MeV
11 /antiNeu/gun/position 3
12 /antiNeu/gun/direction 2
13 /antiNeu/gun/energy 2
14 /antiNeu/gun/particle 3
15 #
16 #/gun/position -5.0 -15.0 0.0 cm
17 #
18 /antiNeu/geometry/polyX 40.0 cm
19 /antiNeu/geometry/polyY 20.0 cm
20 /antiNeu/geometry/polyZ 1.0 cm
21 /antiNeu/geometry/tiO2thick 0.1 mm
22 /antiNeu/geometry/nLayers 40
23 /antiNeu/geometry/nLayInOneStack 2
24 /antiNeu/geometry/nScintInOneLayer 2
25 /antiNeu/geometry/update
26 #
27
28 #
29 #/control/execute visO.mac
30 #
31 /run/beamOn 10000
```

B. Results of the simulations for 1 m^3 detector

The same figures as in Sec. 4.3.1 are shown, however, this time the simulation was done with the 1 m^3 detector. Dimensions of the plates were changed to 100 x 20 x 1 cm^3 and five plates were used in one layer. Again, 10 000 IBD interactions were simulated and the results from simulation package and from Analyser program are shown in the following figures. Descriptions of individual figures can be found also in Sec. 4.3.1. Only the most important differences compared to the results from the S^3 detector are discussed.

The most striking changes from results shown in Fig. B.1 occurred in Figs. d), f), and h). It shows that the neutron is affected by changing the size of the detector much more than positron. Number of interactions shown in Fig. d) increased from 14.04 to 19.01 interactions. Also multiplicity of hits shown in Fig. f) and track length and distance from vertex were increased. Multiplicity changes from 5.2 to 6.8 hited plates it means that in the larger detector neutron will hits more plates. Distance from vertex changed from 80.81 to 104.3 mm.

The efficiency for neutron capture rose about almost 30 %, from 46.0 to 74.9 %. It shows that with larger detector the antineutrino detection efficiency can be improved significantly. The efficiency capture on Gd rose from 41.1 to 67.1 %, however, the probability that if the neutron is captured it is on the hydrogen atom remained the same (10.3 %). Number of gammas created after the neutron capture increased from 1.66 to 2.69 which is mainly caused by the decrease of neutrons escaping without being captured. The same caused enhancement of the peaks about 8 MeV in the Fig. B.5.

The shape of the spectrum of energy deposited in the detector by the gammas produced after neutron capture was changed very significantly. The larger detector provides more space for gammas to interact in the volume of the detector and left their energy inside. This leads to a stronger delayed signal which will be easier distinguished from the background.

On the other side positron results almost do not changed. Already high efficiency for positron annihilation was increased by 2 % and the number of positrons which annihilate in flight remained the same. Also both time distribution between positron annihilation and neutron capture and energies deposited by gammas from positron annihilation nearly do not changed. And the distance to the first interaction of gammas produced after the annihilation of the positron increased too from the same reasons as the energy deposited in the detector by the gammas produced after neutron capture.

Table B.1 shows how the efficiency of antineutrino detection changed. Detection efficiency increased by more than 30 % for all values of threshold energy. This is very good message for the future of the experiment S^3. Nevertheless, the detailed simulations of the light propagation in the plate with dimensions 100 x 20 x 1 cm^3 has to be done.

	Detection efficiency [%]	
E_{thr} [MeV]	OR condition	AND condition
0.035	70.83	66.17
0.1	70.69	63.36
0.25	70.16	58.38
0.5	68.01	50.67
0.75	63.69	42.85
1	58.13	34.65
1.5	43.56	19.29

Table B.1: The antineutrino detection efficiency of the detector S^3 with respect to the E_{thr} and with respect to the condition on the delayed signal. If deposited energy has to outreach E_{thr} in both channels (AND) or at least in one channel (OR). These results are for $1\,\mathrm{m}^3$ detector.

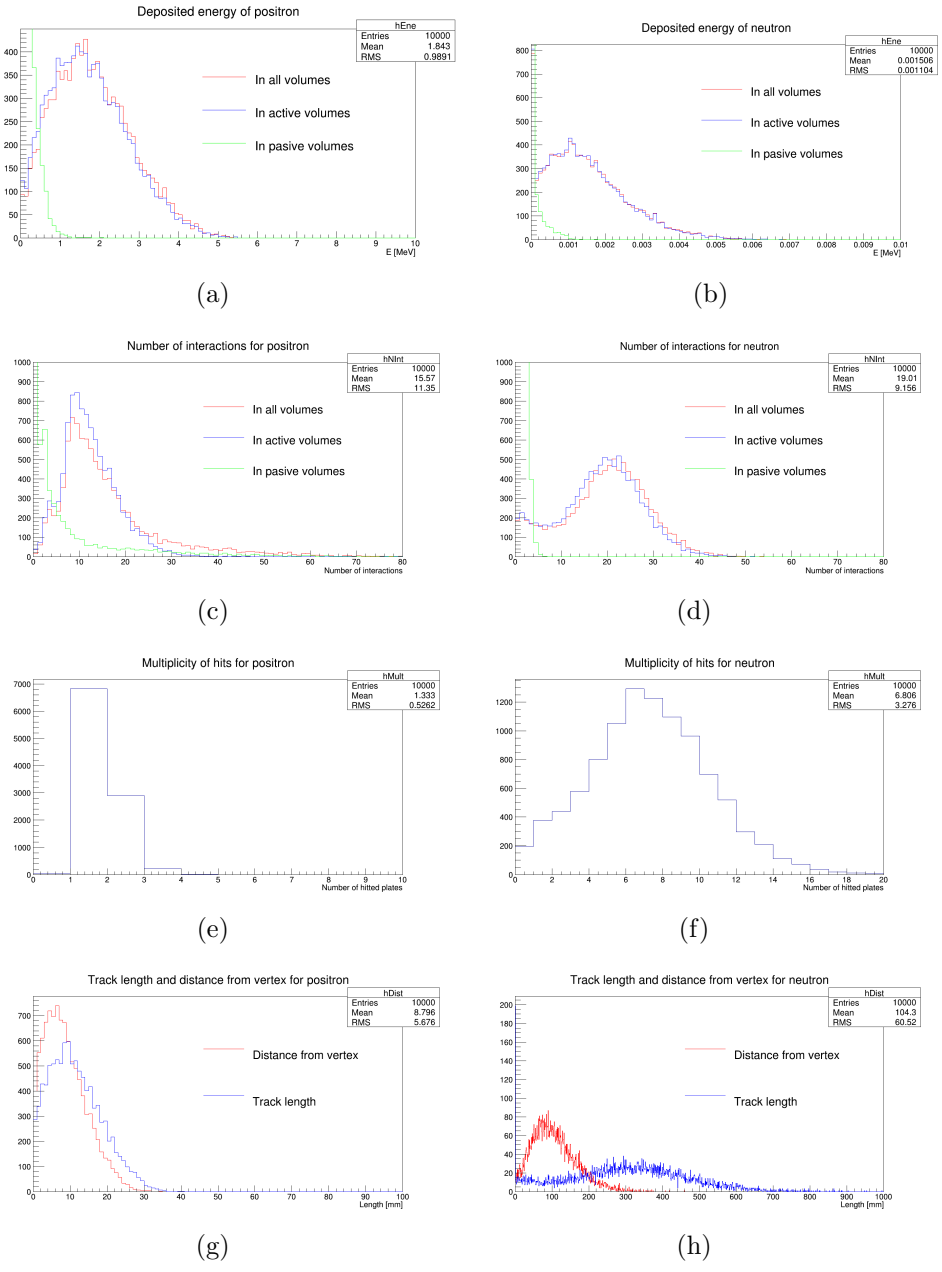

Figure B.1: Illustration of basic quantities which can be obtained from simulations directly. The description of individual histograms is closely explained in the text. These results are for $1\,\mathrm{m}^3$ detector.

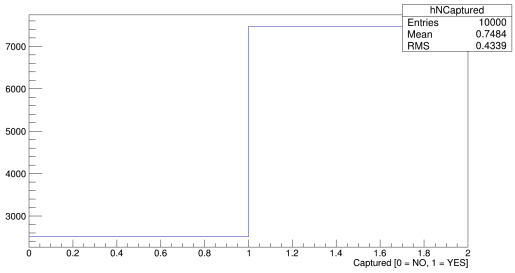

Figure B.2: Number of neutrons captured on some atom (gadolinium, hydrogen). Bin 0 represents neutrons escaping from the volume of the detector without being captured, on the contrary, bin 1 represents captured neutrons. As you can see, 74.8 % of neutrons is captured in our configuration. These results are for $1\,\mathrm{m}^3$ detector.

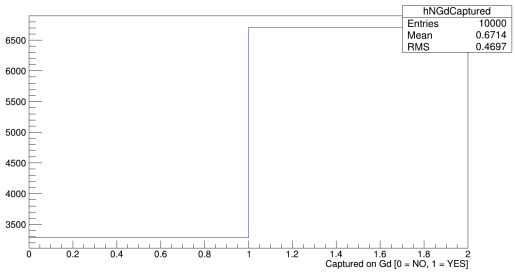

Figure B.3: Number of neutrons captured and only on gadolinium atom. Bin 0 represents neutrons escaping detector or detected on the hydrogen atom. Bin 1 represents neutrons captured on gadolinium. These results are for $1\,\mathrm{m}^3$ detector.

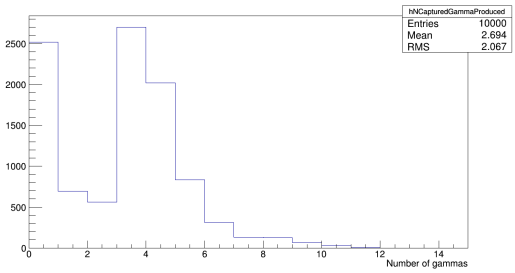

Figure B.4: Number of gammas created after the neutron capture on both types, hydrogen and gadolinium, atoms. If the neutron was not captured, the 0 bin is incremented. These results are for $1\,\mathrm{m}^3$ detector.

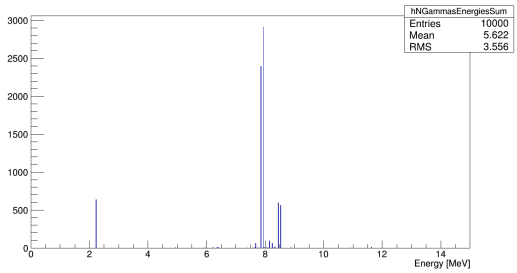

Figure B.5: Total energy spectrum of gammas produced after neutron capture. Number of captures on hydrogen or gadolinium atoms can be easily determined from the energy released in de-excitation of newly created atom. These results are for $1\,\mathrm{m}^3$ detector.

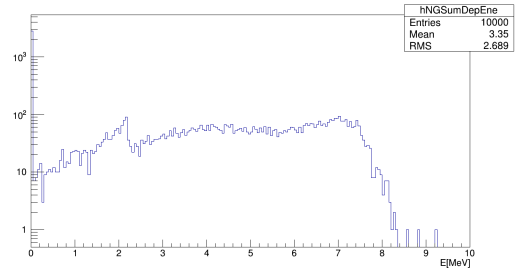

Figure B.6: The amount of energy deposited in the detector by the gammas produced after neutron capture (Y log scale). These results are for $1\,\mathrm{m}^3$ detector.

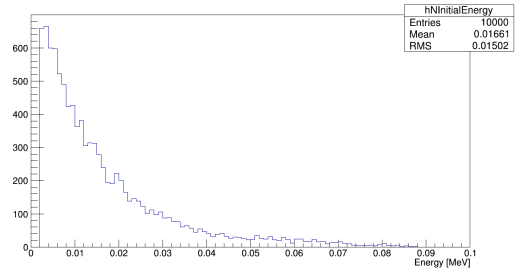

Figure B.7: Initial energy spectrum of simulated neutrons. This quantity is consistent with input data shown in Fig. 4.15(a). These results are for $1\,\mathrm{m}^3$ detector.

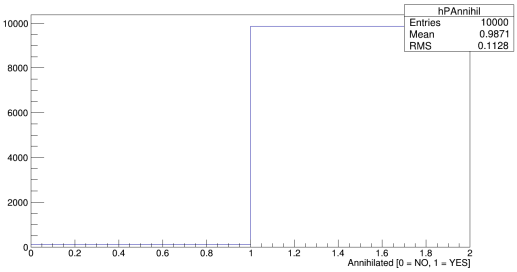

Figure B.8: Number of annihilated positrons. Bin 0 represents positrons escaping from the volume of the detector without annihilation, on the contrary, bin 1 represents annihilated positrons. The simulation shows that 98.71 % of positrons annihilate in our configuration. These results are for $1\,\mathrm{m}^3$ detector.

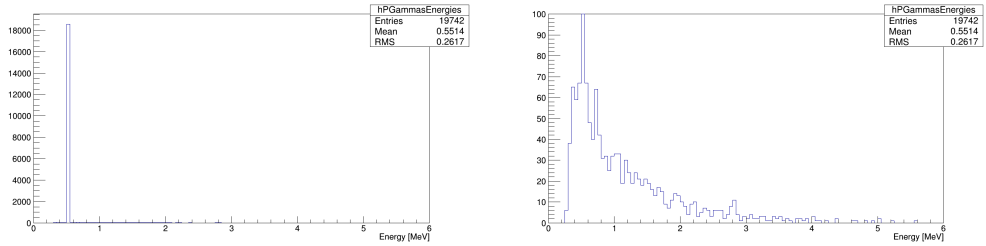

(a) (b)

Figure B.9: a) Energy spectrum of gammas produced after positron ann*ihilation. b) The same spectrum as in Figure a) with zoom applied on the Y axis. The figure shows that about 5 % of all annihilations takes place in flight when gammas with energies different from common 511 keV are created. These results are for 1 m^3 detector.

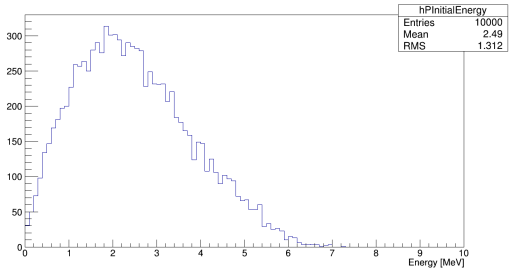

Figure B.10: Initial energy spectrum of simulated positrons for 100 % ^{235}U fuel. This quantity is strongly dependent on the composition of simulated fuel. These results are for 1 m^3 detector.

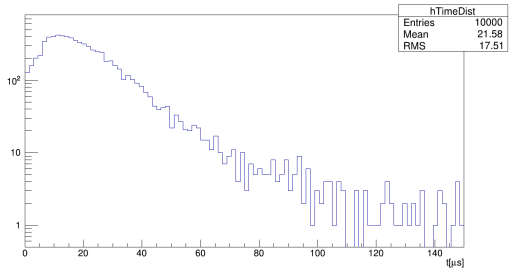

Figure B.11: Time distribution between positron annihilation and neutron capture (Y log scale). This quantity is very important to set optimal size of the time window between prompt and delayed signal. These results are for 1 m^3 detector.

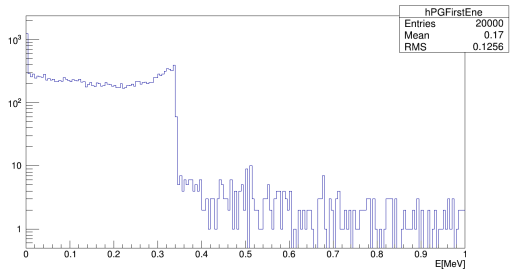

Figure B.12: Energies deposited by gammas from positron annihilation in their first interaction (Y log scale). These results are for $1\,\mathrm{m}^3$ detector.

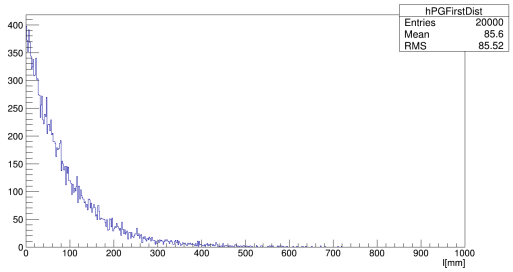

Figure B.13: Distance to the first interaction of gammas produced after the annihilation of the positron. These results are for $1\,\mathrm{m}^3$ detector.

C. Draft of the lead shielding

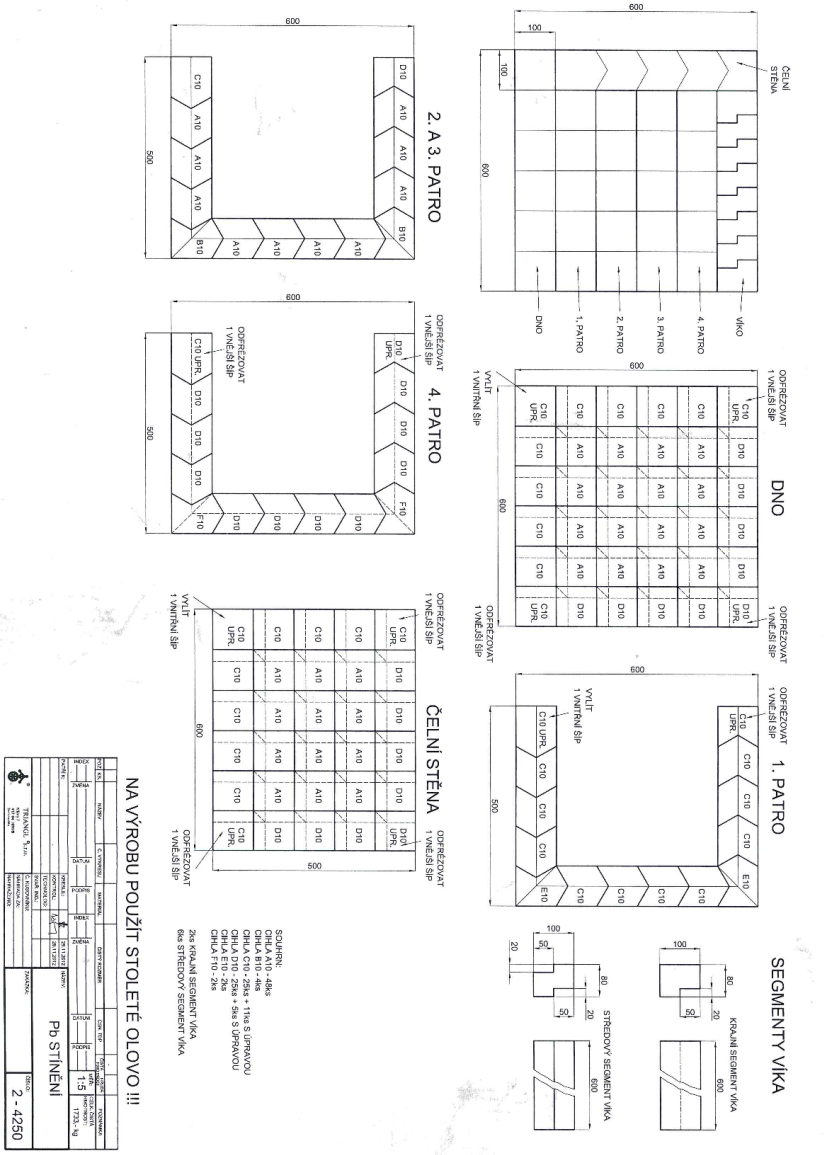

Figure C.1: Draft of the lead shielding for the detector S^3.